Title

Reconstruction and Analysis of Interior Flows with Applications in Cardiovascular Hemodynamics

Author

Frank, Sarah

Publication Date

2019

Peer reviewed|Thesis/dissertation

RECONSTRUCTION AND ANALYSIS OF INTERIOR FLOWS WITH APPLICATIONS IN CARDIOVASCULAR HEMODYNAMICS

By

Sarah Loring Frank

A dissertation submitted in partial satisfaction of the

requirements for the degree of

Doctor of Philosophy

in

Engineering - Mechanical Engineering

in the

Graduate Division

of the

University of California, Berkeley

Committee in charge:

Professor Shawn Shadden

Professor Andrew Szeri

Professor Ming Gu

Fall 2019

Reconstruction and Analysis of Interior Flows with Applications in Cardiovascular Hemodynamics

Sarah Loring Frank

Abstract

Reconstruction and Analysis of Interior Flows with Applications in Cardiovascular Hemodynamics

By Sarah Loring Frank

Doctor of Philosophy in Engineering – Mechanical Engineering
University of California, Berkeley
Professor Shawn Shadden, Chair

Heart disease is the leading cause of death worldwide, killing 17.9 million annually. Blood flow patterns in the heart have been shown to be associated with disease, but the adoption of blood flow diagnostics in the clinic has been limited by the difficulty of imaging blood flow inside the body. Color-Doppler ultrasound and 4D-flow Magnetic Resonance Imaging (MRI) are currently the two main tools used to image blood flow. Color-Doppler ultrasound is widely-accessible and relatively inexpensive, but traditional ultrasound only collects a single component of velocity on a single plane. 4D-flow MRI collects all three components of velocity in a 3D domain but is much more expensive and difficult to use. Here, we use computational tools to improve image processing and analysis of blood flow in the left ventricle for both color-Doppler ultrasound and 4D-flow MRI data. Specifically, we seek to develop methods for de-noising and reconstructing interior flow fields and for calculating kinetic energy and viscous dissipation as potential diagnostic tools from limited data.

First, we investigate tools to augment color-Doppler ultrasound data. We test multiple methods to calculate a second, in-plane component of velocity from the available velocity and geometry information. Previously, methods to reconstruct the second component of velocity were developed using an assumption that through-plane divergence was negligible. We introduce alternative methods to reconstruct the second component of velocity without making the through-plane assumption. However, when compared to previous methods, these alternative methods did not show an improvement in the accuracy of predicting the second component of velocity.

Following these results, we propose modifications to estimates of diagnostic measures from color-Doppler ultrasound data. For many diagnostic measures calculated from color-Doppler ultrasound data, the velocity is measured, a second component of velocity is calculated, and a 2D evaluation of the diagnostic measure is performed. Instead, we propose a 1D evaluation of diagnostic measures directly from the single, measured component of velocity. We introduce this metric for kinetic energy and viscous dissipation rate in the left ventricle, two measures that have been shown to be correlated with heart disease. Using computational fluid dynamics simulation results to obtain a true measurement from all three components of velocity in the entire ventricle, virtual ultrasound measurements were taken and the different types of estimates were calculated from the virtual ultrasound. These reduced dimensional estimates were then compared to the true, 3D values. Both the 1D and 2D estimates were correlated with the 3D values and kinetic energy was more robust to noise and lower grid resolution. These results indicate that 1D estimates, and kinetic energy especially, should be continued to be explored for further use in the clinic.

Next, we explore a modal analysis method to de-noise and reconstruct 3D flow fields that can be applied to 4D-flow MRI or color-Doppler ultrasound data. While many methods have been introduced to de-noise 3D velocity fields, this modal analysis method provides advantages because it results in a divergence-free flow field, satisfies necessary boundary conditions, and can be applied to multiple types of data. To test the method, it was applied to flow inside a cube, through a stenosis, around a cylinder, and inside the left ventricle using data from computational fluid dynamics simulations. The modal analysis method was shown to reduce noise from noisy velocity fields and to be able to adequately reconstruct velocity fields with missing data points or missing components of velocity. These results are promising for use with 4D-flow MRI data where a 3D flow field on a 3D domain is available. These results are also promising for use with more recent advancements of color-Doppler ultrasound that allow for measurements on multiple parallel planes and for developing capabilities of color-Doppler ultrasound that allow for measurement of a second, in-plane component of velocity.

Through reduced dimensional estimates of kinetic energy and viscous dissipation rate in the left ventricle that can be measured using color-Doppler ultrasound data and the introduction of a modal analysis technique to de-noise and reconstruct 3D flow fields, this dissertation advances image processing and analysis tools for blood flow in the left ventricle.

Acknowledgments

I would like to thank a few people who, without their help, this work would not be possible. My advisor, Professor Shawn Shadden, provided me the opportunity to explore this research and helped through all parts of this work from providing advice to getting me connected with the right people. Professor Andrew Szeri was a constant source of support throughout, providing encouragement and asking questions from a fresh perspective. Siavash Ameli was also instrumental in the development of the modal analysis work. He was always willing to help explain new concepts and discuss ways for us to test and improve the method. I would also like to thank Tino Ebbers and Jonas Lantz from Linköping University for providing data for use in multiple parts of the project. In addition, I would like to thank the rest of the Shadden lab for their support and feedback on everything from general ideas to conference presentations. Lastly, I would like to thank my friends and my family for their constant support throughout this whole process.

Contents

List of Figures

List of Tables

Chapter 1

Introduction

1.1 Motivation

Heart disease is the leading cause of death worldwide and in the United States. In the United States, it contributes to 1 in 4 deaths and costs an estimated $200 billion each year [3]. Heart disease includes many conditions that affect heart health, from the muscles of the heart, to valves, rhythm, and narrowed or blocked blood vessels. Although commonly thought of as a problem affecting older people in the developed world, heart disease is a prominent problem for all types of people all across the world. Over three quarters of deaths due to heart disease occur in low- and middle-income countries [4], and in the United States, in addition to being the first leading cause of death for people aged 75 and over, heart disease is the fifth leading cause of death for young Americans aged 1-9 and 15-34 [5].

In order for cardiovascular diseases to be effectively treated, they need to be diagnosed early. Unfortunately, there are many aspects of heart disease that are not well understood, frequently making both diagnosis and treatment difficult. Clinical measures have been developed to assess cardiac function and public health initiatives have been aimed at lowering cholesterol and blood pressure. However, many current indicators of disease show up inconsistently in patients. For example, heart failure symptoms vary widely and certain treatment options have only improved the prognosis for patients with certain sets of symptoms [6]. In another study, flow patterns were shown to change quickly when pacemaker settings were altered even though heart structure remained the same [7]. A more complete understanding of both healthy and diseased heart function is necessary for improved diagnosis and treatment of heart disease. In particular, several studies have linked blood flow inside the heart to disease etiology. However, imaging intra-cardiac blood flow remains challenging, limiting our understanding of heart failure and its hemodynamic consequences and our ability to translate new knowledge easily into the clinic.

To this end, this dissertation focuses on methods to improve image processing of flow data inside the heart. With improved imaging, researchers will be able to better study and understand how flow is related to heart disease, and ultimately doctors will be able to use these improved imaging methods to evaluate the quality of flow fields in the clinic.

1.2 Background - The Heart

1.2.1 The Heart

The heart consists of four chambers (Figure 1.1) and pumps blood throughout the body. Deoxygenated blood is returned from the body through the venae cavae to the right atrium. Then, the blood goes through the tricuspid valve to the right ventricle. From the right ventricle, it exits the heart through the pulmonary valve into the pulmonary arteries to the lungs. The now oxygenated blood returns from the lungs through the pulmonary veins to the left atrium. Then, it goes through the mitral valve to the left ventricle. From the left ventricle, it exits the heart through the aortic valve into the aorta, and carries oxygenated blood to the rest of the body.

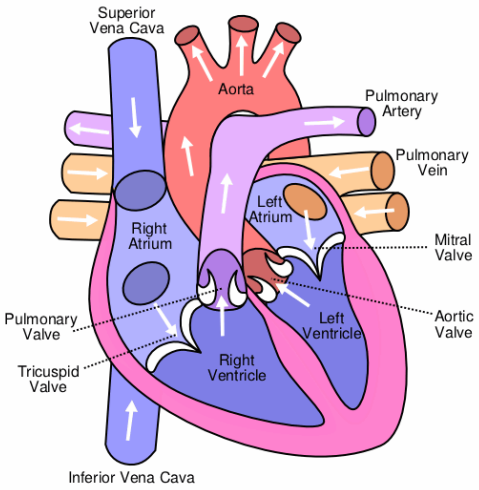

Figure 1.1: The four chambers of the heart. Illustration by Eric Pierce [1]. Reprinted courtesy of the Copyright Holder under a Creative Commons License CC BY-SA 2.0

1.3 Importance of Velocity Fields in the Heart

Heart disease is a broad category of diseases related to the function of the heart. Hemodynamics, the study of blood flow, is an important field that has improved our understanding of many of these heart diseases. Here we will give an overview of a few heart diseases including heart failure, aortic regurgitation, heart attack, and some congenital heart diseases, and discuss why blood flow is important for these diseases.

Heart failure is a condition where the heart is not pumping blood as efficiently as it should be. This means that not enough nutrients are being pumped throughout the body and the symptoms are fatigue and shortness of breath. Although there is not a cure, at some stages heart failure can be managed with medication, but at other stages more serious

medical attention is required. In addition, heart failure can affect the left and/or the right side of the heart, but more frequently affects the left side [8].

Aortic regurgitation is a disease where instead of blood flowing directly out of the left ventricle into the aorta through the aortic valve, some blood flows from the aorta back into the left ventricle. As a result, the left ventricle is required to work harder, and depending on the severity, aortic regurgitation can lead to heart failure. Often, the symptoms for aortic regurgitation do not appear until after the patient has already experienced heart failure. However, if changes in the flow patterns representative of aortic regurgitation are discovered earlier, then proper treatment can help prevent heart failure.

A heart attack, or myocardial infarction, occurs when blood flow is blocked in a vessel that brings blood to the heart muscles. The restriction of blood flow to the muscles is referred to as ischemia, and damage to the muscle due to the lack of blood flow is referred to as myocardial infarction. Damage to the muscle affects how blood moves inside the heart and impairs the heart's ability to pump blood throughout the body [9].

Many congenital heart diseases involve an atypical geometry of the heart. The altered geometries mean that blood moves throughout these hearts differently than inside a healthy heart, and often require surgical intervention. Often, the flow is not as efficient and can make everyday activities more difficult, similar to symptoms of heart failure. Understanding flow in these cases is important because it can inform any invasive procedures to help redirect flow in a more efficient manner. For example, an atrioventricular septal defect is when there are holes between the left and right sides of the heart. This means that some blood that has already been oxygenated in the lungs will return to the lungs before going to the rest of the body, and some blood that never makes it to the lungs will flow to the rest of the body, lowering the oxygen concentration of blood flowing throughout the body. Fontan circulation is another case that refers to a type of flow circulation where patients born with only a single ventricle require surgery to redirect the flow from the veins directly to the lungs, bypassing the heart. Tetralogy of Fallot is a congenital heart disease that is a combination of four other geometric changes: an atrioventricular septal defect, the aortic valve is enlarged and is located in one of the holes between the two chambers, a thickening of the right ventricular wall, and a narrowing of the pulmonary valve.

Heart failure, aortic regurgitation, heart attack, and congenital heart diseases all involve different changes in the geometry of the heart along with changes in blood flow patterns inside the heart. Knowledge of both the geometry and the flow are important for understanding how the disease progresses, and thus how it can potentially be treated.

1.3.1 The Left Ventricle

In many heart diseases, the left ventricle is the site of pathological changes that lead to disease. The blood must travel from the left ventricle to the rest of the body, which requires very large pressure gradients. Therefore, the left ventricle is where the blood experiences the highest pressures. The effects of this are seen across heart diseases, in both the geometry of the left ventricle and the flow fields inside the left ventricle. For example, in the majority

of cases of 'systolic' heart failure, or failure caused by changes during the ejection phase of the cycle, impaired left ventricular contractility is one of or the only contributing factor to failure [10]. In 'diastolic failure', or failure caused by changes during the filling phase of the cycle, there is an increase in left ventricular diastolic pressure that leads to disease [10].

While flow structures that appear inside the left ventricle are correlated with indicators of heart disease, current diagnostic measures often focus on bulk transport variables and not on intracardiac flow structures [11]. However, certain flow patterns apply characteristically different loads on the heart that lead to heart disease or other complications such as thrombus formation. In particular, vortices in the left ventricle have been shown to influence energy losses and have been correlated with patient disease conditions [12, 13, 14]. Other measures of transport such as residence time of blood in the ventricles or atria have also been identified as causes for thrombosis and cardioembolism [15].

The challenge of imaging blood flow has impacted the extent to which blood flow patterns in the heart are used in the clinic. As mentioned previously, current symptoms of heart disease often show up inconsistently between patients, and an improved understanding of blood flow in the heart could help resolve many of these inconsistencies.

1.4 Measuring Velocity in the Left Ventricle

1.4.1 Imaging

Lack of information about flow in the heart is largely due to the difficulty of measuring blood flow in vivo. Similar to many biological tissues of interest in medicine, blood is an opaque fluid found within opaque cavities, making it inherently difficult to image. However, blood is additionally difficult to image because it is moving, and it is contained in cavities that are also moving. At each point in space at each point in time, we are interested in the magnitude and direction of blood. Currently, Magnetic Resonance Imaging (MRI), and Doppler ultrasound are the main imaging methods used to examine blood flow throughout the body.

MRI with phase-contrast velocity mapping, known as 4D-flow MRI is the current gold-standard for examining cardiac flow data because it is the only non-invasive method that provides velocity information that has three components and is available on a three-dimensional grid at multiple time points. Data is gathered throughout the cardiac cycle, providing the fourth dimension of time.

MRI works by taking advantage of the fact that the spin of a proton is affected predictably by an applied magnetic field. Atoms with an odd number of protons or neutrons have a randomly aligned angular spin momentum that will align with the axis of a strong, external magnetic field, causing a net 'longitudinal' magnetization. These spins precess about the axis of the external field at a frequency proportional to the strength of that field. Then, to measure a signal, energy is added to the system to 'excite' the spins, changing the axis that they precess about. Receiver coils are used to measure this signal. Different tissues

respond to the added energy in different ways, and imaging parameters can be adjusted to highlight desired tissues. Certain sequences can also be used to measure the magnitude of velocity in a specific direction because the velocity of an atom influences the phase of the spin. Velocity is calculated by measuring the phase shift of the spins, and converting those values to velocities [16]. An example is shown in Figure 1.2.

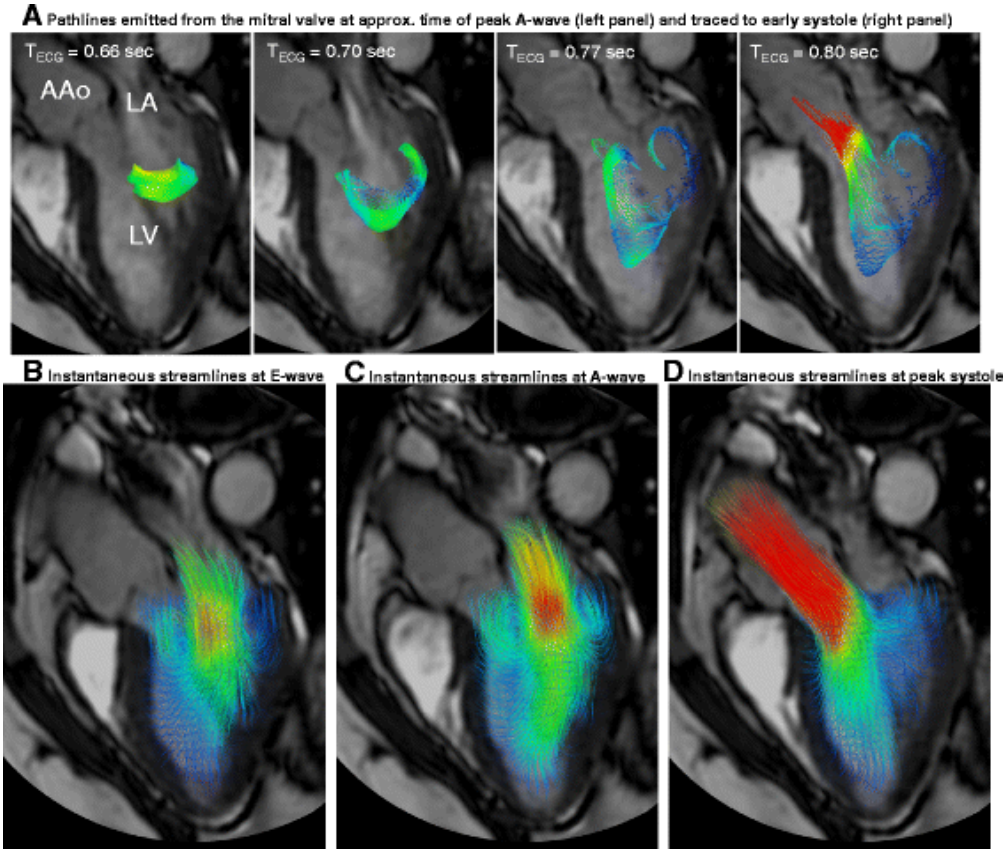

Figure 1.2: Example scans of the left ventricle produced using 4D-flow MRI. A shows velocity visualized as pathlines, which are trajectories that particles follow over time. B-D show velocity visualized as streamlines, which are lines tangent to the velocity vector at each point. Copyright Dyverfeldt et al. 2015 [2]. Reprinted courtesy of the Copyright Holder under a Creative Commons License CC BY 4.0

4D-flow MRI has been instrumental in developing today's understanding of flow in the heart, but it does not come without limitations. First, there is a direct trade-off between the maximum velocity that can be encoded and the signal-to-noise ratio of the velocity measurements [17]. In addition, the temporal and spatial resolution are low, making it difficult to capture complex flow structures (which are commonly predicted in simulation-based models), especially flow conditions close to the walls where thrombosis is thought to occur. Patients with metal implants such as a pacemaker or left ventricle assist device cannot undergo MR imaging. 4D-flow MRI is expensive, time-consuming, and is not widely

accessible. Due to its high costs and the effects of a strong magnetic field on magnetic implants, visualizing flow with 4D-flow MRI is not available to all patients. While 4D-flow MRI has been and continues to be instrumental in discovering more about blood flow in the heart, at this time its costs motivate alternative, more widely-available clinical imaging methods for routine evaluation and diagnosis of cardiac function.

Color-Doppler ultrasound, or color Doppler-echocardiography, is a method that uses ultrasound to measure the velocity magnitude parallel to the ultrasound beam. Color-Doppler ultrasound is an easy-to-use, widely available diagnostic tool used to visualize flow in the heart. It is much cheaper than MRI and it is becoming even more accessible with recent developments in hand-held ultrasound systems [18]. Color-Doppler ultrasound converts frequency shifts into velocity information, representing the flow speed using colors on top of a grayscale anatomical image (Figure 1.3).

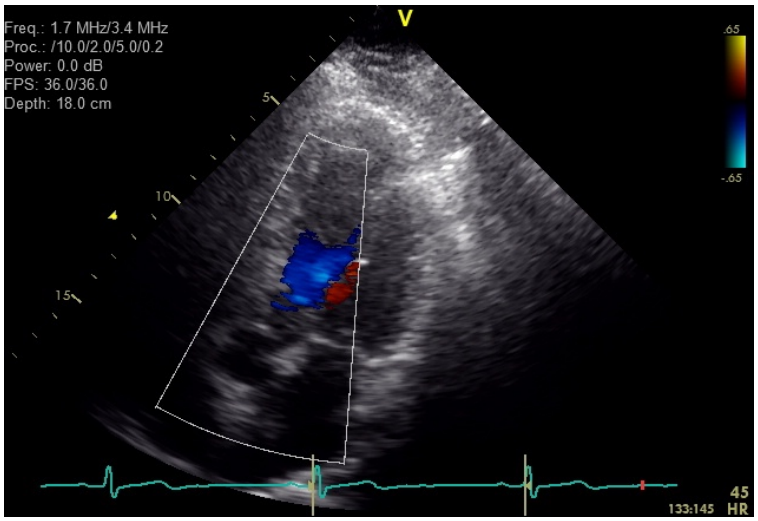

Figure 1.3: An example color-Doppler ultrasound scan of the left ventricle. The greyscale image contains the anatomy of the ventricle and the velocity magnitude is overlayed in color. The velocity magnitude represents the strength in the radial direction, where the 'V' represents the origin, i.e. the transducer location. Velocities are only collected inside the white box region.

Traditional ultrasound detects tissues by producing an ultrasonic wave and measuring the reflections of that wave. In order to measure velocities, multiple measurements are taken and the phase shifts between subsequent echos are used to calculate a velocity [19]. Because ultrasound works by sending and receiving sound waves, the gathered information is only in the direction that the wave is moving. Therefore, the flow information is only available in the beam direction, with the origin being the location of the transducer. The single-component measurement of the flow can be adequate for assessing the mostly uni-directional flow in vessels or through valves, but it is a significant limitation in assessing the highly multidirectional nature of blood flow inside of the heart [11].

While MRI and ultrasound have limitations in terms of measuring velocity fields in the

body, both have been instrumental in developing our understanding of heart disease and both are currently used in the diagnosis and treatment of heart disease.

1.4.2 Simulations

Computational fluid dynamics simulations are an alternative to blood flow imaging. Instead of imaging the movement of the flow directly, patient-specific simulations are produced by imaging the blood flow domain, i.e. the walls of the heart and the vessels, and then solving equations describing fluid movement to calculate the blood velocities throughout the domain. Imaging of the walls is often performed using MRI or computed tomography scans.

Simulations can be performed on just the left ventricle or the whole heart and can also include some vessels. The simulation results provide much higher resolution information for blood flow in both the time and space domain compared to imaging. However, simulations are computationally intensive and time consuming, and therefore their use in the clinic is limited. In addition, they require tuning of multiple parameters to achieve a valid solution, adding to their complexity and the difficulty of introducing them to the clinic.

In addition to higher resolution visualization, simulations also provide the ability to 'test' different situations. For example, multiple variations of a surgery can be modeled and compared via simulations before it is actually performed in a patient. As the ability to segment and mesh the geometry improves and necessary computation time shortens, these simulations will become an important clinical tool when it comes to diagnosis and treatment planning.

1.4.3 Evaluating Quality of Blood Flow in the Left Ventricle

Imaging is an important clinical tool for evaluating blood flow in the heart. For example, in the clinic, color-Doppler ultrasound is regularly used to evaluate valve regurgitation in the left ventricle and cardiac output [20]. Ultrasound, computed tomography, and cardiac MRI are all currently used in the diagnosis and treatment of congenital heart disease. Due to the versatility of MRI, including its ability to measure flow, Rajiah et al. argue the advantages of cardiac MRI over the other modalities, although they note that ultrasound is more widely accessible [21].

Outside of the clinic, imaging and simulations continue to be used to advance our understanding of heart disease. Some promising quantitative measures of flow quality include flow volume, wall shear stress, and turbulent kinetic energy [22]. Vortex formation and viscous energy loss have also been shown to be associated with health outcomes [14]. As this research continues to advance, some of these quantitative and qualitative measures that are both informative and implementable will be introduced to the clinic.

1.5 Overview and Principal Contributions of this Dissertation

This dissertation seeks to improve measurement and evaluation of blood flow in the heart using computational tools. Chapters 2 and 3 focus on improving color-Doppler ultrasound as a diagnostic tool. In Chapter 2 we seek to improve the calculation of a second, in-plane component of velocity from color-Doppler ultrasound data. In Chapter 3 we evaluate the ability of color-Doppler ultrasound to estimate two different diagnostic measures, kinetic energy and viscous dissipation rate, and propose modifications to the estimates. The first main contribution is introducing reduced dimensional estimates of kinetic energy and viscous dissipation rates for color-Doppler ultrasound data, presented in Chapter 3. Chapters 4 and 5 present a new modal analysis method to de-noise and reconstruct velocity fields measured from either 4D-flow MRI or color-Doppler ultrasound. The second main contribution is this new method to process 3D flow fields. It is presented generally in Chapter 4 and specifically for left ventricle applications in Chapter 5.

The first contribution is related to color-Doppler ultrasound, which is a very important imaging modality for the treatment of heart disease due to its availability in the clinic. Recent research has expanded the information available from traditional color-Doppler ultrasound images by solving for an extra component of velocity. However, some of these methods are developed from assumptions that are often not well satisfied and require multiple steps to process. The work in Chapter 2 provides a look at methods developed to solve for an extra component of velocity that avoid these assumptions. In Chapter 3, we introduce reduced dimensional estimates of kinetic energy and viscous dissipation rates that allow us to study diagnostic tools from color-Doppler ultrasound without having to perform extra steps to calculate an extra component of velocity.

The second contribution is an improved method for filtering and reconstructing noisy flow data from images. Due to the difficulty of imaging all types of flow, from blood flow inside the body to flow in the ocean, methods used to image flow fields produce noisy data, and a variety of different methods have been introduced to de-noise these datasets and fill in missing information. The open boundary modal analysis method introduced in Chapter 4 and studied further in Chapter 5 provides a few advantages over these methods. First, open boundary modal analysis enforces a divergence-free condition on the flow. Enforcing physical constraints on the flow are important for further analysis and evaluation of the flow field. Second, open boundary modal analysis enforces appropriate boundary conditions, which are also important for further analysis of the flow field. The way the boundary conditions are implemented also leaves room for the user to easily adjust boundary conditions based on which aspects of the data are more reliable. In addition, open boundary modal analysis can be used on a wide variety of data, from color-Doppler ultrasound data to 4D-flow MRI data to data from other, non-biological, applications.

Together, the work presented here provides multiple steps towards improved measurement and understanding of blood flow in the heart. As this research area continues to grow,

improved imaging of the flow fields will enable further analysis of how flow patterns are related to disease progression. Knowledge of these relationships will help doctors diagnose and treat heart diseases earlier in their development and will allow doctors and engineers to develop better tools for treatment, improving patient outcomes across heart diseases.

Chapter 2

Two-Dimensional Velocity Reconstruction from Color-Doppler Ultrasound

2.1 Introduction

In this chapter, we explore the estimation of a second, in-plane component of velocity from color-Doppler ultrasound data as a way to improve the value of color-Doppler ultrasound data in the evaluation of quality of blood flow in the left ventricle [23].

Color-Doppler ultrasound is a commonly used method to examine blood flow in the left ventricle. It uses a sound wave to measure the flow velocity in the direction of the ultrasound beam. This means that velocity information is only available in the direction parallel to the beam. In other words, only one component of velocity, V_r, is known (Figure 2.1), and the other two components are unknown. In order to have a better understanding of the quality of flow in the heart, more information is needed. As a result, several methods have been proposed to extract more information from the velocity field gathered by color-Doppler ultrasound.

Many of these methods solve for a second, in-plane component of velocity, also called the the azimuthal component of velocity, or V_θ. Figure 2.1 shows a simplified two-dimensional plane of the left ventricle, similar to what is captured in color-Doppler ultrasound data. Only the radial velocity field is measured from the ultrasound, and the azimuthal component is estimated from the given velocity and geometry information.

The majority of these methods to reconstruct the azimuthal component of flow rely on an assumption that the through-plane divergence is negligible, also known as the planar flow assumption.

For example, Garcia et al. [24] use the planar flow assumption combined with wall motion data gathered from B-mode echocardiography to calculate the azimuthal component of velocity. First, the gradient with respect to the radial direction of the radial component of velocity is calculated. Then, boundary conditions are set using the movement of the walls. Using the continuity equation, with the through-plane divergence set to zero, the azimuthal velocity is calculated. They validated these methods using particle image velocimetry mea-

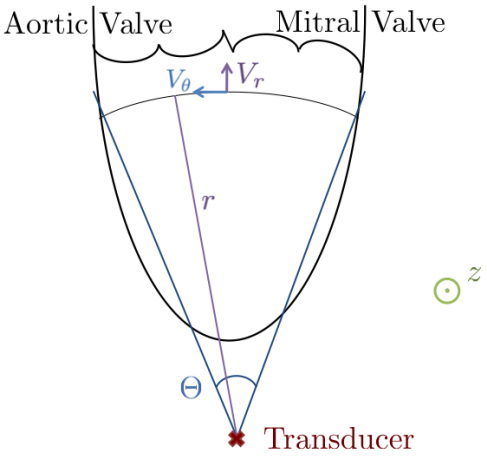

Figure 2.1: Long-axis view of a simplified left ventricle, as it would appear in an ultrasound image. The apex is located nearest the ultrasound transducer. Blood flows in through the mitral valve and out through the aortic valve.

surements of the velocity field in an atrioventricular duplicator and with MR data. They calculated relative errors of about 35% for the azimuthal velocity [24].

Uejima and Ohtsuki also used the planar flow assumption to reconstruct the azimuthal component of velocity from the radial component. This method involves splitting the flow field into a 'basic' component and a 'vortex' component. First, the 'vortex' component is reconstructed based on the assumption that the vortices are bilaterally symmetric and that there is no through-plane flow, and using the concept of a streamfunction. Then, the measured flow field that does not contribute to the 'vortex' component is used to reconstruct the 'basic' component. The two components are combined to build the full, two-dimensional flow field [25, 26].

These reconstruction techniques have since been used to study flow conditions using ultrasound data in diseased and healthy hearts. After reconstructing the velocity field from ultrasound data using Garcia et al.'s method, Hendabadi et al. used Lagrangian Coherent Structures to study boundaries of blood entering the left ventricle during different cycles, from residence time to general transport patterns [27]. Bermejo et al. also used the reconstruction to study vortex properties in the left ventricle in dilated cardiomyopathic and healthy hearts [20], and Rossini et al. studied blood transport in patients undergoing cardiac resynchronization therapy [28].

However, the validity of the planar flow assumption has come into question. It has been found that the magnitude of the through-plane divergence is comparable to the magnitude of the other components of divergence [29, 30]. To remedy this, Jang et al. proposed an alternative reconstruction method that accounts for through-plane divergence. They solve the Navier-Stokes equation for a changing, two-dimensional, left ventricle geometry over a cycle, and they include a source term that accounts for through-plane divergence [30]. The

measured radial velocity from the ultrasound serves as a constraint for the method.

The goal of this chapter is to investigate new methods to reconstruct the in-plane velocity field from color-Doppler ultrasound data without assuming that through-plane divergence is negligible.

2.2 Methods Overview

In this chapter, we develop and evaluate two new methods to calculate the second, in-plane component of velocity from color-Doppler ultrasound data without using the planar-flow assumption. The first method is 2D open boundary modal analysis (OMA). OMA projects a series of 'modes', or velocity fields, that are derived based on the geometry to the known velocity component onto the data in order to reconstruct a new, two-dimensional, flow field. The second method is a weighting method that builds on the continuity method described by Garcia et al. [24] by estimating the through-plane divergence and using this estimate in the reconstruction of the azimuthal velocity.

2.2.1 Note on Color-Doppler Ultrasound Data

Because color-Doppler ultrasound data only has one component of velocity, it is not possible to evaluate the success of the reconstruction methods using only this data. Instead, a data set where the true velocity field is available, such as one from a computational fluid dynamics (CFD) simulation can be subsampled to represent a color-Doppler ultrasound acquisition, and the methods can be tested on this data. Then the results can be compared to the true values from the simulation. For evaluation of LV flow fields, color-Dopper is usually collected from the apical long-axis plane. The transducer is placed beyond the apex of the left ventricle, so the imaging plane contains the apex at one end and goes through both the mitral and aortic valves at the base on the other end (Figure 2.1). To generate synthetic data set to represent color-Doppler ultrasound data, the apical long-axis plane is extracted from the full data (e.g. CFD data) set using a radial coordinate system where the origin is located where the transducer would be located in a typical ultrasound scan. The corresponding radial velocities are then "measured" from the full (e.g. CFD) to represent color Doppler. The azimuthal velocities are then computed from the "measured" radial velocity field using an appropriate reconstruction method, and then compared to the true azimuthal velocities from the original full data.

2.2.2 Data Sets Used

The reconstruction methods were tested on two types of data sets: results from a CFD simulation and phase-contrast MRI data. The CFD data includes three components of velocity on a 3D domain, so a single slice of the domain was selected to represent the slice that would be acquired in a color-Doppler acquisition. The MRI data is from a single plane

Patient	Venc	Contrast	Beat Period (s)	Time Resolution (s)	Spatial Resolution (mm)
4	24	75	1.142	.057	0.94
4	30	100	1.142	.057	0.78
5	14	75	1.063	.053	0.86
8	11	75	0.684	.034	0.94
9	12	75	1.063	.053	0.94

Table 2.1: List of scan and patient parameters for PCMR data sets from UCSD.

but contains all three components of velocity. The reconstructions were performed based on the in-plane radial velocity. For the CFD data, the errors in the reconstruction were measured by comparing the in-plane radial and azimuthal components of velocity from the reconstructed field to the in-plane velocity field from the data. For the MRI data, the measured data is noisy so the results are compared qualitatively but not quantitatively.

The CFD simulation was performed by the Computational Technology Laboratory led by Johan Hoffman at Kungliga Tekniska högskolan Royal Institute of Technology (KTH) in Sweden. The geometry for the simulation was created from ultrasound measurements of the inner wall of the left ventricle. An adaptive arbitrary Lagrangian-Eulerian space-time finite element solver was used to solve the incompressible Navier-Stokes equations in the heart [31]. This data is well suited for method validation because it consists of a three-dimensional, divergence-free velocity field. Data from the apical long-axis plane was extracted to test the reconstruction.

We then tested the reconstruction methods on a group of two-dimensional phase-contrast Magnetic Resonance (PCMR) data sets (Table 2.1). These PCMR data sets were provided by the del Álamo's Research Group at University of California, San Diego. Again, the apical long-axis plane was extracted, and two dimensions of in-plane velocity were available. The slice thickness was 8mm and the left ventricle was segmented manually. Each patient underwent multiple MR scans with different imaging parameters. The details can be found in [23]. The scans presented in this report are the scans that produced the best results. Unlike the CFD data, this data has noise in it and does not produce a divergence-free velocity field. However, also unlike CFD data, this data does not rely on modeling assumptions.

2.2.3 Error Calculations

To evaluate the quality of the different reconstruction types, the error was calculated:

$$E_i = \frac{\int_\Omega ||V_{i,true} - V_{i,reconstructed}||dS}{\int_\Omega ||V_{i,true}||dS} \tag{2.1}$$

where Ω is the apical long-axis plane of left ventricle at a given time point, and i refers to the type of error. For this data, the radial error, where $i = r$, the azimuthal error, where $i = \theta$,

and the velocity magnitude error, where i refers to the velocity magnitude, were calculated. The error was then averaged at each point in time in the cycle and plotted as a function of time. Error is displayed in figures as absolute error, as calculated by equation 2.1, but is converted to a percent in the text.

2.3 2D Open Boundary Modal Analysis

Open boundary modal analysis is a method described by Lekien et al. to reconstruct sparse and noisy flow data that we have adapted for flow in the left ventricle due to the similarity of the two problems. The method was designed for sparse, 2D oceanographic flow data with two types of boundaries - one where there is no flow on or through the boundary ('closed'), and one where there is flow through the boundary ('open') [32]. For oceanographic data, the area of interest is often enclosed only partially by the coast. Therefore, the coastline can be considered a 'closed' boundary and the rest of the edge of the domain where data is collected can be considered an 'open' boundary. This is also similar to a left ventricle, where the walls of the heart can be considered a 'closed' boundary and the valves can be considered an 'open' boundary. We adapted this method to reconstruct a single plane of flow in the left ventricle from ultrasound data.

In the oceanographic data, a domain is chosen such that the domain remains constant in time, and only a single set of modes needs to be calculated even though data from multiple time points is used. For the left ventricle, the domain is changing over time and a new set of modes is calculated at each time step.

For the oceanographic data, the boundary is chosen somewhat arbitrarily, perhaps influenced by feasible measurement locations. A different set of modes would be calculated if a different boundary was chosen. However, flow in the left ventricle is an 'internal flow', where the domain is inherent to the problem and the flow field is strongly influenced by this domain, making it a strong candidate for the 2D open boundary modal analysis method.

The following description of 2D open boundary modal analysis closely follows the work of Lekien et al. found in [32] with the main differences appearing in the implementation of the method.

2.3.1 Modal Analysis Methods

2D open boundary modal analysis is implemented by solving for two types of modes based on only the geometry of the domain, and then projecting the modes onto the available velocity data to get a new, reconstructed velocity field. The first type of mode is an 'interior mode'. Interior modes are based entirely on the geometry of the domain and have no-slip, no penetration boundary conditions. The second type of mode is a 'boundary mode' and allows for flow through the boundary. Once the modes are calculated, the available velocity data is projected onto the modes using a least squares method. The resulting reconstructed flow field is the sum of the modes, each multiplied by a constant, where the constants are

calculated such that the reconstructed field is closest to the original data (measured in the L_2 norm).

General Theory

The Helmholtz decomposition theory states that a two-dimensional vector field, u, in the $x-y$ plane, can be written as the sum of an irrotational and divergence-free component:

$$u = u_\psi + u_\sigma \tag{2.2}$$

where

$$u_\psi = \nabla \times \psi\hat{k} \tag{2.3}$$

is divergence-free and $\hat{k}$ points in the z direction, and

$$u_\sigma = \nabla\sigma \tag{2.4}$$

is irrotational. Explicitly, u can be written:

$$u = \nabla \times \psi\hat{k} + \nabla\sigma \tag{2.5}$$

We can isolate ψ and σ by applying $\nabla\times$ and $\nabla\cdot$ to u, shown in equations 2.6 and 2.7:

$$\nabla \times u = \nabla \times (\nabla \times \psi\hat{k}) + \nabla \times \nabla\sigma = -\Delta(\psi\hat{k}) + 0 = -\hat{k}\Delta\psi \tag{2.6}$$

$$\nabla \cdot u = \nabla \cdot \nabla \times \psi\hat{k} + \nabla \cdot \nabla\sigma = 0 + \Delta\sigma = \Delta\sigma. \tag{2.7}$$

Boundary Conditions

In our problem with domain Ω, we have two types of boundaries. The 'closed' boundary is the area where there is no flow through the boundary, and is denoted $\partial\Omega_0$. The 'open' boundary is the area where flow is allowed through the boundary and is denoted $\partial\Omega_1$. We can separate the normal and tangent components of velocity on the boundary:

$$\begin{aligned} u \cdot \hat{t} &= \hat{t} \cdot (\nabla \times \psi\hat{k}) + \hat{t} \cdot \nabla\sigma \\ &= \hat{n} \cdot \nabla\psi + \hat{t} \cdot \nabla\sigma \\ u \cdot \hat{n} &= \hat{n} \cdot (\nabla \times \psi\hat{k}) + \hat{n} \cdot \nabla\sigma \\ &= -\hat{t} \cdot \nabla\psi + \hat{n} \cdot \nabla\sigma. \end{aligned}$$

It is important to note that the decomposition of the flow, represented by equations 2.3 and 2.4, is not unique. A divergence-free or irrotational component could be added to each component respectively, and still satisfy equation 2.2. Therefore, we choose that u_ψ does not flow through the closed boundary, $\partial\Omega_0$: i.e.

$$0 = \hat{n} \cdot u_\psi = \hat{n} \cdot (\nabla \times \psi\hat{k}) = -\hat{t} \cdot \nabla\psi. \tag{2.8}$$

Since any constant can be added to ψ without changing the result, we choose that $\psi = 0$ on the closed boundary. This means that on closed parts of the boundary, $\hat{t} \cdot \nabla\psi = 0$ and therefore that $\hat{n} \cdot \nabla\sigma = 0$.

System Equations

This leads to the system of linear, partial differential equations:

$$\begin{cases} \Delta\sigma = \nabla \cdot u & \text{in } \Omega \\ n \cdot \nabla\sigma = 0 & \text{on } \partial\Omega_0 \\ n \cdot \nabla\sigma = g_\sigma(s) & \text{on } \partial\Omega_1 \end{cases} \tag{2.9}$$

and

$$\begin{cases} \Delta\psi = -\hat{k} \cdot (\nabla \times u) & \text{in } \Omega \\ \psi = 0 & \text{on } \partial\Omega_0 \\ \psi = g_\psi(s) & \text{on } \partial\Omega_1 \end{cases} \tag{2.10}$$

where the functions g_σ and g_ψ are dependent on the velocity field at the boundary. They are discussed further in section 2.3.1.

From here, two types of modes, interior and boundary, are developed. These modes, u_ψ and u_σ, are a set of basis functions for our velocity fields that span the set of square integrable velocities and satisfy all necessary boundary conditions [32]. Interior modes are independent of type of boundary ('open' or 'closed') and boundary modes take into account flow through the boundary.

Interior Modes

Interior modes do not take into account the different types of boundaries and are designed to have no flow through the boundary. The interior modes are a set of eigenmodes that satisfy the following equations:

$$\begin{cases} \Delta\sigma_i = \lambda_i^\sigma \sigma_i & \text{in } \Omega \\ n \cdot \nabla\sigma = 0 & \text{on } \partial\Omega \end{cases} \tag{2.11}$$

and

$$\begin{cases} \Delta\psi_i = -\lambda_i^\psi \psi_i & \text{in } \Omega \\ \psi = 0 & \text{on } \partial\Omega \end{cases} \tag{2.12}$$

where σ and ψ are normalized: $\|\sigma\| = 1$ and $\|\psi\| = 1$.

Boundary Modes

Boundary modes take into account flow through the boundary and have differing boundary conditions on the 'open' and 'closed' boundaries. The boundary modes are defined as follows:

$$\begin{cases} \Delta\sigma^b = \int_{\partial\Omega} g_\sigma(s) ds & \text{in } \Omega \\ n \cdot \nabla\sigma^b = g_\sigma(s) & \text{on } \partial\Omega \end{cases} \tag{2.13}$$

where s is the arc length along the boundary.

Equation 2.13 does not inherently provide a set of modes, like the eigenvalue problem for the interior problem does. Instead, for a known boundary condition, $g_\sigma(s)$, a single boundary mode will be defined. Therefore, if $g_\sigma(s)$ was known, then only one boundary mode would be necessary. However, $g_\sigma(s)$ is noisy and possibly sparse. Therefore, a basis is defined for $g_\sigma(s)$ such that $g_\sigma(s)$ is a sum of basis functions. A single boundary mode corresponds to a single basis function, $g_i(s)$, resulting in multiple boundary modes. The interior modes corresponding to the basis functions, σ_i^b, are defined as follows:

$$\begin{cases} \Delta\sigma_i^b = \int_{\partial\Omega} g_i(s)ds & \text{in } \Omega \\ n \cdot \nabla\sigma_i^b = g_i(s) & \text{on } \partial\Omega. \end{cases} \tag{2.14}$$

For this problem sinusoidal basis functions are used:

$$\{g_i(s)\} = \{1, ..., \sin(\frac{i\pi}{l}s), \cos(\frac{i\pi}{l}s), ...\} \tag{2.15}$$

where the arc length, s, ranges from 0 to l.

Velocity Field Reconstruction

The new, reconstructed velocity field is a sum of the interior and boundary modes, each multiplied by a constant:

$$\mathbf{u}_{new} = \sum_{i=1}^{n_1} \alpha_i^\psi \nabla \times \psi_i \hat{k} + \sum_{i=1}^{n_2} \alpha_i^\sigma \nabla\sigma_i + \sum_{i=1}^{n_3} \alpha_i^b \nabla\sigma_i^b \tag{2.16}$$

where n_1 represents the maximum number of ψ interior modes used, n_2 represents the maximum number of σ interior modes used, and n_3 represents the maximum number of boundary modes used.

The constants (α) are determined by minimizing the difference between the measured and reconstructed velocity fields in the L_2 norm (or a least squares minimization), as shown here:

$$\min_\alpha \|\mathbf{u}_{data} - \mathbf{u}_{new}\|_2^2$$

where $\mathbf{u}_{data}$ contains the velocity data information.

Multiple different numbers of modes were tested. In each case, equal numbers of σ modes and ψ modes, and double the number of boundary modes were used for each reconstruction. Then, a 'divergence-free' reconstruction was performed where no σ modes were used so that the resulting field satisfies the assumption used in the original method: that the through-plane divergence is negligible. For these cases, if n ψ modes were used, then $2n$ boundary modes were used.

2.3.2 Results

The open boundary modal analysis reconstruction method was tested on two different types of data, described in section 2.2.

Reconstruction from Computational Fluid Dynamics Simulation

First, the reconstruction method was tested on the CFD data. Reconstructions were performed using multiple different numbers of modes. For most reconstructions, there are n irrotational (σ) modes, n divergence-free (ψ) modes, and $2n$ boundary (σ_b) modes.

The reconstruction is calculated by minimizing the difference between the measured radial velocity and in the reconstructed radial velocity. Therefore, as the number of modes used in the reconstruction increases, the error of the reconstructed radial velocity error decreases (Figure 2.2a). The error of the reconstructed radial velocity was on the order of about 10-20% but doubled about 40% of the way through the cardiac cycle during diastole, before dropping back down about 60% of the way through the cycle. Ideally, increasing the numbers of modes used would also correlate with a decrease in the error in the azimuthal velocity. Unfortunately, this was not the case and average error of reconstructed azimuthal velocity actually increased with increasing number of modes (Figure 2.2b). In addition, even the lowest errors in azimuthal velocity averaged over 500% error, with most of the reconstructions averaging over 1000% error.

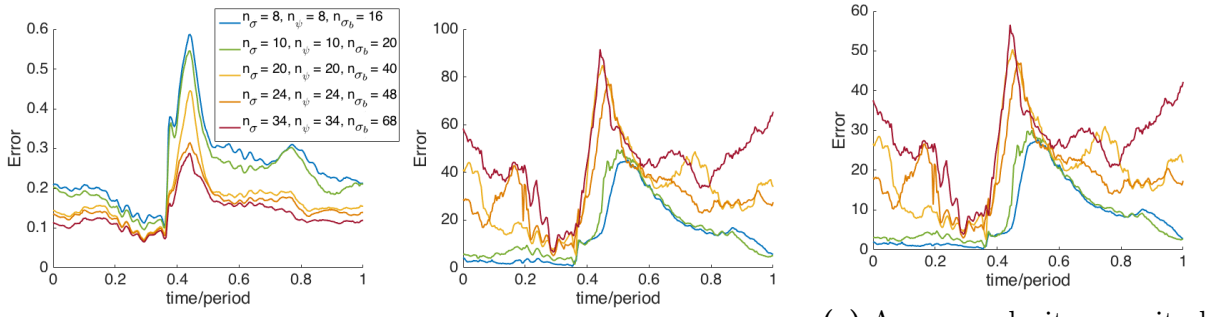

(a) Average V_r error **(b)** Average V_θ error **(c)** Average velocity magnitude error

Figure 2.2: Relative average velocity errors at each time point over the cycle for different numbers of modes for the open boundary modal analysis tested on KTH data.

Next, the reconstruction was performed using only the divergence-free modes and the boundary modes. This is akin to making the 'planar flow assumption' - that the through-plane divergence is negligible. Using only divergence-free modes significantly reduced the azimuthal and magnitude error in all cases, but there were still errors of over 100% in almost all of the cases (Figure 2.3). Like the previous version, the error peaked about 40% of the way through the cycle.

To better understand what is happening in the divergence-free reconstruction, velocity fields at two representative time points were examined (Figure 2.4). While similar structures are captured at both time points, the average error is much lower during the earlier point in the cycle (Figure 2.4b) than during the later part (Figure 2.4d). It appears that a large portion of this error is due to the large overestimation of velocity at the inlet at the later time point. Since OMA calculates a new radial velocity field in addition to a new azimuthal

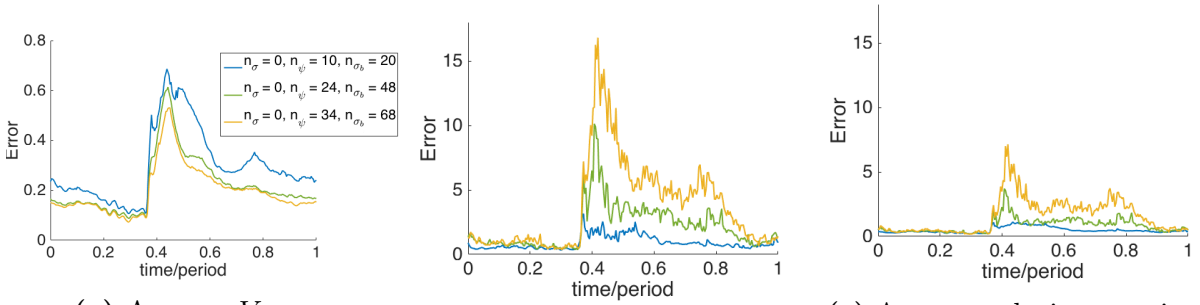

(a) Average V_r error

(b) Average V_θ error

(c) Average velocity magnitude error

Figure 2.3: Relative average velocity errors at each time point over the cycle for different numbers of divergence-free modes for the open boundary modal analysis tested on KTH data.

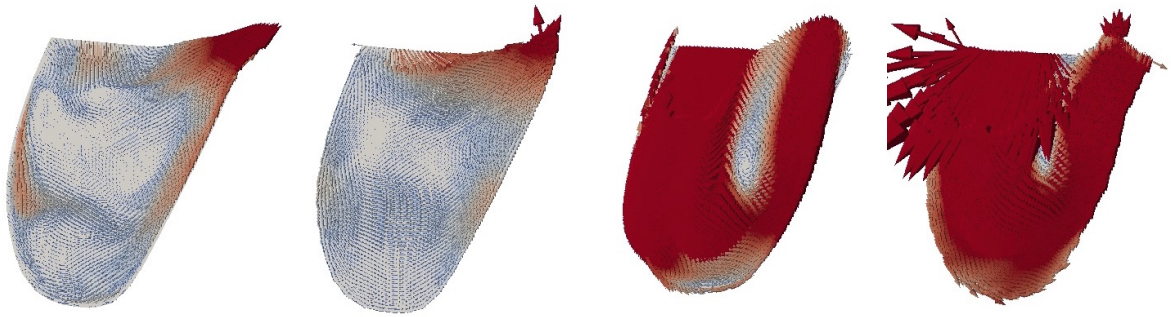

(a) Simulation result at t/T = 0.1.

(b) OMA reconstruction at t/T = 0.1.

(c) Simulation result at t/T = 0.5.

(d) OMA reconstruction at t/T = 0.5.

Figure 2.4: Snapshots of the velocity field at two different time points for the true KTH simulation result and for the OMA reconstruction using 10 divergence-free modes and 20 boundary modes.

velocity field, the large overestimates are seen in both the radial and azimuthal directions, even though the order of magnitude of error is one to two times less for the radial velocity (Figures 2.3a, 2.3b).

Reconstruction from PCMR Data

Next, the open boundary modal analysis method was tested on five different sets of PCMR data (Table 2.1). The five data sets are from four different patients. For one of the patients, two data sets were acquired with different scanning parameters. Again, for all cases, with increasing modes the error in radial velocity decreased, which is expected because the projection of the data onto the modes is completed by minimizing the errors between the original and new radial velocity fields. The error in azimuthal velocity did not follow the same decreasing pattern and was orders of magnitude higher than the radial velocity errors.

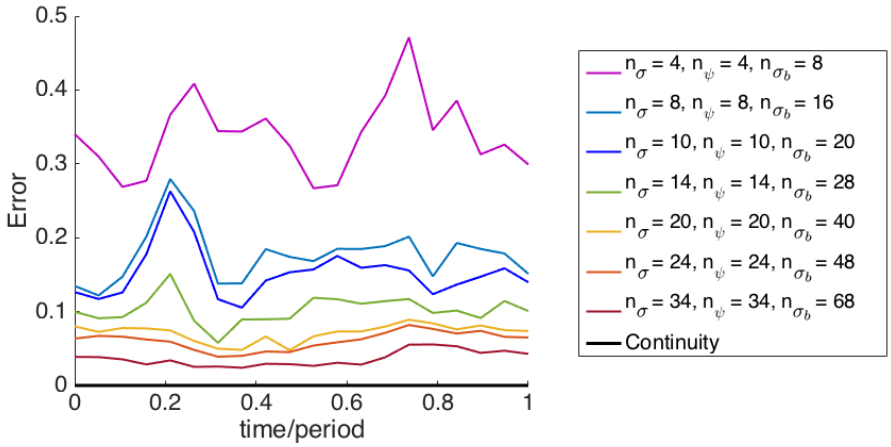

(a) Average V_r error

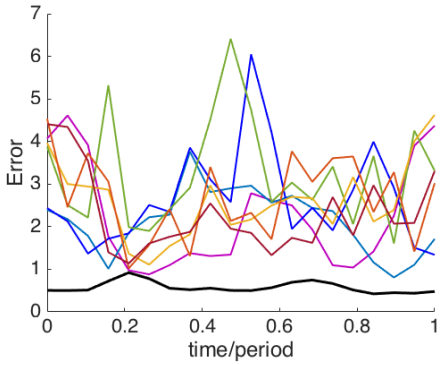

(b) Average V_θ error

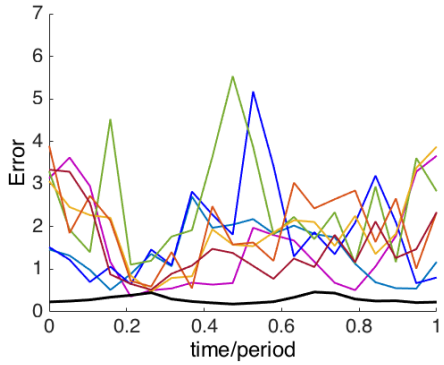

(c) Average velocity magnitude error

Figure 2.5: Relative average velocity errors at each time point over the cycle for different numbers of modes for the open boundary modal analysis tested on MRI patient 4a. The black line represents the results of the continuity equation described at the beginning of the weighted methods section (i.e. assuming through-plane divergence to be negligible).

The average errors were over 100% at almost every time point, and averaged around 400% for all cases (Figure 2.5).

Then, the PCMR data was reconstructed using only divergence-free and boundary modes. The error was lower using the divergence-free reconstruction than using the original reconstruction, with the azimuthal velocity error averaging around 100% for all cases (Figures 2.6 - 2.10). These resulting velocity fields were visually very similar to those that resulted from the continuity method, and the error over the cycle followed similar trends to the error in the continuity method. This is an expected result as both methods make the same assumptions about the flow field.

Overall, the errors calculated for the CFD data were much higher than the errors for the PCMR data, especially at their peak. This was true for both radial velocity and azimuthal

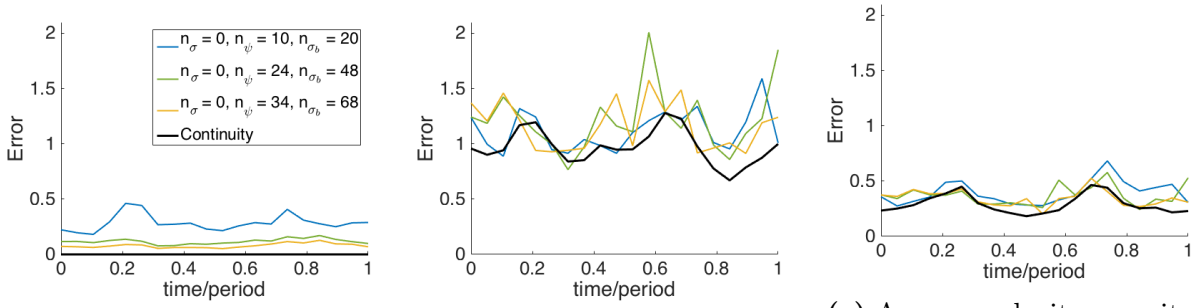

(a) Average V_r error **(b)** Average V_θ error **(c)** Average velocity magnitude error

Figure 2.6: Relative average velocity errors at each time point over the cycle for different numbers of divergence-free modes for the open boundary modal analysis tested on MRI patient 4a.

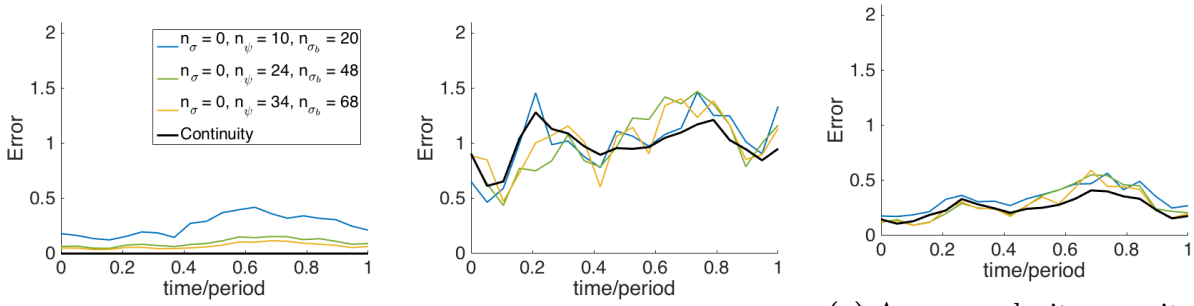

(a) Average V_r error **(b)** Average V_θ error **(c)** Average velocity magnitude error

Figure 2.7: Relative average velocity errors at each time point over the cycle for different numbers of divergence-free modes for the open boundary modal analysis tested on MRI patient 4b.

velocity. Since the error was higher for the CFD data than the PCMR data for the radial velocity, this indicates that the modes were able to more accurately represent the PCMR data than the CFD data. The open boundary modal analysis method had difficulty with the large velocities coming into the ventricle during diastole, and overestimated the magnitude in the azimuthal and radial directions.

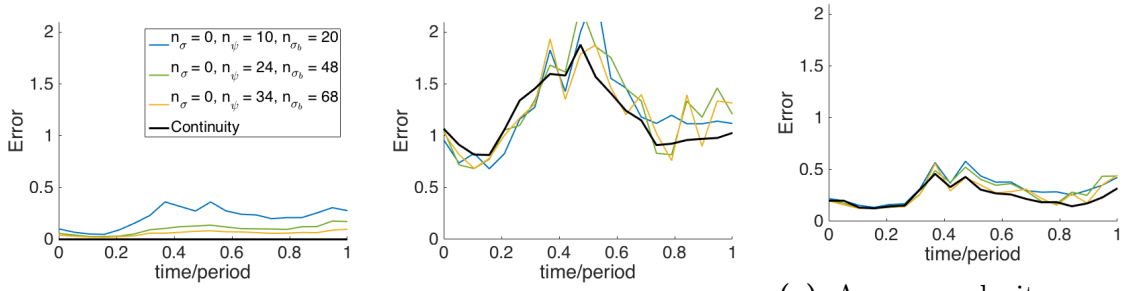

(a) Average V_r error **(b)** Average V_θ error **(c)** Average velocity magnitude error

Figure 2.8: Relative average velocity errors at each time point over the cycle for different numbers of divergence-free modes for the open boundary modal analysis tested on MRI patient 5.

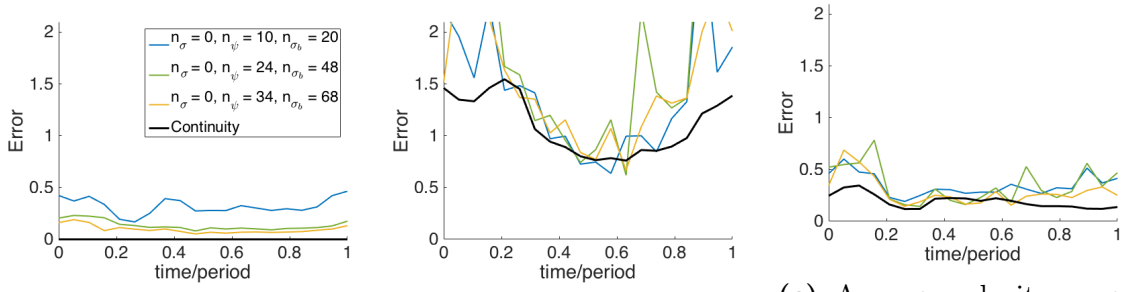

(a) Average V_r error **(b)** Average V_θ error **(c)** Average velocity magnitude error

Figure 2.9: Relative average velocity errors at each time point over the cycle for different numbers of divergence-free modes for the open boundary modal analysis tested on MRI patient 8.

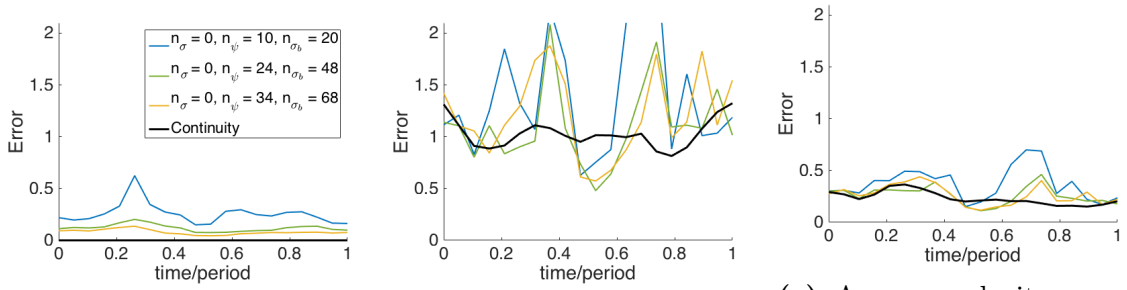

(a) Average V_r error **(b)** Average V_θ error **(c)** Average velocity magnitude error

Figure 2.10: Relative average velocity errors at each time point over the cycle for different numbers of divergence-free modes for the open boundary modal analysis tested on MRI patient 9.

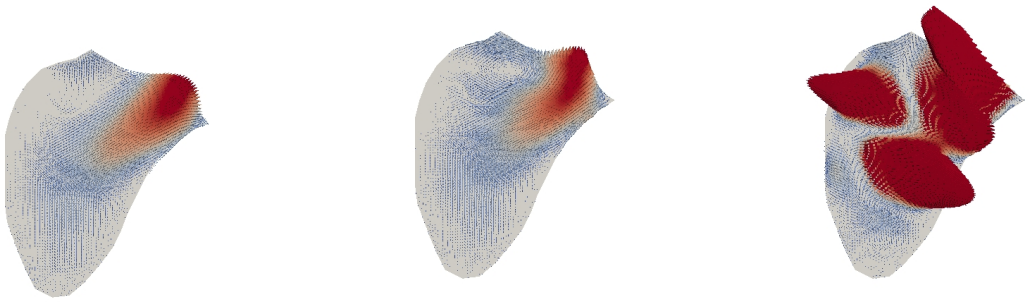

(a) Collected MRI data.

(b) Reconstructed with $n_\sigma = 0$, $n_\psi = 34$, $n_{\sigma_b} = 68$.

(c) Reconstructed with $n_\sigma = 34$, $n_\psi = 34$, $n_{\sigma_b} = 68$.

Figure 2.11: Snapshots of the velocity field using all types of modes or only divergence-free and boundary modes for a single timepoint during systole for the KTH data.

2.4 Weighted Method

The weighted method of 2D velocity reconstruction from color-Doppler ultrasound data is an extension of the method described by Garcia et al. [24]. In the original method, it is assumed that the through-plane component of divergence is negligible. To implement this, the $\frac{\partial V_z}{\partial z}$ term in the continuity equation is taken to be 0. The weighted method does not make the same assumption, and instead estimates the through-plane divergence and replaces the $\frac{\partial V_z}{\partial z}$ term with this estimate in the continuity equation.

2.4.1 Methods

Blood is assumed to be incompressible, and therefore satisfies the continuity equation:

$$0 = \frac{V_r}{r} + \frac{\partial V_r}{\partial r} + \frac{1}{r}\frac{\partial V_\theta}{\partial \theta} + \frac{\partial V_z}{\partial z}. \tag{2.17}$$

Since V_r is calculated in a specific plane by color-Doppler ultrasound, and therefore known, $\frac{\partial V_r}{\partial r}$ can be estimated using a second order finite difference scheme, leaving two unknown terms.

A 2D continuity method assumes that $\frac{\partial V_z}{\partial z}$ is negligible, leaving only one unknown term. To reconstruct the velocity field, $r\left(\frac{V_r}{r} + \frac{\partial V_r}{\partial r}\right)$ is calculated throughout the field. For a 2D continuous flow field, this is eqaul to $\frac{\partial V_\theta}{\partial \theta}$. Then, V_θ is calculated across each arc in the data, or across each row of constant r. On each wall of the left ventricle, the velocity is estimated based on wall movements. From these estimates, two boundary conditions are derived, providing two different solutions to V_θ. The results are averaged. This method is described in detail by Garcia et al. [24] and has been used to evaluate multiple different measures of cardiac function in other studies [11, 27, 28].

However, for this project, an estimate of $\frac{\partial V_z}{\partial z}$ was calculated and included in the calculation of V_θ.

Calculating $\frac{\partial V_z}{\partial z}$

The term $\frac{\partial V_z}{\partial z}$ is estimated using a control volume analysis. The control volume used is a single arc (or row with constant r) across the left ventricle. An example arc can be seen in figure 2.12 and the control volume can be seen in figure 2.13.

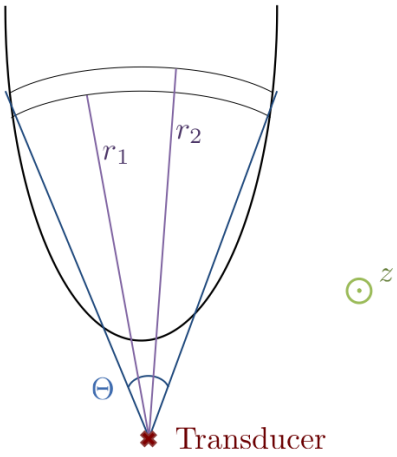

Figure 2.12: A left ventricle with a single arc marked. The angle along with the two radii defining the control volume are defined.

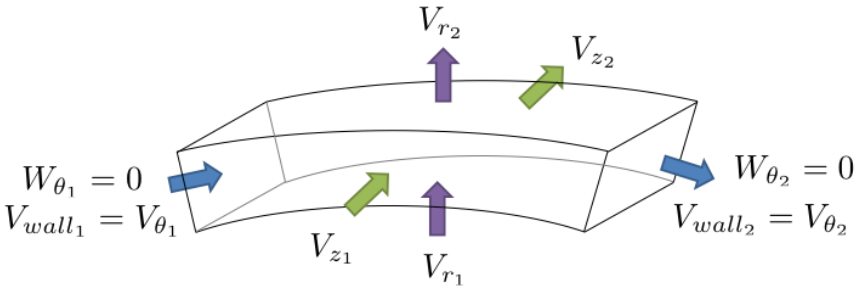

Figure 2.13: Control volume across an arc to calculate $\frac{\Delta V_z}{\Delta z}$.

Throughout this section, $\mathbf{V}$ refers to the velocity of the fluid, $\mathbf{V}_{CS}$ refers to the velocity of the control surface, and $\mathbf{W}$ is the difference:

$$\mathbf{W} = \mathbf{V} - \mathbf{V}_{CS}. \tag{2.18}$$

In a given control volume examined in this problem, the control volume is deforming because the walls of the ventricle are changing position. However, the control volume does not move in the r or z directions. There is no flow through the walls, but there is flow in both the radial and z directions (Figure 2.13).

The Reynold's Transport Theorem states that for a given control volume (CV),

$$\frac{DM_{sys}}{Dt} = \frac{\partial}{\partial t}\int_{CV} \rho d\,V + \int_{CS} \rho \mathbf{W}\cdot\hat{\mathbf{n}} dA = 0. \tag{2.19}$$

For this particular problem,

$$\frac{\partial}{\partial t}\int_{CV} \rho d\,V = \frac{\partial}{\partial t}\big(\rho(dz)\pi(r_2^2 - r_1^2)\frac{\Theta}{2\pi}\big) \tag{2.20}$$

where r_2 is the outer radius, r_1 is the inner radius, dz is the depth of the control volume, and Θ is the total angle of the control volume between the two walls of the left ventricle. Θ is a function of time. V_{r_1}, V_{r_2}, V_{z_1}, and V_{z_2} are also functions of time, and are taken as averages across the arc for a specific control volume. The next term is evaluated:

$$\int_{CS} \rho \mathbf{W}\cdot\hat{\mathbf{n}} dA = \rho\bigg(V_{r_1}A_{r_1} - V_{r_2}A_{r_2} + (V_{z_1} - V_{z_2})A_z\bigg) \tag{2.21}$$

where A_{r_1}, A_{r_2}, and A_z are areas of the bottom wall, top wall, and walls in the z plane respectively. The areas are all functions of time, defined as follows:

$$A_{r_1} = r_1\Theta\Delta z \tag{2.22}$$

$$A_{r_2} = r_2\Theta\Delta z \tag{2.23}$$

$$A_z = \pi(r_2^2 - r_1^2)\frac{\Theta}{2\pi} = \frac{1}{2}(r_2^2 - r_1^2)\Theta. \tag{2.24}$$

Using this and defining $\Delta V_z = V_{z_1} - V_{z_2}$, it follows that

$$0 = \frac{\partial}{\partial t}\big(\rho(\Delta z)\pi(r_2^2 - r_1^2)\frac{\Theta}{2\pi}\big) + \rho\bigg(V_{r_1}r_1\Theta\Delta z - V_{r_2}r_2\Theta\Delta z + (\Delta V_z)\frac{1}{2}(r_2^2 - r_1^2)\Theta\bigg) \tag{2.25}$$

Next, $\frac{\Delta V_z}{\Delta z}$ is isolated by dividing by ρ since the problem is incompressible

$$\frac{\Delta V_z}{\Delta z} = -\frac{\bigg(\frac{1}{2}(r_2^2 - r_1^2)\frac{\partial}{\partial t}(\Theta) + V_{r_1}r_1\Theta - V_{r_2}r_2\Theta\bigg)}{\frac{1}{2}(r_2^2 - r_1^2)\Theta} \tag{2.26}$$

In equation 2.26, all the terms on the right hand side are known, but $\frac{\partial}{\partial t}(\Theta)$ is calculated using a central difference scheme based on the locations of the wall at different time points.

$$\frac{\partial\Theta(t)}{\partial t} \approx \frac{\Theta(t+dt) - \Theta(t-dt)}{2dt} \tag{2.27}$$

At this point, all the necessary terms in equation 2.26 have been calculated and can be plugged in to solve for $\frac{\Delta V_z}{\Delta z}$.

2.4.2 Results

Reconstruction from Computational Fluid Dynamics Simulation

The CFD 'pointwise' reconstruction created velocity fields with the lowest error and did the best job at capturing many of the structures that were present in the simulation. Theoretically, if the calculations for all the components of divergence and the boundary conditions were exact, then the azimuthal component of velocity could be calculated exactly. However, the divergence calculations and the boundary conditions are discrete, which requires voxel averaging and means that the divergence calculations and boundary conditions are not exact. In addition, the reconstructed velocity fields have singular points of highly overestimated azimuthal velocity (Figure 2.16b). This is likely caused by a very large w that is a result of a very small radial divergence, since the radial divergence is on the denominator in the calculation of w.

In addition, reconstructions were performed on both filtered and unfiltered data sets. The results were much better when the radial velocity was filtered prior to reconstruction (Figures 2.14, 2.15). Additionally, the method with an average 'w' used across each arc performed the worst, with azimuthal errors averaging around 400% (Figure 2.14). These data sets were left out of subsequent plots.

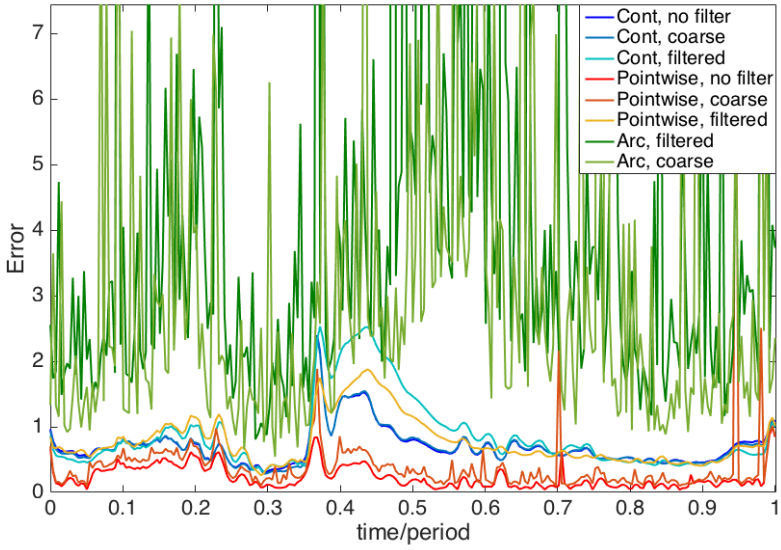

Figure 2.14: Relative average V_θ errors at each time point over the cycle for different methods of the weighted reconstruction on the KTH simulation data. 'Cont' refers to the original continuity method. 'Pointwise' refers to the pointwise reconstruction method. 'Arc' refers to the reconstructions where w was averaged across each arc. If there is no indication of whether the filter was applied, then the filter was not applied. Coarse refers to the reconstructions that were performed on a coarser grid.

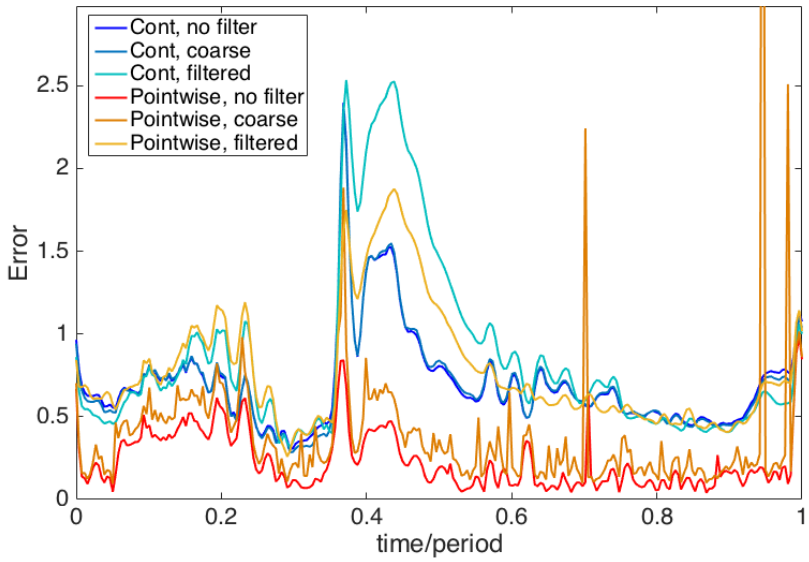

(a) Average V_θ error

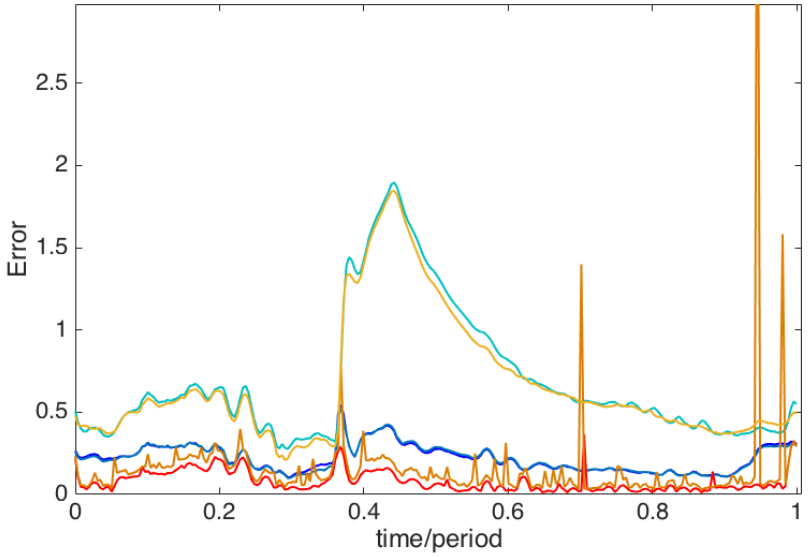

(b) Average velocity magnitude error

Figure 2.15: Relative average velocity errors at each time point over the cycle for different methods of the weighted reconstruction on the KTH simulation data. 'Cont' refers to the original continuity method. 'Pointwise' refers to the pointwise reconstruction method. If there is no indication of whether the filter was applied, then the filter was not applied. Coarse refers to the reconstructions that were performed on a coarser grid.

The 'pointwise' reconstruction, where the through-plane divergence was calculated at each point and the azimuthal velocity was reconstructed based on this calculation, gave the results with the lowest error of any method. However, when the weighting term was averaged across the arc, the error was larger than the error for any of the other variations on the method. The reason for this large increase in error is due to the large variations across each arc. In some cases, there are values for w that are very large or very small at just one point on an arc, so when w is averaged, the very small or large value dominates the averaged term.

For the CFD data, results calculated from the coarse and the fine grid were comparable to each other. The coarse grid was on the order of resolution of what is typically seen from ultrasound data and the fine grid was 10 times more resolved in each direction.

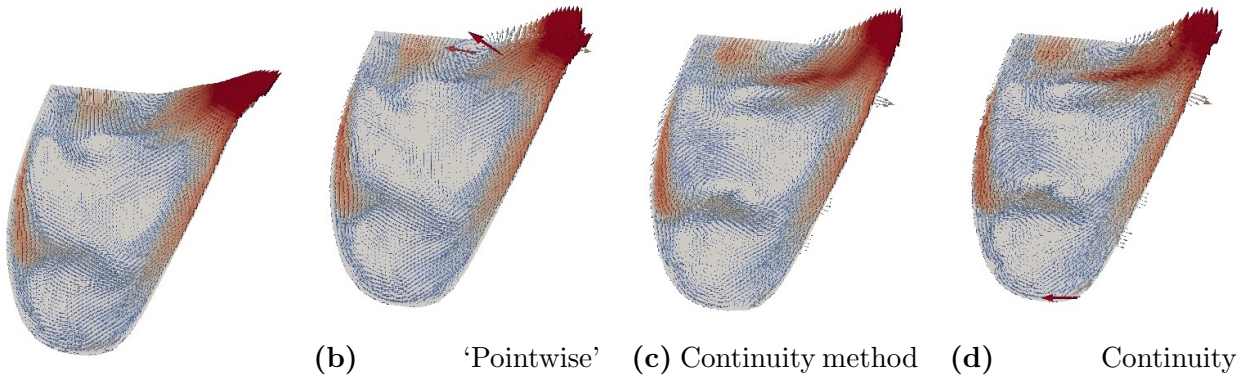

(a) Simulation result.

(b) 'Pointwise' weighted reconstruction on a fine grid without filtering.

(c) Continuity method reconstruction without filtering on a coarse grid.

(d) Continuity method reconstruction without filtering on a fine grid.

Figure 2.16: Snapshots of the velocity field using different reconstruction methods from a single timepoint during systole for the KTH data.

Reconstruction from PCMR Data

Unlike for the CFD data, a 'pointwise' reconstruction could not be done for the PCMR data because velocity data was only available in a single plane. Instead, the through-plane divergence was estimated across each arc using the control volume analysis. This method did not provide any improvement to the continuity method for the MRI data, which is a result that follows directly from the poor results seen in the CFD data when w was averaged across arcs for the reconstruction (Figure 2.17).

Notably, there were many areas of very large azimuthal velocity. This problem was seen in the CFD data as well, where areas of small radial divergence cause an overestimate of w, since radial divergence is on the denominator of w. To decrease the effects of this issue, a slight variation on the method was implemented where there is a maximum value for w, and if the magnitude of the calculated w was larger, it was reassigned to the lower, more

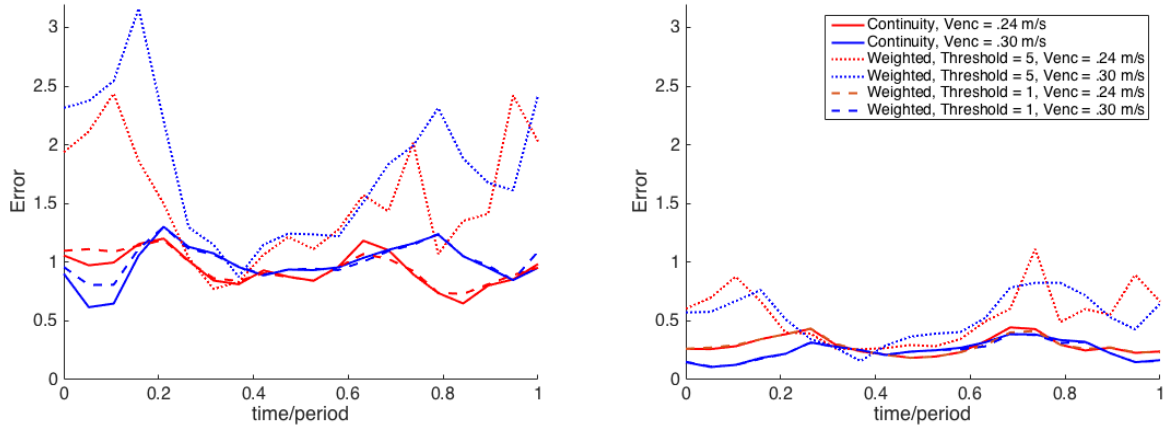

(a) Average V_θ error **(b)** Average velocity magnitude error

Figure 2.17: Relative average velocity errors at each time point over the cycle for the weighted method tested on MRI patient 4 for two different velocity encoding values. Solid lines represent the results for patient 4, $V_{enc} = .24m/s$ and dashed lines represent the results for patient 4, $V_{enc} = .30m/s$.

physiological value. To test this, w was capped at 1 and at 5. When w is capped at a magnitude of 1, the results are very close to those seen with the the regular continuity method. Since this saw a lower error, it appears that it would be a waste of computational time to try and estimate w when the results are the same as or worse than if the original continuity method is used.

2.5 Conclusions

The purpose of this chapter was to explore 2D velocity reconstruction methods for color-Doppler ultrasound data in the long-axis apical plane of the left ventricle that did not rely on a divergence-free assumption, motivated by evidence that the divergence-free assumption was often not well satisfied. Two methods were investigated, a '2D open boundary modal analysis' method and a 'weighted' version of the previously explored continuity method. However, both methods produced results with relatively large errors, and these errors were reduced when the divergence-free assumption was re-introduced into these methods.

The open boundary modal analysis method calculates a set of modes based on the geometry of the ventricle, and then projects the available data onto these modes. The large errors in the velocity fields produced from this method are likely due to many local minimum available in the projection of the data onto the modes. The under-constrained nature of the problem suggests that additional constraints are needed to get an improved reconstruction. One such constraint was the divergence-free assumption, the exact assumption that we were seeking to avoid. When this assumption was re-introduced, the errors dropped to around

the same values as using the original continuity method. While these errors were still higher than desirable, we saw that this assumption was necessary to produce any sort of reasonable results.

These results prompted an exploration of alternatives to the 2D divergence-free assumption. One way that we approached this problem was by moving into the 3D domain. With advancements in ultrasound, measuring 3D data is becoming more and more accessible. With geometry and velocity information available in a 3D domain even with only the radial component of velocity available, extra constraints are introduced to the problem. We explore 3D open boundary modal analysis in Chapters 4 and 5.

The weighted method was a modified version of the continuity method that introduced an extra term to account for through-plane divergence. The extra term averaged through-plane divergence across individual arcs. However, through-plane divergence often varied greatly across individual arcs, meaning that the extra term was a poor representation of the through-plane divergence at individual points. In many cases, ignoring through-plane divergence produced a better result than the weighted method.

Through all of these methods, the main goals are related to improving our understanding, diagnosis, and treatment of heart disease. Ultimately, we are interested in a method that enables us to qualify or quantify heart health, even if our velocity field is not error-free. Therefore, in Chapter 3 we explore different estimates of kinetic energy and viscous dissipation calculated from limited velocity information in the left ventricle. These estimates are derived directly from the radial component of velocity, avoiding the divergence-free assumption, and from reconstructed velocity fields that use the divergence-free assumption.

As technology advances and we continue to better understand blood flow in the body, ultrasound remains a very important tool due to its low cost and high accessibility compared to other imaging modalities. Information learned from studying 4D flow MRI data and simulations can continue to be combined with measurements obtained from color-Doppler ultrasound to improve the diagnosis and treatment of heart disease.

Chapter 3

Calculating Kinetic Energy and Viscous Dissipation Rate from Color-Doppler Ultrasound Data

3.1 Introduction

Characteristic flow patterns in the left ventricle have been shown to be associated with heart disease, which has the potential to be leveraged to improve diagnosis and treatment of heart disease [11], but there is still much to be understood about exactly how flow patterns are related to disease and disease progression. Two metrics that have been linked to heart health are kinetic energy and viscous dissipation rate of blood flow in the left ventricle. However, the difficulty of imaging blood flow has contributed to difficulty in understanding the relationship between flow structures and disease, so this chapter focuses on evaluating these metrics from limited velocity information. In particular, this study focuses on our understanding of these metrics from color-Doppler ultrasound data, where only one component of velocity is measured on a single plane.

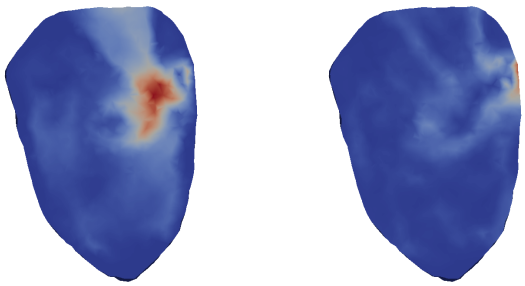

Figure 3.1: Kinetic energy (left) and viscous dissipation rate (right) mapped across a left ventricle during diastole, with red corresponding to high levels of kinetic energy and viscous dissipation rate and blue corresponding to low values.

3.1.1 Kinetic Energy in The Left Ventricle

Many studies have shown that there are differences in kinetic energy levels in the left ventricle between healthy and diseased patients, with the majority using 4D-flow magnetic resonance imaging (MRI). In 2015, kinetic energy was shown to be higher in diseased tetralogy of Fallot patients than healthy controls, although the difference was not statistically significant [33]. In myocardial infarction patients, kinetic energy in the left ventricle was significantly lower than in healthy patients, and flow patterns were also significantly different between myocardial infarction patients with and without thrombus formation in the left ventricle [34, 35]. In other studies, significant differences have been found in kinetic energy measures taken at specific times in the cycle or normalized by various values. Systolic kinetic energy was higher in heart failure patients than healthy controls, and three distinct patterns in kinetic energy over time were identified [36]. Peak diastolic kinetic energy, when indexed to stroke volume, was significantly lower in patients with Fontan circulation than healthy controls [37]. Peak diastolic kinetic energy, indexed to ventricular volume, decreased with age and peak diastolic kinetic energy of patients with left ventricular dysfunction was comparable to the older healthy individuals [38].

In addition to a sum of kinetic energy calculated across the entire left ventricle, kinetic energy in subsets of the ventricle have also been studied. In a comparison of the kinetic energy measured throughout the ventricle versus in only the short-axis, base-to-apex plane, it was found that the proportion of kinetic energy captured in the short-axis plane was the same between controls and myocardial infarction patients without thrombus, but was higher in myocardial infarction patients with thrombus than myocardial infarction patients without thrombus [35]. In addition to 4D-flow MRI, echocardiographic particle image velocimetry, which captures 2D velocity information in a single plane, was also used to measure kinetic energy, with results showing that kinetic energy fluctuations over a cycle were an important predictor of major adverse cardiac events in patients with chronic heart failure [39]. These studies indicate that estimates of kinetic energy in subsets of the left ventricle are correlated with kinetic energy in the entire ventricle and therefore have the potential to be used as diagnostic tools.

3.1.2 Viscous Dissipation Rate in The Left Ventricle

Viscous dissipation rate, often referred to as kinetic energy loss or flow energy loss, has also been shown to be lower in healthy than diseased patients using simulations and 4D-flow MRI, which both provide a 3D velocity field. In 2005, the natural angle of the mitral valve was shown to minimize flow energy losses in the left ventricle compared to other angles based on the results of simulations [40]. Using 4D-flow MRI, it was found that viscous energy losses were correlated with different types of vortices in the left ventricle, and viscous energy losses were higher in atrioventricular septal patients than healthy volunteers [14]. Changes in the vortex in the left ventricle associated with aortic regurgitation are correlated with higher viscous energy dissipation [41]. In Fontan patients, energy losses evaluated using 4D-

flow MRI were significantly elevated when compared to healthy controls [42]. These studies showed that in healthy patients, viscous dissipation rates were lower than in diseased patients. In many cases, the studies also explored the relationship between the vortex formation in the left ventricle and patterns in viscous dissipation rates.

Other studies explored the reliability of measuring viscous dissipation rate. In 2018, the scan-rescan reproducibility of diastolic kinetic energy and dissipation rates was shown to be high for healthy patients when calculated from 4D-flow MRI [43]. In another study, it was noted that calculation of viscous dissipation is dependent on image resolution, with higher values calculated from finer resolutions. However, relative viscous dissipation rates were maintained between patients [44]. While rate of viscous dissipation appears to be a promising diagnostic tool, image resolution is machine dependent so the variation in viscous dissipation with image resolution is an important consideration in further study of viscous dissipation rate.

3.1.3 Measurements in 2D

Although these prior studies examine kinetic energy and viscous dissipation rate in 3D using either simulations or 4D-flow MRI data, color-Doppler ultrasound is a more commonly used, less expensive method for examining blood flow in the clinic. However, color-Doppler ultrasound only measures a single, radial, component of blood velocity in a single plane. Therefore, it is of interest to study estimates of kinetic energy and viscous dissipation rate using this type of data.

Often, when using color-Doppler ultrasound data to evaluate blood flow, a second, in-plane (azimuthal) component of velocity is calculated from the collected data. Then, diagnostic metrics can be estimated from two, in-plane, components of velocity, as discussed in Chapter 2. However, the reconstruction of the second component of velocity relies on a '2D' assumption where the through-plane component of divergence is taken to be negligible. Some studies have shown that this assumption still allows for good reconstruction of the in-plane velocity component [24] or calculation of diagnostic measures [28], but others have shown that this assumption is over-simplified [29, 30], which is also discussed in Chapter 2.

A few groups have studied viscous dissipation rates using in-plane velocity data from color-Doppler ultrasound, where the measured radial component of velocity is used and the second, azimuthal component of velocity is calculated from the radial component. In 2013, a vector flow mapping method was used to reconstruct the in-plane component of velocity and flow energy losses were examined as a potential indicator of flow quality [45]. The same method was used in 2015 to determine baseline values of flow energy losses in children for future comparison [46], and in 2017 to determine baseline values of energy loss in adults [47]. It was also noted that energy loss values were correlated with age and heart rate in the healthy children [46]. In patients who had mitral valve surgery, ejection fraction and type of surgery were shown to affect postoperative energy losses in the left ventricle [48]. In a study on diabetic patients, diastolic dissipative energy losses were increased in diabetic patients compared to healthy controls and systolic dissipative energy losses were increased in diabetic

patients with uncontrolled blood glucose [49]. Energy losses have also been evaluated in dogs, where energy losses measured from a single plane using color-Doppler ultrasound increased when aortic regurgitation was present, and the diastolic energy losses were proportional to the severity of regurgitation [50].

In these 2D estimates of viscous dissipation rate from color-Doppler ultrasound data, the second component of velocity is calculated from the first component of velocity. To avoid assumptions made in the calculation of the second component of velocity, in this study, we propose 1D estimates of kinetic energy and viscous dissipation rate that rely on the single, measured component of velocity collected from color-Doppler ultrasound. We expect that because the 1D estimates do not rely on the same 2D assumptions, that the results will be as valuable as a diagnostic tool as the 2D estimates of kinetic energy and viscous dissipation rate, and much easier to calculate. We will compare the 1D estimates to 2D estimates in synthetic vortices, and we will compare 1D and 2D estimates to the true 3D kinetic energy and viscous dissipation rate in 3D flow fields in the left ventricle.

3.2 Methods Overview

In this section, we outline the 1D and 2D estimates of kinetic energy and viscous dissipation rate. The measures are introduced in their polar forms because color-Doppler ultrasound in the left ventricle is typically collected on a polar grid.

3.2.1 Kinetic Energy

Kinetic energy is defined as:

$$KE_{3D} = \frac{1}{2}m\|\mathbf{u}\|^2 = \frac{1}{2}m(u_r^2 + u_\theta^2 + u_z^2). \tag{3.1}$$

The 3D estimate is the sum of the kinetic energy at each point in the flow field integrated across the ventricle:

$$KE_{3D} = \frac{1}{2}\rho \int_V (u_r^2 + u_\theta^2 + u_z^2) r d\theta dr dz \tag{3.2}$$

where ρ is the density of blood, which is constant across the ventricle, and V is the entire ventricular volume.

For the reduced 1D and 2D estimates, we develop measures that can be calculated from color-Doppler ultrasound data, where only a single plane of data is available. The resulting estimates are:

$$KE_{2D} = \frac{1}{2}\rho \int_A (u_r^2 + u_\theta^2) r d\theta dr$$

$$KE_{1D} = \frac{1}{2}\rho \int_A (u_r^2) r d\theta dr$$

where A is the extracted plane from the left ventricle.

3.2.2 Viscous Dissipation Rate

The rate of dissipation of mechanical energy, per unit mass of fluid, is defined:

$$\phi_{3D,Cartesian} = \sum_i \sum_j \frac{2\mu}{\rho}\left[\left(\frac{1}{2}\left(\frac{\partial u_i}{\partial x_j} + \frac{\partial u_j}{\partial x_i}\right)\right)^2 - \frac{1}{3}\left(\frac{\partial u_i}{\partial x_i}\right)^2\right] \tag{3.3}$$

where μ is the dynamic viscosity. The rate of dissipation of mechanical energy is equivalent to an irreversible addition of heat to the fluid [51].

Blood is an incompressible fluid, meaning that $\frac{\partial u_i}{\partial x_i} = 0$. As a result, we can reduce viscous dissipation rate to

$$\phi_{3D,Cartesian} = \sum_i \sum_j \frac{\mu}{2\rho}\left(\frac{\partial u_i}{\partial x_j} + \frac{\partial u_j}{\partial x_i}\right)^2$$

We consider the viscous dissipation rate across the entire ventricle in polar coordinates:

$$\begin{aligned}\phi_{3D} = \int_V \mu\Bigg(2\left[\left(\frac{\partial u_r}{\partial r}\right)^2 + \left(\frac{1}{r}\frac{\partial u_\theta}{\partial \theta} + \frac{u_r}{r}\right)^2 + \left(\frac{\partial u_z}{\partial z}\right)^2\right] \\ + \left[r\frac{\partial}{\partial r}\left(\frac{u_\theta}{r}\right) + \frac{1}{r}\frac{\partial u_r}{\partial \theta}\right]^2 + \left[\frac{1}{r}\frac{\partial u_z}{\partial \theta} + \frac{\partial u_\theta}{\partial z}\right]^2 + \left[\frac{\partial u_r}{\partial z} + \frac{\partial u_z}{\partial r}\right]^2\Bigg) r d\theta dr dz.\end{aligned}$$

The 2D estimate of viscous dissipation rate is achieved by considering only a single r-θ plane and eliminating all terms with u_z or with derivatives with respect to z. As a result, viscous dissipation reduces to:

$$\phi_{2D} = \mu \int_A \left(2\left[\left(\frac{\partial u_r}{\partial r}\right)^2 + \left(\frac{1}{r}\frac{\partial u_\theta}{\partial \theta} + \frac{u_r}{r}\right)^2\right] + \left[r\frac{\partial}{\partial r}\left(\frac{u_\theta}{r}\right) + \frac{1}{r}\frac{\partial u_r}{\partial \theta}\right]^2\right) r d\theta dr.$$

This can be expanded and rewritten with each term labeled:

$$\begin{aligned}\phi_{2D} = \mu \int_A \Bigg(\underbrace{2\left(\frac{\partial u_r}{\partial r}\right)^2}_{\text{a}} + \underbrace{2\left(\frac{1}{r}\frac{\partial u_\theta}{\partial \theta}\right)^2}_{\text{b}} + \underbrace{4\left(\frac{1}{r}\frac{\partial u_\theta}{\partial \theta}\frac{u_r}{r}\right)}_{\text{c}} + \underbrace{2\left(\frac{u_r}{r}\right)^2}_{\text{d}} \\ + \underbrace{\left(r\frac{\partial}{\partial r}\left(\frac{u_\theta}{r}\right)\right)^2}_{\text{e}} + \underbrace{2\left(\frac{\partial}{\partial r}\left(\frac{u_\theta}{r}\right)\frac{\partial u_r}{\partial \theta}\right)}_{\text{f}} + \underbrace{\left(\frac{1}{r}\frac{\partial u_r}{\partial \theta}\right)^2}_{\text{g}}\Bigg) r d\theta dr.\end{aligned}$$

For the 1D estimate, we still consider data in a single r-θ plane, but where only the radial component of velocity is available. The u_θ component of velocity is neglected and viscous dissipation rate reduces to:

$$\phi_{1D} = \mu \int_A \left(\underbrace{2\left(\frac{\partial u_r}{\partial r}\right)^2}_{\text{a}} + \underbrace{2\left(\frac{u_r}{r}\right)^2}_{\text{d}} + \underbrace{\left(\frac{1}{r}\frac{\partial u_r}{\partial \theta}\right)^2}_{\text{g}}\right) r d\theta dr$$

where we keep terms a, d, and g.

Alternatively, we can also compare modified estimates where we assume that the planar-flow assumption is appropriate. To do this, we assume that the through-plane divergence is negligible and the 2D continuity equation holds, and then modify our viscous dissipation estimate accordingly. The 2D continuity equation can be written:

$$0 = \frac{1}{r}\frac{\partial u_\theta}{\partial \theta} + \frac{u_r}{r} + \frac{\partial u_r}{\partial r}$$

Therefore, we can rewrite our 2D estimate of viscous dissipation:

$$\begin{aligned}\phi_{2D,divergence-free} =& \mu \int_A \Bigg(2\Bigg[\underbrace{2\left(\frac{\partial u_r}{\partial r}\right)^2}_{\text{a}} \Bigg] + \underbrace{\left(r\frac{\partial}{\partial r}\left(\frac{u_\theta}{r}\right)\right)^2}_{\text{e}} \\ &+ \underbrace{2\left(\frac{\partial}{\partial r}\left(\frac{u_\theta}{r}\right)\frac{\partial u_r}{\partial \theta}\right)}_{\text{f}} + \underbrace{\left(\frac{1}{r}\frac{\partial u_r}{\partial \theta}\right)^2}_{\text{g}} \Bigg) r d\theta dr.\end{aligned}$$

Now, if the u_θ component of velocity is neglected, 1D viscous dissipation reduces to:

$$\phi_{1D,divergence-free} = \mu \int_A \Bigg(2\Bigg[\underbrace{2\left(\frac{\partial u_r}{\partial r}\right)^2}_{\text{a}} \Bigg] + \underbrace{\left(\frac{1}{r}\frac{\partial u_r}{\partial \theta}\right)^2}_{\text{g}} \Bigg) r d\theta dr$$

where we can see that we keep terms a and g.

3.2.3 Methods: Synthetic Vortices

In order to explore the efficacy of using 1D estimates of kinetic energy and viscous dissipation rate compared to 2D estimates, the metrics were first evaluated using synthetic flow fields with analytical solutions. Since the vortex formation in the left ventricle is tied to viscous dissipation and heart health, analytical solutions for four different types of vortex flows were chosen.

These synthetic vortices were placed and defined on a 2D grid, where the radius ranges from r_{min} to r_{max} and the angle ranges from θ_{min} to θ_{max}. Then, 2D and 1D estimates of kinetic energy and viscous dissipation rate were calculated. A variety of mesh resolutions, vortex center locations, and vortex strengths were tested for each type of vortex. For each type of vortex, 100 to 200 vortices were evaluated, and the vortex center location and strength were randomly generated for each vortex. In addition, multiple grid resolutions were tested, and $\frac{\mu}{\rho}$ was taken to be 1 for simplicity. In the following descriptions, the center of each vortex is defined at $x_c\mathbf{e_x} + y_c\mathbf{e_y} + z_c\mathbf{e_z} = r_c\mathbf{e_r} + \theta_c\mathbf{e}_\theta + z_c\mathbf{e_z}$.

Rigid-body Vortices

In a rigid-body vortex, angular rotational velocity, Ω, is uniform. The velocity field is

$$\begin{aligned}\mathbf{u} =& -\Omega(y-y_c)\mathbf{e_x} + \Omega(x-x_c)\mathbf{e_y} \\ =& \Omega r_c(\sin\theta_c\cos\theta - \cos\theta_c\sin\theta)\mathbf{e_r} + \Omega(r - r_c(\sin\theta_c\sin\theta + \cos\theta_c\cos\theta))\mathbf{e}_\theta.\end{aligned}$$

Irrotational Vortices

In an irrotational vortex, the velocity is inversely proportional to the center of the vortex:

$$\begin{aligned}\mathbf{u} =& -\alpha(y-y_c)((x-x_c)^2+(y-y_c)^2)^{-1}\mathbf{e_x} + \alpha(x-x_c)((x-x_c)^2+(y-y_c)^2)^{-1}\mathbf{e_y} \\ =& \frac{\alpha}{(r^2+r_c^2-2rr_c\cos(\theta_c-\theta))}\left(r_c\sin(\theta_c-\theta)\mathbf{e_r} + (r-r_c\cos(\theta_c-\theta))\mathbf{e}_\theta\right)\end{aligned}$$

where α determines the strength of the vortex.

Lamb-Oseen Vortex

The Lamb-Oseen vortex is a vortex that decays over time due to viscosity. It is an exact solution of the 2D Navier-Stokes equation and the radial component of velocity is zero when the center is at $r = 0$:

$$\begin{aligned}v_r =& 0 \\ v_\theta =& \frac{\gamma}{2\pi r}\left(1-\exp\left(-\frac{r^2}{c^2(t)}\right)\right)\end{aligned}$$

where

$$\begin{aligned}\gamma =& \text{ circulation contained in the vortex} \\ \nu =& \text{ viscosity} \\ c(t) =& \sqrt{4\nu t + c^2(0)} \\ c =& \text{ a parameter controlling the strength of the vortex.}\end{aligned}$$

When the center is at $r = r_c$, $\theta = \theta_c$,

$$\begin{aligned}v_r =& \frac{\gamma r_c\sin(\theta_c-\theta)}{2\pi(r^2+r_c^2-2rr_c\cos(\theta_c-\theta))}\left(1-\exp\left(-\frac{r^2+r_c^2-2rr_c\cos(\theta_c-\theta)}{c^2(t)}\right)\right) \\ v_\theta =& \frac{\gamma(r-r_c\cos(\theta_c-\theta))}{2\pi(r^2+r_c^2-2rr_c\cos(\theta_c-\theta))}\left(1-\exp\left(-\frac{r^2+r_c^2-2rr_c\cos(\theta_c-\theta)}{c^2(t)}\right)\right).\end{aligned}$$

Hill's Spherical Vortex

Hill's Spherical Vortex is a relatively simple analytical description of a vortex ring. In 3D, the velocity field within a Hill's Spherical Vortex centered at $(0, 0, 0)$ with radius c is:

$$\begin{aligned} v_r =& \frac{3U}{2c^2} rz \\ v_\theta =& 0 \\ v_z =& \frac{3U}{2c^2}(c^2 - 2r^2 - z^2). \end{aligned}$$

The velocity field outside of the vortex centered at $(0, 0, 0)$ with radius c is:

$$\begin{aligned} v_r =& \frac{3c^3U}{2} \frac{rz}{(r^2 + z^2)^{5/2}} \\ v_\theta =& 0 \\ v_z =& -U - \frac{c^3U}{2} \frac{(r^2 - 2z^2)}{(r^2 + z^2)^{5/2}}. \end{aligned}$$

For the purposes of a 2D examination of a vortex, we will look at the vortex in the $x - z$ plane, where $y = 0$. Therefore, the out-of-plane velocity goes to 0 and we are concerned with the in-plane cartesian components v_x and v_z. In addition, we consider a vortex centered at $(x_c, 0, z_c)$. See appendix B for more details.

Inside the vortex, we get

$$\begin{aligned} v_x =& \frac{3U}{2c^2}(x - x_c)(z - z_c) \\ v_y =& 0 \\ v_z =& \frac{3U}{2c^2}(c^2 - 2(x - x_c)^2 - (z - z_c)^2). \end{aligned}$$

Outside of the vortex, the velocity is

$$\begin{aligned} v_x =& \frac{3c^3U}{2} \frac{(x - x_c)(z - z_c)}{((x - x_c)^2 + (z - z_c)^2)^{5/2}} \\ v_y =& 0 \\ v_z =& -U - \frac{c^3U}{2} \frac{((x - x_c)^2 - 2(z - z_c)^2)}{((x - x_c)^2 + (z - z_c)^2)^{5/2}}. \end{aligned}$$

For simplicity, the analytical versions of radial and azimuthal components of velocity will not be presented in this dissertation.

3.2.4 Methods: Left Ventricle Data

To gain a better understanding of how these estimates would perform clinically, the estimates were tested on the results of multiple computational fluid dynamics simulations of flow in the left ventricle.

Results from a computational fluid dynamics simulation provide all three components of velocity in a 3D domain. The true, 3D calculations of kinetic energy and viscous dissipation rate were calculated in the entire ventricle, and compared to the reduced order estimates. In order to evaluate the reduced order estimates, a single plane was extracted to represent the type of data that would be collected in a color-Doppler ultrasound acquisition. Then, the kinetic energy and viscous dissipation rate were calculated using the two, known, in-plane components of velocity, called the '2D' estimates. Then, the kinetic energy and viscous dissipation rate were calculated where the radial component of velocity is known and the azimuthal component of velocity was calculated from the radial component using the reconstruction method developed by Garcia et al. [24]. This estimate is called the '2D reconstructed' estimate. Then, the 1D estimates were evaluated using only the radial component of velocity, called the '1D' estimate.

In addition, variations in transducer location were also considered. In reality, the transducer will not be placed in the exact same location for each patient, so it is important to study the effects of transducer location on estimates of kinetic energy and viscous dissipation rate. Figure 3.16a shows some of the transducer locations for one of the data sets used in this study. In this figure, all measurements and calculations are made from the same plane, but a different transducer location will result in different radial and azimuthal components of velocity at each point. In addition to multiple transducer locations in the same plane, multiple planes were also tested.

The CFD simulations were performed by Jonas Lantz and Tino Ebbers at Linköping University. The simulations are a result of a fluid dynamics simulation where the geometry of the heart was collected from Computed Tomography images.

3.3 Results: Kinetic Energy in Synthetic Vortices

The results of 1D and 2D estimates of kinetic energy for different types of synthetic vortices are presented in this section. Numerical solutions are presented for all types of vortices, and they are preceded by analytical solutions in some cases. Step-by-step analytical results are presented in Appendix B.

For all types of vortices, we expect the 1D estimate of kinetic energy to be less than the 2D estimate because we are missing a positively valued term (i.e. v_θ^2). We are interested in whether or not the 1D and 2D estimates are correlated with each other. To examine this, we focus on the coefficient of determination, or R^2, as a measure of the correlation between two variables, x and y. The coefficient of determination is equal to the proportion of the variance in y that is explained by a linear relationship with x.

3.3.1 Rigid-body Vortices

Kinetic energy can be evaluated analytically. In $2D$ we get

$$KE_{2D} = \frac{1}{2}\Omega^2 \int_A \Big((\sin\theta_c \cos\theta - \cos\theta_c \sin\theta)^2 + (r - r_c(\sin\theta_c \sin\theta + \cos\theta_c \cos\theta))^2\Big) r d\theta dr.$$

In $1D$ we get

$$KE_{1D} = \frac{1}{2}\Omega^2 \int_A (\sin\theta_c \cos\theta - \cos\theta_c \sin\theta)^2 r d\theta dr.$$

The 1D estimate of kinetic energy is different by the term $\frac{1}{2}\Omega^2(r - r_c(\sin\theta_c \sin\theta + \cos\theta_c \cos\theta))^2$. Close to the center of the vortex, this term goes to 0, and then it increases in magnitude further away from the center. Since this term is integrated across the whole area we expect the contribution of this term to be related to the strength (Ω) of the vortex. However, the term that is contained in the 1D approximation is also multiplied by Ω^2 and so we would expect the 1D estimate to be correlated with the 2D kinetic energy.

On both a fine and a coarse grid we see that the 1D estimate of kinetic energy appears to be correlated with the 2D kinetic energy (Figure 3.2), with an R^2 value of 0.83 and 0.85 respectively. This high level of linear correlation is expected based on our analytical findings. However, we do see that there are a few cases where the 1D estimate of kinetic energy is much lower than expected based on the linear correlation of the other points.

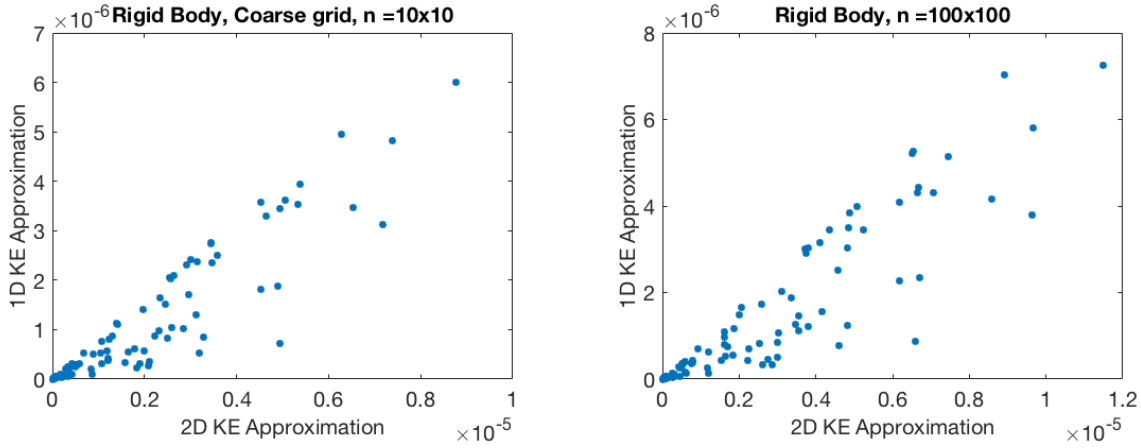

(a) **(b)**

Figure 3.2: 1D estimate of kinetic energy (KE) versus 2D kinetic energy in a single plane for rigid-body vortices on a coarse (a) and fine (b) grid.

		R^2 with 2D KE		R^2 with 2D VDR		
Vortex Type	Grid Size	1D KE	2D VDR	1D VDR	1D divergence -free VDR	b
Rigid-Body	100 x 100	0.83	0.53	0.94	0.99	0.78
	10 x 10	0.85	0.46	0.92	0.99	0.67
Irrotational	100 x 100	0.81	0.71	0.82	0.81	0.88
	10 x 10	0.68	0.95	0.68	0.61	0.96
Lamb-Oseen	100 x 100	0.97	0.32	0.99	0.99	0.95
	10 x 10	0.92	0.83	0.89	0.90	0.87
Hill's Spherical	100 x 100	0.99	0.83	0.94	0.94	0.93
	10 x 10	0.99	0.50	0.96	0.96	0.76

Table 3.1: R^2 between estimates of the 2D values of kinetic energy (KE) and viscous dissipation rate (VDR) and the 1D reduced order estimates of kinetic energy and viscous dissipation rate.

3.3.2 Irrotational Vortices

Kinetic energy can be evaluated analytically. In $2D$ we get

$$KE_{2D} = \frac{\alpha^2}{2} \int_A \frac{1}{(r^2 + r_c^2 - 2rr_c\cos(\theta_c - \theta))} r d\theta dr.$$

In $1D$,

$$KE_{1D} = \frac{\alpha^2}{2} \int_A \frac{r_c^2 \sin^2(\theta_c - \theta)}{(r^2 + r_c^2 - 2rr_c\cos(\theta_c - \theta))^2} r d\theta dr.$$

The 1D and 2D calculations of kinetic energy are different by a factor of $r_c^2 \sin^2(\theta_c - \theta)$. This factor will vary with the location of the center of the vortex with respect to the origin, which will influence the correlation between 1D and 2D estimates of kinetic energy. However, if the strength of the vortex, α, is sufficiently strong, then we would still expect to see a relationship between the 1D and 2D estimates of kinetic energy. Based on our numerical results, it appears that the 1D and 2D estimates of kinetic energy are correlated (Figure 3.3b), with an R^2 value of 0.81 for the fine grid. For the coarse grid, the coefficient of determination drops to 0.68 (Figure 3.3a). This indicates that estimates of kinetic energy in the irrotational vortex are not robust to grid resolution.

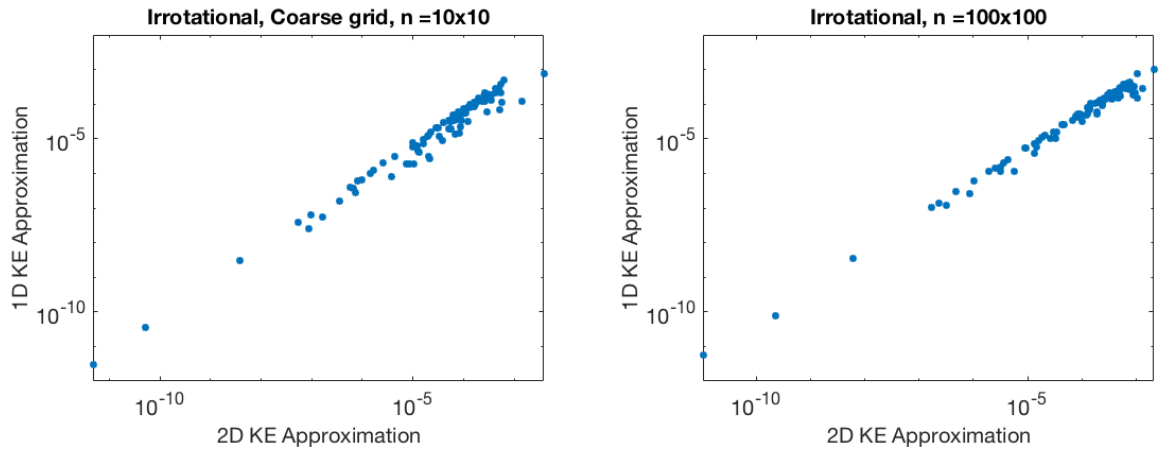

(a) **(b)**

Figure 3.3: 1D estimate of kinetic energy versus 2D kinetic energy in a single plane for irrotational vortices on a coarse (a) and fine (b) grid plotted on a log-log scale.

3.3.3 Lamb-Oseen Vortex

In $2D$, kinetic energy is equal to

$$KE_{2D} = \frac{\gamma^2}{8\pi^2}\int_A \frac{\left(r_c^2 + r^2 - 2rr_c\cos(\theta_c - \theta)\right)}{(r^2 + r_c^2 - 2rr_c\cos(\theta_c - \theta))^2}\left(1 - \exp\left(-\frac{r^2 + r_c^2 - 2rr_c\cos(\theta_c - \theta)}{c^2(t)}\right)\right)^2 r d\theta dr.$$

In $1D$,

$$KE_{1D} = \frac{\gamma^2}{8\pi^2}\int_A \frac{\left(r_c^2\sin^2(\theta_c - \theta)\right)}{(r^2 + r_c^2 - 2rr_c\cos(\theta_c - \theta))^2}\left(1 - \exp\left(-\frac{r^2 + r_c^2 - 2rr_c\cos(\theta_c - \theta)}{c^2(t)}\right)\right)^2 r d\theta dr.$$

Similar to the other vortices, the difference between the 1D and 2D estimates of kinetic energy is a factor influenced by the location of the center of the vortex. We expect that like the other vortices, the correlations between the estimates is influenced by the location of the vortex, but that overall we will see a strong correlation between the 1D and 2D measures. We see these results in Figure 3.4 and with strong coefficients of determination of 0.97 and 0.92 for the fine and coarse grids respectively.

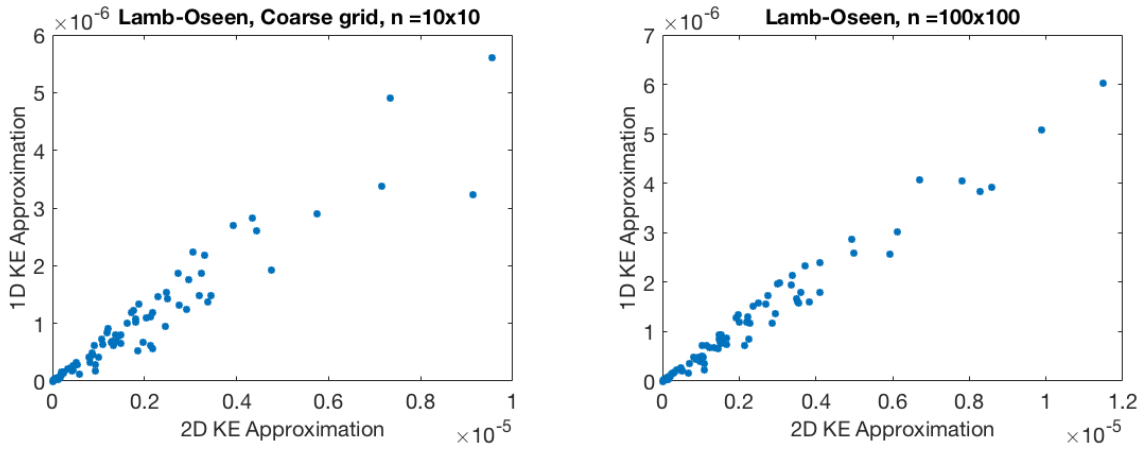

(a) **(b)**

Figure 3.4: 1D estimate of kinetic energy versus 2D kinetic energy in a single plane for Lamb-Oseen vortices on a coarse (a) and fine (b) grid plotted on a log-log scale.

3.3.4 Hill's Spherical Vortex

The kinetic energy for Hill's Spherical vortex can also be evaluated analytically, but it is not explored in this dissertation due to its complexity. However, we expect the general behavior to be the similar to the other vortices. In fact, we see that the estimates for Hill's Spherical Vortex have a very high R^2 of 0.99 between the 1D and 2D estimates of kinetic energy for both the coarse and fine grids (Figure 3.5).

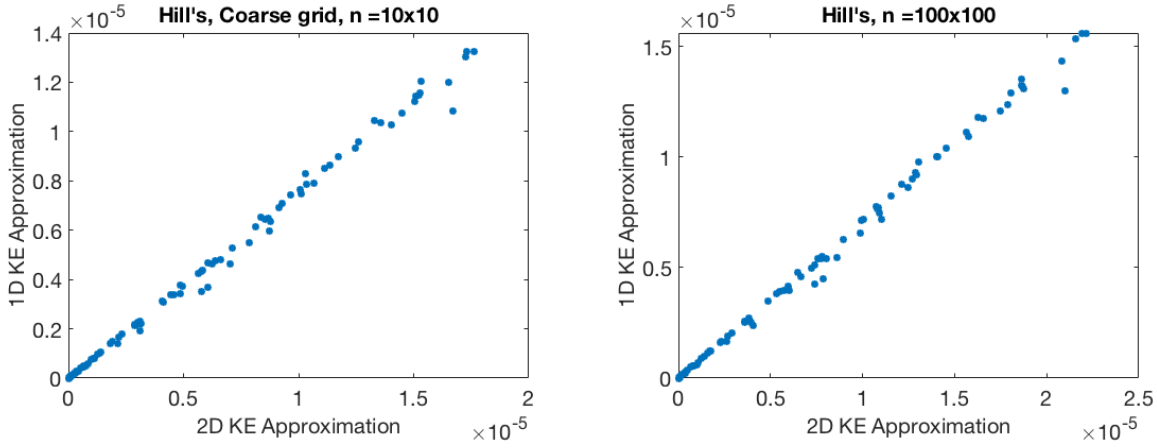

(a) **(b)**

Figure 3.5: 1D estimate of kinetic energy versus 2D kinetic energy in a single plane for Hill's Spherical Vortices on a coarse (a) and fine (b) grid.

3.4 Results: Viscous Dissipation Rate in Synthetic Vortices

The estimates of viscous dissipation rate for different types of synthetic vortices are presented in this section. Numerical solutions are presented for all types of vortices, and they are preceded by analytical solutions in some cases. Step-by-step analytical results are presented in Appendix B.

3.4.1 Rigid-body Vortices

The viscous dissipation rate can be evaluated analytically. In $2D$ we get:

$$\phi_{2D} = 0.$$

However in $1D$, the viscous dissipation rate estimate yields a nonzero value:

$$\phi_{1D} = \frac{\mu}{\rho} \int_A \left(\frac{\Omega r_c}{r} \right)^2 \left(1 + \sin^2 \theta_c \cos^2 \theta + \cos^2 \theta_c \sin^2 \theta \right) r d\theta dr.$$

The true viscous dissipation rate from a rigid-body vortex is equal to zero. Since the rigid-body vortex is not a function of z, the calculated 2D viscous dissipation rates should also be zero. However, the 1D estimate of viscous dissipation rate produces a positive result. Yet, when we calculated the 2D and 1D estimates, both gave nonzero results due to the numerical nature of the problem. The order of magnitude of the 1D results was much larger than the 2D results, and the order of magnitude for the 2D estimate decreased with increasing density of the grid. The results for 1D estimates are correlated with the 2D estimate (Figure 3.6), as they are heavily influenced by strength (Ω) and location in relation to the transducer (Figure 3.7).

In Figure 3.8 we examine the contributions to each term in the viscous dissipation rate. Many of the individual components appear to be correlated with the calculated 2D viscous dissipation rate. There also appears to be more scatter in d than g or a, which explains why for the rigid vortex, the 1D divergence-free estimate has a stronger correlation with the 2D measure than the 1D estimate has with the 2D measure.

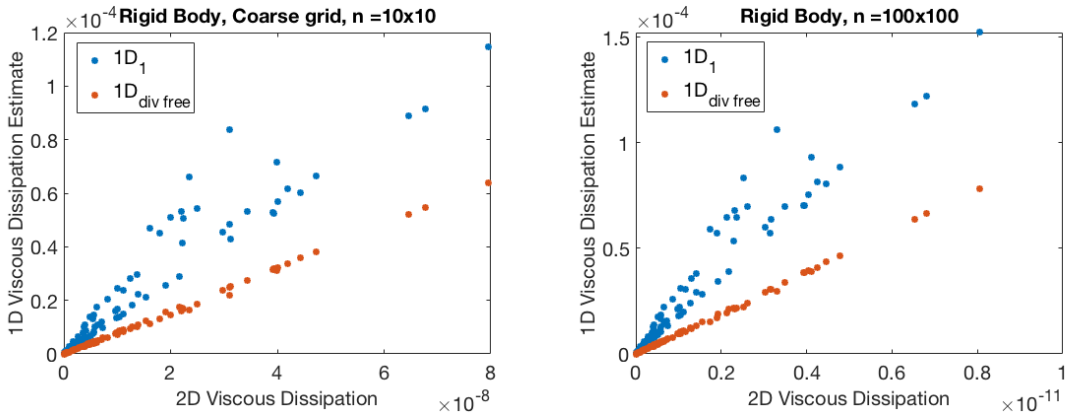

Figure 3.6: 1D viscous dissipation rate estimates versus 2D viscous dissipation rate for the rigid body vortex for a variety of different vortex locations on a coarse grid (left) and a fine grid (right). Each red-blue pair of points represents a different velocity field that contains a single vortex.

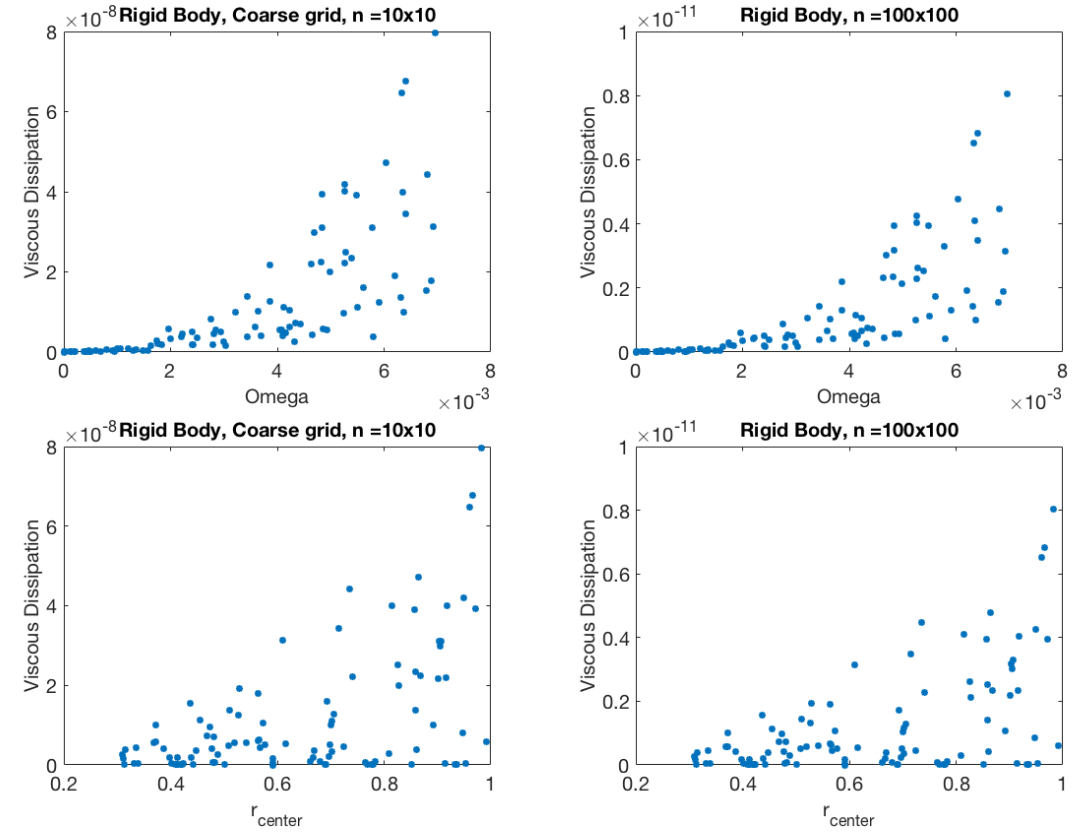

Figure 3.7: For the rigid body vortex, viscous dissipation rate estimates versus vortex strength (Omega) and vortex center (r_{center}) for different grid sizes.

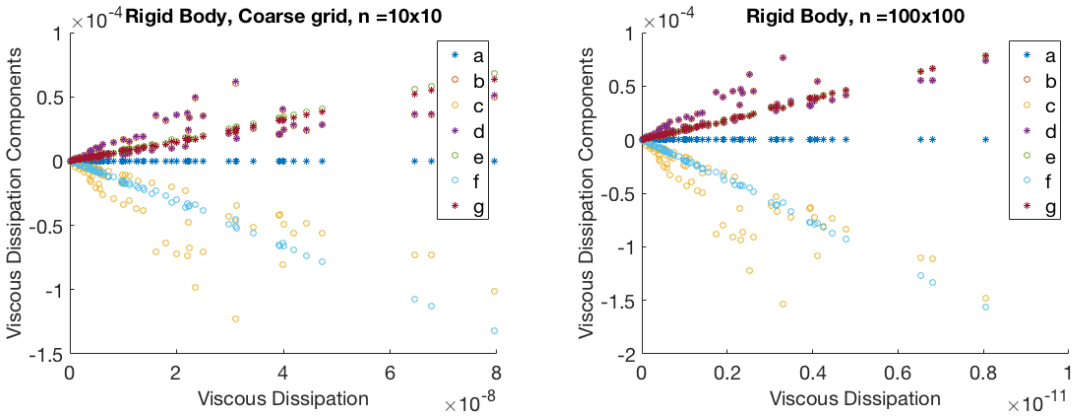

Figure 3.8: Components of viscous dissipation rate for the rigid body vortex for a variety of different vortex locations and grid sizes.

3.4.2 Irrotational Vortices

The viscous dissipation rate can be evaluated analytically. In $2D$ we get:

$$\phi_{2D} = \int_A \frac{8\alpha^2}{(r^2 + r_c^2 - 2rr_c\cos(\theta_c - \theta))^2} r d\theta dr.$$

But in $1D$:

$$\phi_{1D} = \int_A \frac{16r^2\sin^2(\theta_c - \theta)(r - r_c\cos(\theta_c - \theta))^2}{(r^2 + r_c^2 - 2rr_c\cos(\theta_c - \theta))^4} + \frac{4\Big(-r^2 - r_c^2 + 2rr_c\cos(\theta_c - \theta) + 2r_c^2\sin^2(\theta_c - \theta)\Big)^2}{(r^2 + r_c^2 - 2rr_c\cos(\theta_c - \theta))^4} r d\theta dr.$$

For irrotational vortices, there is a correlation between the 2D and 1D estimates of viscous dissipation rate, with an R^2 of 0.82 for the fine grid and 0.68 for the coarse grid (Figure 3.9). While there are a few outliers, the correlation becomes especially clear in the log-log plot due to how the results are distributed (Figure 3.10). Similar to the kinetic energy, reduced order estimates of viscous dissipation rate were not robust to resolution for the irrotational vortex. In addition, it is expected that the 1D estimate that takes into account the 2D divergence-free assumption would give a similar result, which is seen with an R^2 of 0.81 for the fine grid and 0.61 for the coarse grid. The 2D measure of viscous dissipation rate also is correlated to the vortex strength, as indicated by the analytical solution, but not by the vortex location (Figure 3.11).

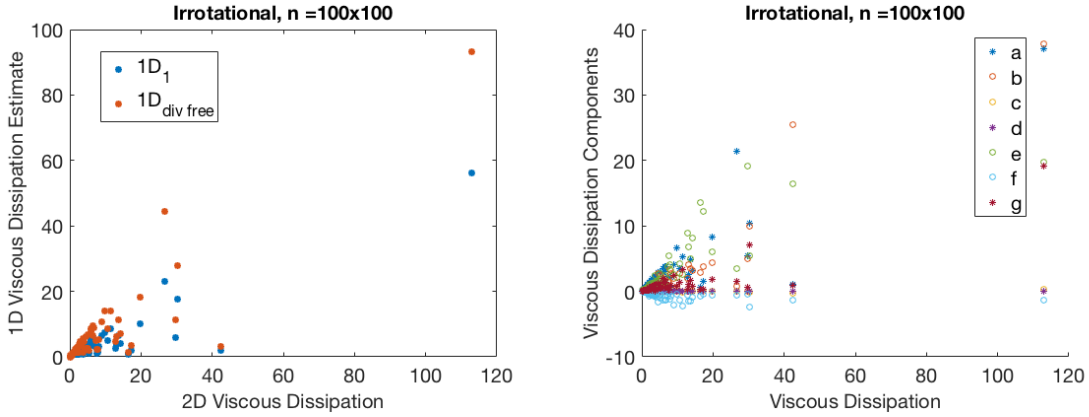

Figure 3.9: 1D viscous dissipation rate estimates (left) and components of viscous dissipation rate (right) versus 2D viscous dissipation rate for the irrotational vortex for a variety of different vortex locations.

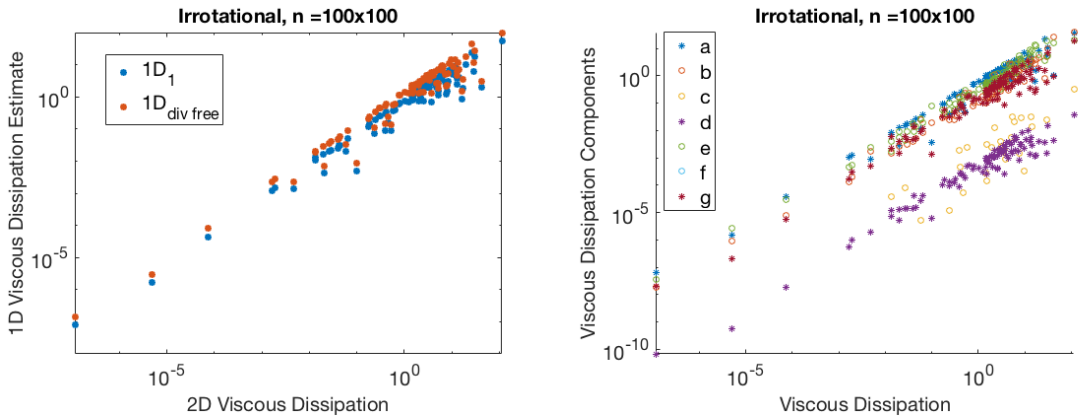

Figure 3.10: 1D viscous dissipation rate estimates (left) and components of viscous dissipation rate (right) versus 2D viscous dissipation rate for the irrotational vortex for a variety of different vortex locations plotted on a log-log scale. Each red-blue pair of points represents a different velocity field that contains a single vortex.

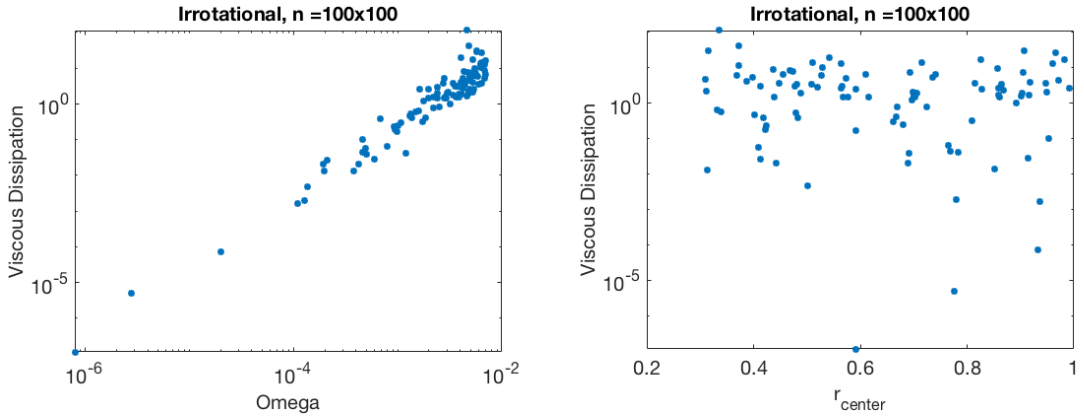

Figure 3.11: 2D viscous dissipation rate versus attributes of the vortex. On the left is 2D viscous dissipation rate versus vortex strength and on the right is 2D viscous dissipation rate versus vortex center.

3.4.3 Lamb-Oseen Vortex

The viscous dissipation rate for Lamb-Oseen vortices can also be evaluated analytically, but that is not explored in this paper. Overall, there was a strong correlation for both the 1D and 1D divergence-free estimates of viscous dissipation with the 2D estimates of viscous dissipation (Figure 3.12). For the fine grid, there was an R^2 of 0.99 for both the 1D and 1D divergence-free estimates, and for the coarse grid these coefficients reduced to 0.89 and 0.90 respectively.

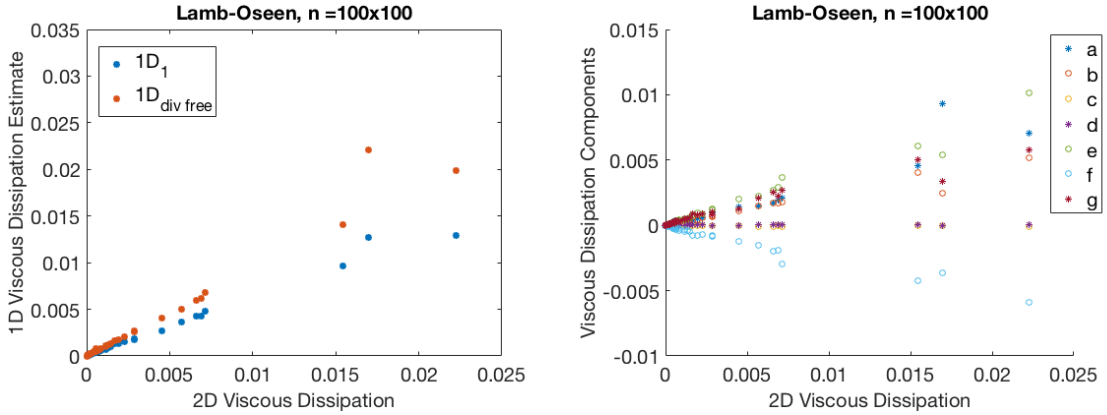

Figure 3.12: 1D viscous dissipation rate estimates (left) and components of viscous dissipation rate (right) versus 2D viscous dissipation rate for the Lamb-Oseen vortex for a variety of different vortex locations and strengths on a fine grid.

3.4.4 Hill's Spherical Vortex

The viscous dissipation rate for Hill's Spherical vortices can also be evaluated analytically, but it is not explored in this paper. Like all the vortices explored in this section, there is a strong correlation between the 2D estimate of viscous dissipation and both the 1D and 1D divergence-free estimates (Figure 3.13). The R^2 between both the 1D and 1D divergence-free estimate with the 2D calculation was 0.94 for the fine grid and 0.96 for the coarse grid.

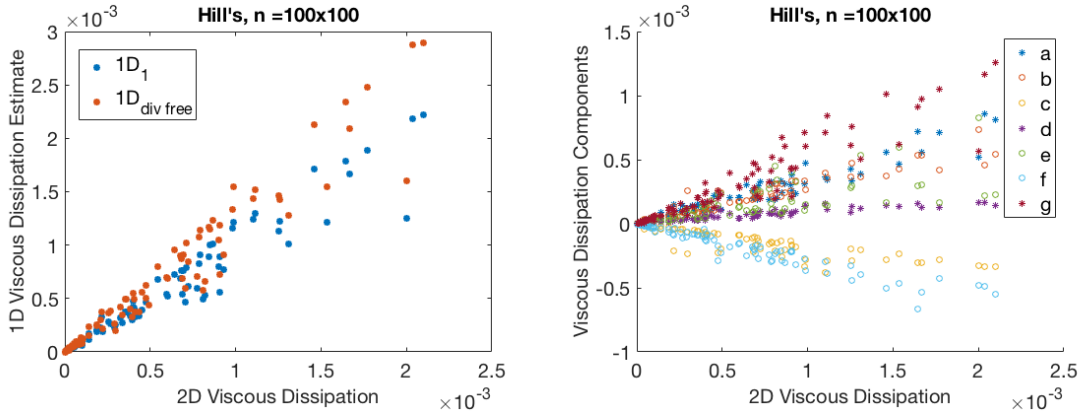

Figure 3.13: 1D viscous dissipation rate estimates (left) and components of viscous dissipation rate (right) versus 2D viscous dissipation rate for the Hill's Spherical vortex for a variety of different vortex locations and strengths.

3.5 Results: Kinetic Energy in Left Ventricle Data

The kinetic energy was evaluated in 3 different patients. For each patient, multiple time points and multiple transducer locations were tested. Overall, the results showed that reduced order estimates of kinetic energy were positively correlated with true, 3D kinetic energy (Figure 3.14). Figure 3.15 shows the R^2 values between all of the estimates and both true, 3D kinetic energy and true, 3D viscous dissipation rate. For kinetic energy, the coefficient of determination was above 0.80 for all reduced estimates. With color-Doppler ultrasound, the exact azimuthal component of velocity will not be known. Therefore, instead of using the 2D estimate, it is of greater clinical use to examine the coefficient of determination for the 2D reconstructed and 1D estimates, which are about equal to each other. This indicates that the 1D estimate would be just as valuable clinically as the 2D reconstructed estimate. The 2D reconstructed estimate is much more difficult to calculate, so if the 1D estimate is just as informative, there is no need to calculate the 2D reconstructed estimate.

The true value of 3D kinetic energy is also positively correlated with 3D viscous dissipation rate ($R^2 \approx 0.80$). This makes physical sense, as viscous dissipation rate is the sum of velocity gradients, so higher values of viscous dissipation rate occur when there is a spatial transition between high to low velocity magnitude (Figure 3.1). High values of kinetic energy occur when there are high velocity magnitudes. In the left ventricle, the no-slip velocity condition at the walls require that there are always regions of low velocity magnitude, even when there are also regions of high velocity magnitudes. This means that when there are high velocity magnitudes (i.e. high kinetic energy), there are also regions of low velocity magnitude and therefore there will be large spatial transitions between high and low velocity magnitudes (i.e. high viscous dissipation rate).

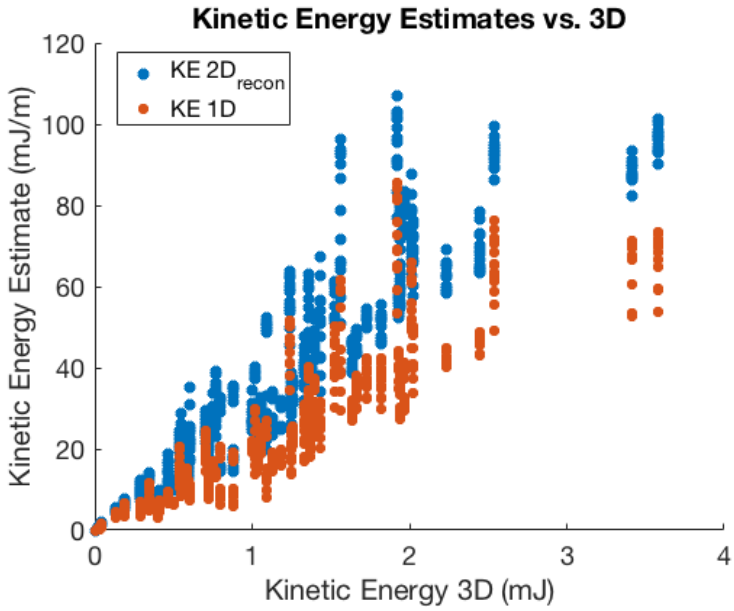

Figure 3.14: Comparison of the reduced order estimates of kinetic energy when only the radial component of velocity is measured to the true 3D measured kinetic energy for the left ventricle data.

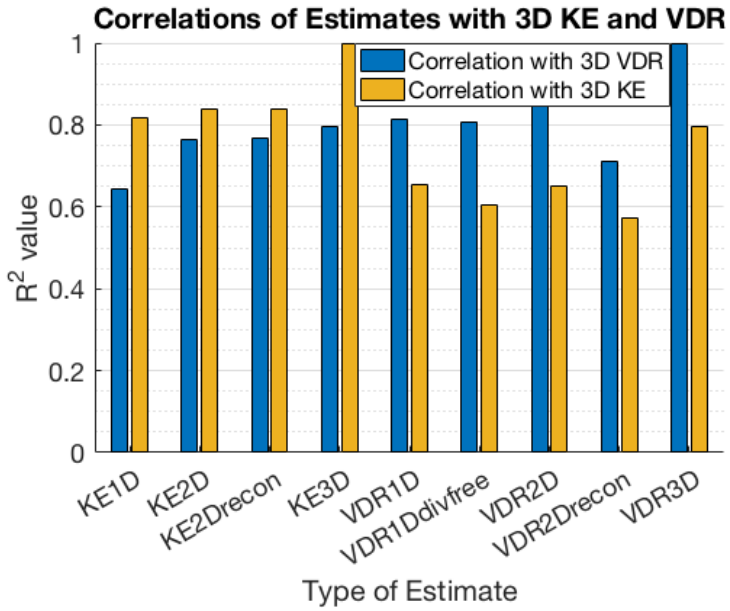

Figure 3.15: The R^2 value for the relationships between either the true kinetic energy (KE, yellow) or viscous dissipation rate (VDR, blue) and the reduced order estimates of kinetic energy and viscous dissipation rates for all of the data sets. See Table 3.2 for label descriptions.

3D KE, KE3D	true, 3D kinetic energy measured in the entire ventricle
3D VDR, VDR3D	true, 3D viscous dissipation rate measured in the entire ventricle
KE1D	1D estimate of kinetic energy, calculated using only the radial component of velocity on a single plane
KE2D	2D estimate of kinetic energy, calculated using the available radial and azimuthal components of velocity on a single plane
KE2Drecon	2D estimate of kinetic energy, calculated using the available radial component of velocity and the azimuthal component of velocity that is calculated from the radial component, on a single plane
VDR1D	1D estimate of viscous dissipation rate, calculated using only the radial component of velocity on a single plane
VDR1Ddivfree	1D estimate of viscous dissipation rate, calculated using only the radial component of velocity and assuming that the through-plane divergence is negligible, on a single plane
VDR2D	2D estimate of viscous dissipation rate, calculated using the available radial and azimuthal components of velocity on a single plane
VDR2Drecon	2D estimate of viscous dissipation rate, calculated using the available radial component of velocity and the azimuthal component of velocity that is calculated from the radial component, on a single plane

Table 3.2: Descriptions of labels used in bar charts for coefficients of determination between 3D kinetic energy and viscous dissipation and reduced order estimates of kinetic energy and viscous dissipation.

In Figure 3.16, we examine the different reduced order estimates for a single heart at multiple time points at varying transducer locations, shown in Figure 3.16a. The strong correlation between the true 3D kinetic energy and the 2D estimate is maintained in this heart (Figure 3.16b). This 2D estimate is not strongly influenced by transducer location, which is expected because for different transducer locations, the only difference between the 2D estimates is that the grid resolution changes in different areas of the heart. The correlations between the true 3D kinetic energy and the 2D reconstructed estimate and between the true 3D kinetic energy and the 1D estimate are also maintained (Figures 3.16c and 3.16d, respectively). When the transducer was located closer to the intraventricular septum, i.e. shifts 2 and 5, the 1D estimates for kinetic energy were lower than when the transducer was located at other locations. Shifts 1 and 4, toward the mitral valve, consistently produced higher estimates than the other transducer locations. These changes in 1D kinetic energy estimates with transducer location were consistent across the hearts examined in this study.

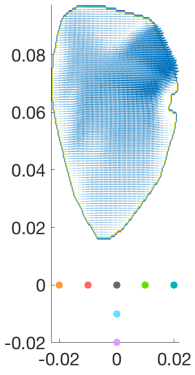

(a) Transducer locations for one heart.

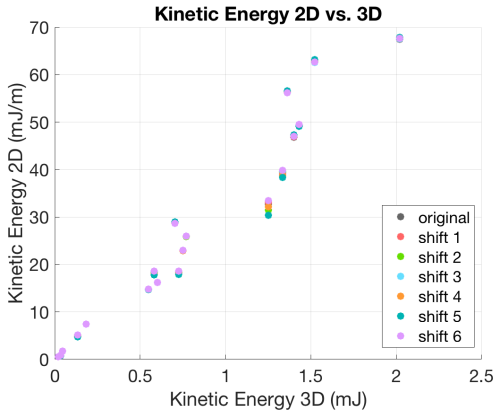

(b) Comparison of the 2D estimate of kinetic energy when both radial and azimuthal components of velocity are known to the true 3D measured kinetic energy for one heart.

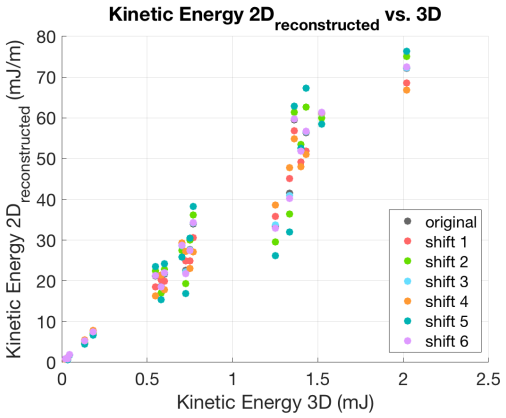

(c) Comparison of 2D reconstructed estimate of kinetic energy when the radial component of velocity is known and the azimuthal component is calculated from the radial component, to the true 3D measured kinetic energy for one heart.

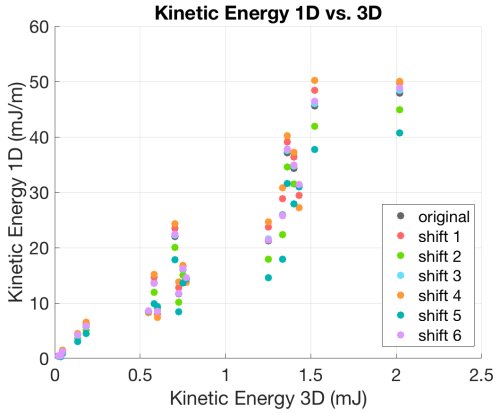

(d) Comparison of the 1D estimate of kinetic energy when both radial and azimuthal components of velocity are known to the true 3D measured kinetic energy for one heart.

Figure 3.16: Comparison of the reduced order estimates for kinetic energy for varying transducer locations for a single heart on a single plane. Measurements were taken at multiple time points throughout the cardiac cycle. The colors correspond to specific transducer locations.

Left Ventricle Data: Added Noise

When noise was added to the data, the coefficient of determination remained above 0.80 between the true 3D kinetic energy and all reduced order estimates of kinetic energy (Figure 3.17). Color-Doppler ultrasound data is noisy, and these results indicate that estimates of

kinetic energy are robust to noise.

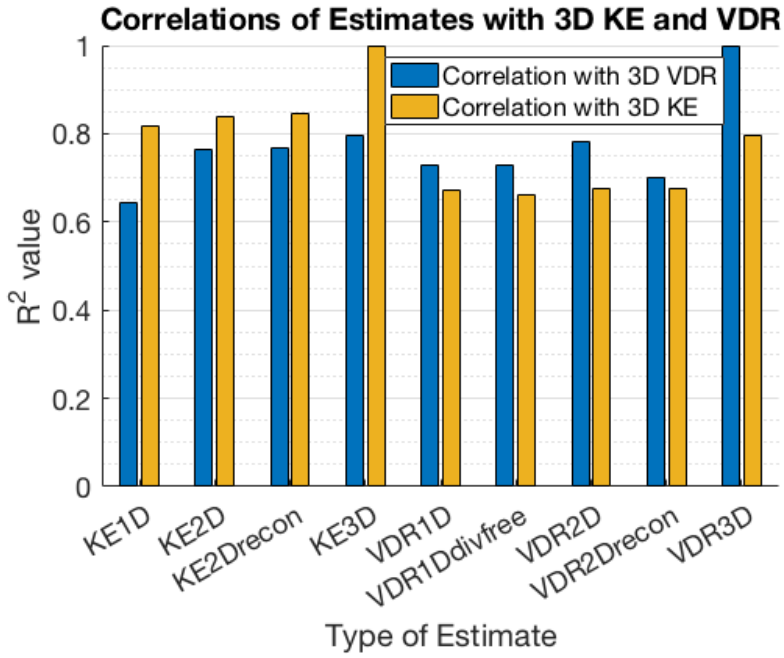

Figure 3.17: The R^2 values for the relationships between either the true kinetic energy (KE - yellow) or viscous dissipation rates (VDR - blue) and the reduced order estimates of kinetic energy and viscous dissipation rate for all of the left ventricle data sets with artificial noise added. See Table 3.2 for label descriptions.

Left Ventricle Data: Lower Resolution

At the lower resolution, the coefficients of determination between the true 3D kinetic energy and reduced order estimates dropped by about 10-15% (Figure 3.18) compared to the higher resolution data (Figure 3.15).

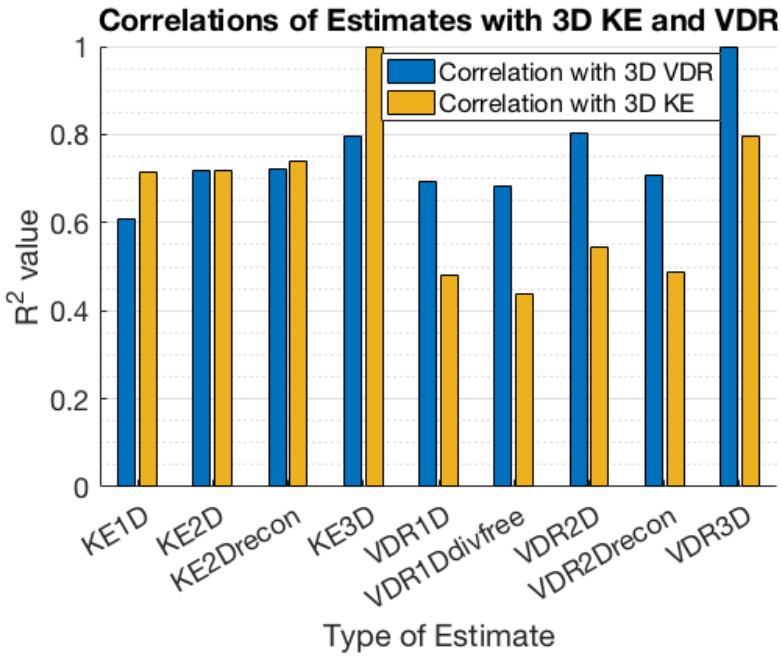

Figure 3.18: The R^2 values for the relationships between either the true kinetic energy (KE - yellow) or viscous dissipation rate (VDR - blue) and the reduced order estimates of kinetic energy and viscous dissipation rate for all of the left ventricle data sets at a reduced resolution. See Table 3.2 for label descriptions.

3.6 Results: Viscous Dissipation Rate in Left Ventricle Data

The reduced order estimates of viscous dissipation rates were positively correlated with the true, 3D viscous dissipation rate (Figure 3.19). The strongest correlation, with an R^2 of about 0.85 was the 2D estimate. However, current measurements from color-Doppler ultrasound data do not allow for this type of measurement so we are more interested in the 2D reconstructed, 1D, and 1D divergence-free estimates. Both the 1D and 1D divergence-free estimates had R^2 values of just above 0.80. The 2D reconstructed estimate had an R^2 of about 0.70. The higher R^2 values for the 1D estimates indicate that if we are trying to acquire viscous dissipation rate information from ultrasound data, it is better to calculate an estimate directly from only the radial component of velocity, rather than calculating the azimuthal component in order to calculate the 2D reconstructed estimate.

Interestingly, the true, 3D viscous dissipation rate was strongly correlated with the 2D and 2D reconstructed measures of kinetic energy, with higher coefficients of determination than for the 2D reconstructed viscous dissipation rate. As mentioned previously, it makes sense that viscous dissipation rate is correlated with kinetic energy, but it is not expected for some estimates of kinetic energy to be more strongly correlated with viscous dissipation

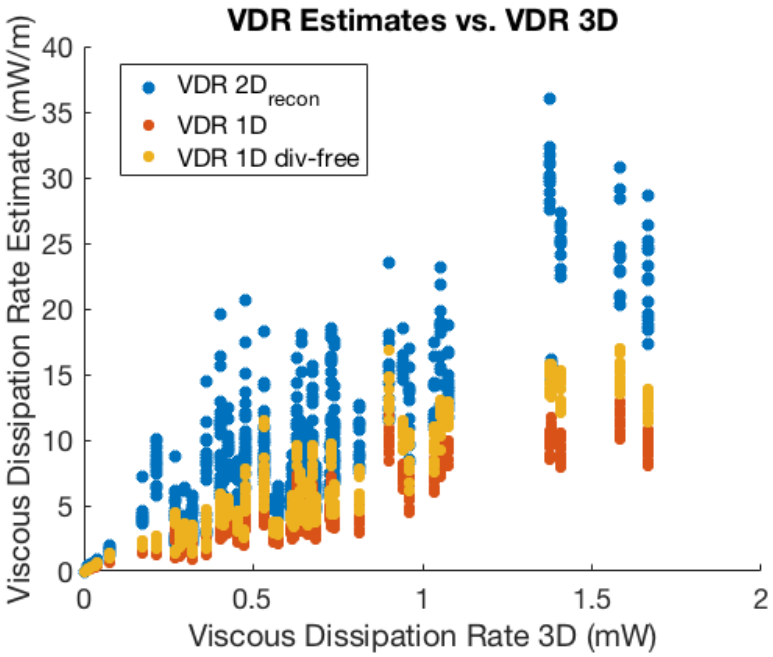

Figure 3.19: Comparison of the reduced order estimates of viscous dissipation rate (VDR) to the true 3D measured viscous dissipation rate for the Linköping University data. See Table 3.2 for label descriptions.

rate than estimates of viscous dissipation rate. However, all of our estimates only consider estimates in a single plane and because viscous dissipation rate is more complicated to calculate than kinetic energy, we see that some of the measures of kinetic energy are more robust to the reduced order estimations than viscous dissipation rate.

Figure 3.20 compares the reduced order estimates for viscous dissipation rate to the true 3D viscous dissipation rate for a single heart, for multiple different time points and multiple different transducer locations (Figure 3.16a). Similar to the kinetic energy results, there is a strong correlation between the 3D viscous dissipation and the true 2D estimates, and the 2D is not strongly influenced by transducer location (Figure 3.20a). The strong correlation indicates that the viscous dissipation in the long-axis apical plane is strongly correlated with the overall viscous dissipation at each point throughout the cycle. Figure 3.20b demonstrates that while there is a positive correlation between the 3D and 2D estimate of viscous dissipation when the second component of velocity is calculated from the first component, it is not as strong of a correlation as the other estimates. For viscous dissipation, we see that shifts 1 and 4, towards the mitral valve, provide larger scatter in the estimates than the other transducer locations. The results for the 1D and the 1D divergence-free estimates (Figures 3.20c and 3.20d respectively) both show very similar, strong correlations between the 1D estimates and 3D values for viscous dissipation rate.

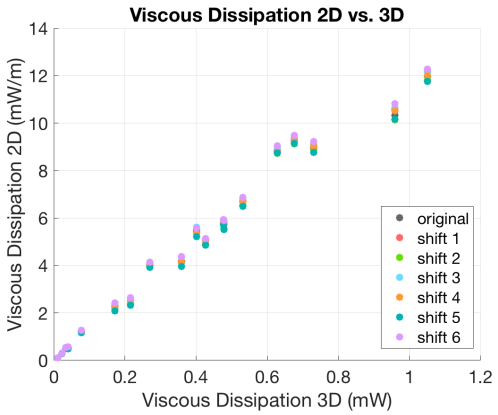

(a) Comparison of the 2D estimate of viscous dissipation rate when both radial and azimuthal components of velocity are known to the true 3D measured viscous dissipation rate.

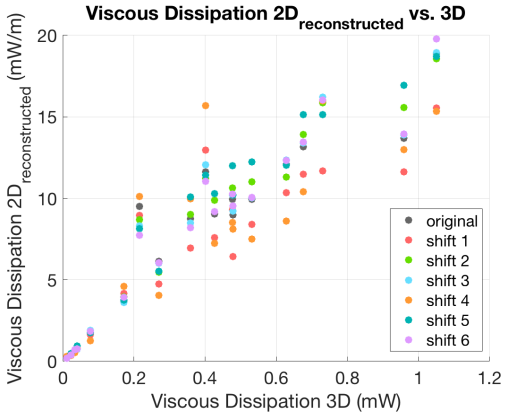

(b) Comparison of 2D reconstructed estimate of viscous dissipation rate when the radial component of velocity is known and the azimuthal component is calculated from the radial component, to the true 3D measured viscous dissipation rate.

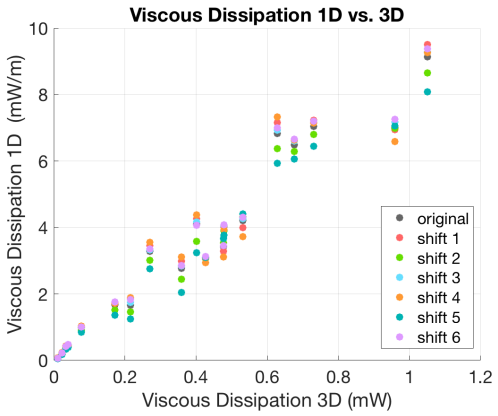

(c) Comparison of the 1D estimate of viscous dissipation rate when both radial and azimuthal components of velocity are known to the true 3D measured viscous dissipation rate.

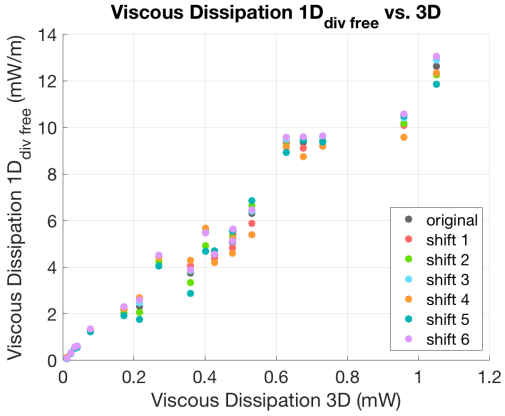

(d) Comparison of the 1D divergence-free estimate of viscous dissipation rate when both radial and azimuthal components of velocity are known to the true 3D measured viscous dissipation rate.

Figure 3.20: Comparison of the reduced order estimates for viscous dissipation rate for varying transducer locations for a single left ventricle on a single plane. Measurements were taken at multiple time points throughout the cardiac cycle. The colors correspond to specific transducer locations.

Left Ventricle Data: Added Noise

When artificial noise is added to the data, the R^2 values between the true, 3D value of viscous dissipation rate and the reduced order estimates of viscous dissipation rate are around 0.70

(Figure 3.17). However, the coefficients of determination between the true, 3D value of viscous dissipation rate and the 2D reconstructed and 2D estimates of kinetic energy are around 0.70 as well. This suggests that reduced order estimates of kinetic energy have the potential be helpful in evaluating viscous dissipation rate from color-Doppler ultrasound data.

Left Ventricle Data: Lower Resolution

At a reduced resolution, the coefficients of determination between reduced order estimates of viscous dissipation rate and 3D viscous dissipation rate were around 0.70 (Figure 3.18). Again, at this reduced resolution, the coefficients of determination between the true, 3D value of viscous dissipation rate and reduced order estimates of kinetic energy were also around 0.70.

3.7 Discussion

Overall, the results show that reduced order estimates of kinetic energy and viscous dissipation rate, such as those calculated in the left ventricle by color-Doppler ultrasound, are correlated with true measures of kinetic energy and viscous dissipation rate. Due to the vortices that appear inside the left ventricle, reduced order estimates were first explored on synthetic velocity fields with analytical vortices. In most cases, coefficients of determination of over 0.80 were seen between 1D and 2D estimates. Then, reduced order estimates of kinetic energy and viscous dissipation rate on a single plane were examined in flow fields in the left ventricle and compared to the true, 3D kinetic energy and viscous dissipation in the entire left ventricle. The estimates with the highest coefficients of determination were the 2D estimates where both the true radial and azimuthal velocities are known. This indicates that if reconstruction methods to calculate the azimuthal component of velocity were perfect, then using both components of velocity would be the best way to estimate the true 3D measures. However, we don't currently have access to measurements of both components of velocity, so we must look to the other estimates. The estimates for 2D reconstructions where the azimuthal components of velocity were calculated from the radial components had similar levels of correlation with the true 3D values as the 1D estimates did with the true 3D values for kinetic energy, but lower correlation for the viscous dissipation rates.

The effect of noise was also studied on the estimates of kinetic energy and viscous dissipation, and it was found that reduced order estimates of kinetic energy were more robust to noise than viscous dissipation. The coefficients of determination between reduced order estimates of kinetic energy and 3D kinetic energy all remained above 0.80. Coefficients of determination between 1D reduced order estimates of viscous dissipation rate and 3D viscous dissipation rate dropped closer to 0.70. However, the coefficients of determination between 2D estimates of kinetic energy and 3D viscous dissipation rate remained above 0.75, meaning that for low resolution data estimates of kinetic energy may be a better predictor of true

viscous dissipation rate than estimates of viscous dissipation rate.

Calculations of viscous dissipation rate are highly sensitive to grid resolution. This was shown in [44], and was confirmed using the synthetic vortices. In addition, for the rigid body vortex, it can be seen that the results are highly influenced by the discrete nature of the problem. While zero viscous dissipation rate was expected, nonzero results (albeit very small) were produced and the results increased with increasing vortex strength. In addition, calculated viscous dissipation rates were orders of magnitude smaller on a finer grid than a coarser grid. The influence of grid resolution is an important consideration when evaluating viscous dissipation rate as a diagnostic tool as many different brands and types of machines can be used to collect data. In addition, each machine often has adjustable settings that could alter the resolution. It is important that diagnostic tools be consistent between hospitals and patients, otherwise it would not be possible to compare viscous dissipation rate between hospitals. For the left ventricle simulation data, we also saw that the coefficients of determination between the reduced order estimates and the 3D values decreased on a coarse grid. The 1D and 2D estimates for kinetic energy and viscous dissipation all dropped to around 0.70.

Overall, reduced order estimates of kinetic energy and viscous dissipation measured by color-Doppler ultrasound in the left ventricle are correlated with true 3D values of kinetic energy and viscous dissipation and should be explored further for use in the clinic. Measures of kinetic energy are more robust to noise and grid resolution than viscous dissipation. Since there are correlations between kinetic energy and viscous dissipation, it may make sense to focus on kinetic energy rather than viscous dissipation.

For the left ventricle, the 1D estimates appeared to give just as strong (for kinetic energy) or stronger (for viscous dissipation) correlations with the 3D values than the 2D estimates achievable with color-Doppler ultrasound, where the second component of velocity is calculated from the first. The 1D values are much easier to calculate than the 2D estimates, making them more clinically viable. If however, the reconstruction of the second component of velocity improves, then it would be advisable to return to the 2D estimates of kinetic energy and viscous dissipation rate, as the 2D estimates when both components of velocity were known gave the strongest correlations.

In addition, we also saw that location of the transducer impacted the predictions of both kinetic energy and viscous dissipation rate. Examining these relationships further can help advise sonographers on ideal locations for the transducer when measuring kinetic energy and viscous dissipation.

The effect of disease was not examined in this chapter, and that is ultimately what is important in the clinic. The relationship between disease and kinetic energy or viscous dissipation rates has been explored in other studies, especially in 3D using MRI, and in some studies in 2D using color-Doppler ultrasound. This study suggests that 1D estimates should be studied in disease states using color-Doppler ultrasound, and that kinetic energy and viscous dissipation rate should be studied in tandem, to determine if there are cases where they provide diverging information or if measuring just kinetic energy will provide the valuable clinical information needed. Overall, this study showed that using color-Doppler

ultrasound to evaluate flow fields in the left ventricle is a promising diagnostic avenue.

Chapter 4

Geometric Modal Analysis as a Three-Dimensional De-Noising and Reconstruction Technique

4.1 Introduction

In addition to blood flow inside the body, a variety of applications require measurement of three-dimensional flow fields, including oceanographic flows and flow around hydrofoils. Tools to measure these flow fields are rapidly improving and becoming more widely available, but the measured data is sparse and noisy, necessitating filtering techniques to de-noise these flow fields. In this chapter, we introduce a modal analysis technique to filter flow fields from a variety of applications. In Chapter 5 we explore this method applied to left ventricle applications.

Four-dimensional flow magnetic resonance imaging (4D-flow MRI) is an important technique for visualizing flow fields inside the body. 4D-flow MRI captures three dimensional flow information in space across multiple time points. It has been used inside the heart to study how flow patterns are related to disease and disease progression [2, 13, 14, 20, 52], but the data is noisy and the image acquisition is time consuming, decreasing its clinical effectiveness. Acquisition parameters for 4D-flow MRI can be tuned to minimize errors in the data, but higher resolution generally comes at the cost of increased acquisition time and other sources of error such as aliasing or velocity-to-noise ratio [53]. A variety of post-processing techniques have been developed to address different sources of error [54, 55].

Outside of the body, particle image velocimetry (PIV) and particle tracking velocimetry (PTV) are two techniques to measure 3D flow fields that benefit from improved filtering of the measured flow data [56]. Modified correlation and reconstruction algorithms have been developed to speed up and improve flow fields measured from particle tracking [57, 58, 59]. However, the results are still noisy and not divergence-free. Therefore, post-processing methods have been implemented to smooth the data after cross-correlation. These methods include local mean, median and band-pass filtering, data convolutions, and a smoothing

algorithm based on the discrete cosine transform for digital PIV [60, 61]. According to the results of the 4th annual PIV challenge, optimizing imaging parameters is still an open question for maximizing spatial resolution without losing accuracy [62], demonstrating that filtering techniques can play an important role in the post-processing of PIV data as imaging parameters and cross-correlation techniques continue to improve.

All of the different measurement devices discussed here are often used to investigate incompressible fluids, and some filtering techniques that take into account incompressibility have been proposed. For example, Schiavazzi et al. use a divergence-free linear filter to de-noise three-dimensional velocity fields [63]. With a focus on turbulent flow, deSilva et al. minimized the difference between the measured and filtered velocity fields while enforcing a divergence-free constraint [64]. To reconstruct and de-noise blood flow data measured with 4D-flow MRI, Song et al. used a projection operation into the space of divergence-free vector fields [65], Busch et al. combined normalized convolution and divergence-free radial basis functions [66], and Santielli et al. combined divergence-free wavelets and the finite difference method to iteratively reconstruct the flow field by regularizing phase and magnitude in alternative iterations [67]. Falahatpisheh et al. reconstructed a 3D flow field from 2D data acquired on multiple planes while enforcing incompressibility [68]. In addition to these methods that strictly enforce a divergence-free condition, other methods have been proposed that penalize non-zero divergence rather than enforcing a strict divergence-free condition, such as the wavelet transforms to account for inaccurate boundary conditions used by Ong et al. [69] and the optimization method described by Assi et al [70].

In addition to the divergence-free condition, accurately quantifying the flow at the boundary is often of importance in flow fields. For example, Lagrangian and particle analyses will be inaccurate if there are particles flowing through the walls when there should be no-slip boundary conditions. Wall shear stress is also an important indicator related to cardiovascular diseases that cannot be properly evaluated when the flow field is not resolved at the walls. To this end, we have developed a modal projection method to de-noise 3D velocity fields such that the resulting field is divergence-free and satisfies no-slip and no-penetration boundary conditions.

Modal analysis is a tool that can be used to filter data by identifying the dominant modes of the system and filtering out other modes with smaller contributions [71]. In general, modal analysis is used to decompose a flow field by identifying the main components of the flow. For example, proper orthogonal decomposition and dynamic mode decomposition are common data-driven methods to break down the flow into its main components. These types of decompositions are data-based techniques because the modes are calculated based on the velocity data. An alternate type of decomposition, and the type of decomposition used in this paper, is geometry-based, where the modes are calculated based on the domain. Some examples of geometry-based modal analysis methods are Lekien et al.'s geometry-based modal decomposition to reconstruct noisy flow data in two dimensions [32] and Chu et al.'s similar method in three dimensions [72].

Here, to de-noise three-dimensional velocity fields, we propose a modal projection method that takes into account the incompressibility of the velocity field. The projection method

works by first solving for a set of geometry-based modes, where each mode is a velocity field. The modes are calculated by solving for velocity fields that minimize velocity gradient, subject to specified boundary conditions, in order to produce smooth velocity fields. In addition, a divergence-free condition is enforced for all modes. Each mode is calculated using information about the geometry of the domain. This method is different than many data-driven modal analysis methods where the modes are calculated from the velocity data itself. By calculating the modes based on the geometry, we take advantage of velocity modes inherent to the geometry. Then, the data is projected onto the modes to produce a new, filtered velocity field.

In this chapter, we describe the method in detail and then apply it to three test cases: flow inside a cube, through a stenosis, and around a cylinder. Multiple versions of the data are used as inputs to the method to represent different imaging acquisitions, including the data with artificial noise added and subsampled versions of the data. Reconstructed velocity fields are compared to the true velocity fields to evaluate the method.

4.2 Theory

Measured velocity fields are reconstructed by calculating a set of divergence-free modes based on the geometry of the domain at a specific time point, and then projecting measured data onto the modes to produce a new, divergence-free velocity field. There are two sets of modes: interior and boundary modes. The interior modes have a no-slip, no-penetration boundary condition on all parts of the boundary and are described in section 4.2.1. These modes capture flow structures based exclusively on the geometry of the domain. The boundary modes have a non-zero velocity through specified parts of the boundary and are described in section 4.2.2. The boundary modes capture flow structures that develop as a result of flow through the boundaries. The optimal combination of modes to reconstruct the velocity field is calculated using a minimization problem described in section 4.2.3.

For a case where the geometry stays the same over time, like the examples explored in this chapter, only one set of modes needs to be calculated. The data can be projected onto the same set of modes at each time point. For a case where the geometry is changing over time, like the examples discussed in Chapter 5, a set of modes is calculated at each time point, and the boundary conditions for the boundary modes can be adjusted to properly capture the flow at the moving boundary.

Both sets of modes are based on minimizing the velocity gradient in a given domain while enforcing specified boundary conditions and a divergence-free condition throughout the domain. In order to de-noise the data, we want to have smooth modes, which motivates the minimization of the velocity gradient. In addition, minimizing the velocity gradient is equivalent to minimizing viscous dissipation in this formulation of the problem. See Appendix A for an extended discussion of the minimization of the velocity gradient.

4.2.1 Interior Modes

Interior Modes Problem Definition

Interior modes are calculated by minimizing the Frobenius norm of the velocity gradient in a given domain, subject to a divergence-free constraint and no flow on or through the boundaries. The problem is defined:

$$\begin{aligned} &\min \left(\int_\Omega \|\nabla \mathbf{U}\|_F^2 dV \right) \\ \text{such that } &\left(\nabla \cdot \mathbf{U} = 0 \right) \\ \text{and } &\left(\mathbf{U} = 0 \text{ on } \partial\Omega \right) \\ \text{and } &\left(\int_\Omega |\mathbf{U}|^2 d\Omega = 1 \right) \end{aligned} \tag{4.1}$$

where $\mathbf{U} = u_1\mathbf{e}_1 + u_2\mathbf{e}_2 + u_3\mathbf{e}_3$ is a mode over the domain Ω with boundary $\partial\Omega$. Each mode is a velocity field where u_i represents the component of velocity in the i^{th} direction. The $\left(\int_\Omega \|\mathbf{U}\|_2^2 dV = 1 \right)$ constraint is required to avoid the trivial solution. The minimization of the norm of the velocity gradient is equivalent to minimizing viscous dissipation (Appendix A).

To solve the problem, we start by defining the functional to minimize, I:

$$I = \int_\Omega \left(\sum_{i=1}^{3} |\nabla u_i|^2 + \lambda \left(\sum_{i=1}^{3} |u_i|^2 - 1 \right) + \mu \sum_{i=1}^{3} \frac{\partial u_i}{\partial x_i} \right) dV \tag{4.2}$$

where λ and μ are Lagrange multipliers used to enforce two of the three constraints. The Lagrange multiplier, λ is a constant because it multiplies an integral constraint and μ is a function of $\mathbf{x}$ because it multiplies a differential constraint. The implementation of the boundary condition, which is the third constraint, is described later.

Next, we take the first variation of our function with respect to our free variables, u_i and μ, and set them equal to 0 to find the minimum. The first variation of the functional with respect to u_i is

$$\delta_{u_i} I = \int_\Omega \left(2\nabla u_i \cdot \nabla(\delta u_i) + 2\lambda u_i \cdot \delta u_i + \mu \frac{\partial(\delta u_i)}{\partial x_i} \right) dV = 0 \text{ for } i = 1, 2, 3. \tag{4.3}$$

The first variation with respect to μ is

$$\delta_\mu I = \int_\Omega \delta\mu \sum_{i=1}^{3} \frac{\partial u_i}{\partial x_i} dV = 0. \tag{4.4}$$

The variables δu_i and $\delta\mu$ can be considered test functions corresponding to u_i and μ, respectively. Then, this problem can be implemented using a finite element formulation.

Implementation - Defining Matrices

To implement the finite element formulation, the trial (u_i, μ) and test (v_i, $\delta\mu$) functions are defined

$$\begin{aligned} u_i(\mathbf{x}) &= \sum_{j=1}^{n} \hat{u}_i^j \varphi^j(\mathbf{x}),\ i = 1,2,3 \\ \delta u_i(\mathbf{x}) &= \sum_{j=1}^{n} \varphi^j(\mathbf{x}),\ i = 1,2,3 \\ \mu(\mathbf{x}) &= \sum_{j=1}^{n} \hat{\mu}^j \varphi^j(\mathbf{x}) \\ \delta\mu(\mathbf{x}) &= \sum_{j=1}^{n} \varphi^j(\mathbf{x}) \end{aligned} \tag{4.5}$$

where n is the number of nodes in the domain, φ is a basis function, and $\hat{u}_i^j$ and $\hat{\mu}_i^j$ are scalar functions of $\mathbf{x}$. The stiffness matrix, $\mathbf{K}$, is defined

$$K_{ij} = \int_\Omega \nabla\varphi_i \cdot \nabla\varphi_j \mathrm{d}V$$

and the mass matrix, $\mathbf{M}$, is

$$M_{ij} = \langle \varphi_i, \varphi_j \rangle = \int_\Omega \varphi_i \varphi_j \ \mathrm{d}V.$$

The matrix $\mathbf{D}$ is defined

$$D_{k,ij} = \langle \frac{\partial \varphi_i}{\partial x_k}, \varphi_j \rangle = \int_\Omega \frac{\partial \varphi_i}{\partial x_k} \varphi_j \ \mathrm{d}V, \qquad k = 1,2,3.$$

Together, the weak form of the problem is:

$$\begin{aligned} \mathbf{K}\boldsymbol{u}^i + \lambda\mathbf{M}\boldsymbol{u}^i + \mathbf{D}^i\boldsymbol{\mu} = 0, \quad i = 1,2,3 \\ \mathbf{D}_1^T\boldsymbol{u}^1 + \mathbf{D}_2^T\boldsymbol{u}^2 + \mathbf{D}_3^T\boldsymbol{u}^3 = 0 \end{aligned} \tag{4.6}$$

where the first equation comes from equation 4.10, the second equation comes from 4.4, and

$$\boldsymbol{u}^i = \left[u_1^i, \cdots, u_n^i\right]^T.$$

The full system is

$$\begin{bmatrix} \mathbf{K} & \mathbf{0} & \mathbf{0} & \mathbf{D}_1 \\ \mathbf{0} & \mathbf{K} & \mathbf{0} & \mathbf{D}_2 \\ \mathbf{0} & \mathbf{0} & \mathbf{K} & \mathbf{D}_3 \\ \mathbf{D}_1^T & \mathbf{D}_2^T & \mathbf{D}_3^T & \mathbf{0} \end{bmatrix} \begin{bmatrix} \boldsymbol{u}^1 \\ \boldsymbol{u}^2 \\ \boldsymbol{u}^3 \\ \boldsymbol{\mu} \end{bmatrix} + \lambda \begin{bmatrix} \mathbf{M} & \mathbf{0} & \mathbf{0} & \mathbf{0} \\ \mathbf{0} & \mathbf{M} & \mathbf{0} & \mathbf{0} \\ \mathbf{0} & \mathbf{0} & \mathbf{M} & \mathbf{0} \\ \mathbf{0} & \mathbf{0} & \mathbf{0} & \mathbf{0} \end{bmatrix} \begin{bmatrix} \boldsymbol{u}^1 \\ \boldsymbol{u}^2 \\ \boldsymbol{u}^3 \\ \boldsymbol{\mu} \end{bmatrix} = \mathbf{0}$$

which can be written in a compact form:

$$\begin{bmatrix} \underline{\mathbf{K}} & \underline{\mathbf{D}} \\ \underline{\mathbf{D}}^T & \mathbf{0} \end{bmatrix} \begin{bmatrix} \underline{\boldsymbol{u}} \\ \boldsymbol{\mu} \end{bmatrix} = -\lambda \begin{bmatrix} \underline{\mathbf{M}} & \mathbf{0} \\ \mathbf{0} & \mathbf{0} \end{bmatrix} \begin{bmatrix} \underline{\boldsymbol{u}} \\ \boldsymbol{\mu} \end{bmatrix} \tag{4.7}$$

where

$$\underline{\mathbf{K}} = \begin{bmatrix} \mathbf{K} & \mathbf{0} & \mathbf{0} \\ \mathbf{0} & \mathbf{K} & \mathbf{0} \\ \mathbf{0} & \mathbf{0} & \mathbf{K} \end{bmatrix}, \quad \underline{\mathbf{D}} = \begin{bmatrix} \mathbf{D}_1 \\ \mathbf{D}_2 \\ \mathbf{D}_3 \end{bmatrix}, \quad \underline{\mathbf{M}} = \begin{bmatrix} \mathbf{M} & \mathbf{0} & \mathbf{0} \\ \mathbf{0} & \mathbf{M} & \mathbf{0} \\ \mathbf{0} & \mathbf{0} & \mathbf{M} \end{bmatrix}, \quad \underline{\boldsymbol{u}} = \begin{bmatrix} \boldsymbol{u}^1 \\ \boldsymbol{u}^2 \\ \boldsymbol{u}^3 \end{bmatrix}.$$

4.2.2 Boundary Modes

Unlike the interior modes, the boundary modes allow flow through the boundary. The parts of the boundary where flow goes through are known as 'open boundaries', and the parts with no flow through are called 'closed boundaries'. Each mode has a distinct boundary condition on the open boundary. Below, the problem formulation is described, followed by a description of how the boundary conditions on the open boundaries are chosen.

If the boundary is moving, there are many different ways to treat this boundary. One way is to treat the moving boundary as an alternative type of 'closed boundary', where instead of no flow at the wall, the velocity boundary conditions at the wall are defined based on wall movement and conservation of mass. See Chapter 5 for a more detailed discussion of moving boundaries.

Boundary Modes Problem Definition

The calculation of the boundary modes is formulated in the same manner as the interior modes, beginning with the minimization of the velocity gradient. However, due to the introduction of a non-zero Dirichlet boundary condition, it is no longer necessary to enforce the norm of velocity to be equal to 1, meaning that this problem is not an eigenvalue problem. The problem is defined:

$$\begin{aligned} &\min \left(\int_\Omega \|\nabla \mathbf{U}\|_F^2 dV \right) \\ \text{such that } &\left(\nabla \cdot \mathbf{U} = 0 \right) \\ \text{and } &\left(\mathbf{U} = \mathbf{U}^b \text{ on } \partial\Omega \right). \end{aligned} \tag{4.8}$$

The velocity on the boundary, $\mathbf{U}^b$, may be equal to 0 on some portions of the boundary, denoted as the 'closed boundary', and may be non-zero on other parts of the boundary, denoted as the 'open boundary'. Determining the appropriate boundary condition is discussed in the next section.

The functional I_b is defined:

$$I_b = \int_\Omega \left(\sum_{i=1}^{3} |\nabla u_i|^2 + \mu \sum_{i=1}^{3} \frac{\partial u_i}{\partial x_i} \right) dV \tag{4.9}$$

where μ is a function of $\mathbf{x}$ because it multiplies a differential constraint. The first variation of the functional with respect to u_i is

$$\delta_{u_i} I_b = \int_\Omega \left(2\nabla u_i \cdot \nabla(\delta u_i) + \mu \frac{\partial(\delta u_i)}{\partial x_i} \right) dV = 0 \text{ for } i = 1, 2, 3. \tag{4.10}$$

The first variation is also taken with respect to μ, yielding the same results as equation 4.4.

Using the same definitions as for the interior modes, the problem is written compactly:

$$\begin{bmatrix} \underline{\mathbf{K}} & \underline{\mathbf{D}} \\ \underline{\mathbf{D}}^T & \mathbf{0} \end{bmatrix} \begin{bmatrix} \underline{\boldsymbol{u}} \\ \underline{\boldsymbol{\mu}} \end{bmatrix} = \underline{\mathbf{0}} \tag{4.11}$$

Determining the boundary condition

There are a few ways to determine the appropriate boundary conditions for the boundary modes. If the boundary conditions are known exactly, a single boundary mode can be used where $\mathbf{U}^b$ is equal to the known boundary condition. If the exact flow through the boundary is not know, we must develop a set of boundary conditions, where each boundary condition corresponds to one boundary mode. One method to accomplish this is to assume the flow through the boundary, $\mathbf{U}_b$, is perpendicular to the boundary, and then solve for a scalar set of modes on the open boundary where the magnitude of the velocity on the boundary is equal to the value of the scalar field at that point. Therefore, flow on the boundary satisfies

$$\mathbf{n} \cdot \mathbf{U}^b = g_i(s) \text{ on } \partial\Omega \tag{4.12}$$

where g_i is set to 0 on the closed boundary. Any set of modes could be chosen for the open boundary. In our case, we use the set of scalar modes, g_i, that are the solution to the Laplace eigenvalue problem on the open boundary:

$$\begin{aligned} \Delta g_i &= -\lambda_i^g g_i \\ g_i &= 0 \text{ on } \partial(\partial\Omega) \end{aligned} \tag{4.13}$$

where $\partial(\partial\Omega)$ is the edge of the open boundary. These scalar modes, g_i, form an orthogonal basis on our open boundary.

Modification: Single Boundary Mode

If the flow through the boundary is not perpendicular to the boundary and also has some noise associated with it, a slight modification to the boundary mode method can be made.

Each component of velocity through the open boundary can be projected on scalar modes, to come up with a single boundary condition that is not necessarily normal to the boundary. First, the scalar modes described in equation 5.1 are solved on the open boundary, just as they would be in the previously described version. Then, a single new boundary condition, $\mathbf{U}^b$ is defined where the magnitude of each component of velocity is reconstructed as a weighted sum of the modes, g_i:

$$\begin{aligned}\mathbf{U}^b =& u^{b,1}\mathbf{e}_1 + u^{b,2}\mathbf{e}_2 + u^{b,3}\mathbf{e}_3\\ u^{b,1} =& \sum_i a_i g_i\\ u^{b,2} =& \sum_i b_i g_i\\ u^{b,3} =& \sum_i c_i g_i\end{aligned}$$

where a_i, b_i, and c_i are constants.

These constants are determined by three least squares problems. The least squares problems seek to minimize the difference between each component of the reconstructed field and the measured velocity field

$$\min_{a_i,b_i,c_i} \|u^{data,j} - u^{b,j}\|_2^2, \text{ for } j = 1,2,3$$

where $u^{data,j}$ is the j^{th} component of the measured velocity data on the boundary. The result of this method is a single velocity field on the boundary, which yields a single boundary mode.

Implementation: Uzawa - Conjugate Gradient

To solve for boundary modes, a modified version of the Uzawa iteration algorithm with the Conjugate Gradient method is implemented to solve the system of equations.

We start by rewriting the boundary problem as follows:

$$\begin{bmatrix}\mathbf{K} & \mathbf{0} & \mathbf{0} & \mathbf{G}_1\\ \mathbf{0} & \mathbf{K} & \mathbf{0} & \mathbf{G}_2\\ \mathbf{0} & \mathbf{0} & \mathbf{K} & \mathbf{G}_3\\ \mathbf{G}_1^T & \mathbf{G}_2^T & \mathbf{G}_3^T & \mathbf{0}\end{bmatrix}\begin{bmatrix}\boldsymbol{u}^1\\ \boldsymbol{u}^2\\ \boldsymbol{u}^3\\ \boldsymbol{\mu}\end{bmatrix} = \begin{bmatrix}\boldsymbol{b}^1\\ \boldsymbol{b}^2\\ \boldsymbol{b}^3\\ \boldsymbol{b}_{BC}\end{bmatrix} = \begin{bmatrix}\mathbf{0}\\ \mathbf{0}\\ \mathbf{0}\\ \boldsymbol{b}_{BC}\end{bmatrix}$$

where

$$\mathbf{G}_1 = \begin{bmatrix}\mathbf{D}_1 & \mathbf{BC}_{v_x} & \mathbf{0} & \mathbf{0}\end{bmatrix}, \mathbf{G}_2 = \begin{bmatrix}\mathbf{D}_2 & \mathbf{0} & \mathbf{BC}_{v_y} & \mathbf{0}\end{bmatrix}, \mathbf{G}_3 = \begin{bmatrix}\mathbf{D}_3 & \mathbf{0} & \mathbf{0} & \mathbf{BC}_{v_z}\end{bmatrix}$$

and

$$\boldsymbol{b}_{BC} = \begin{bmatrix}\mathbf{0} & \boldsymbol{BC}_{v_x}\end{bmatrix}^T.$$

We can then rewrite equations for $\boldsymbol{u}^i$

$$\begin{aligned}\boldsymbol{u}^1 &= \mathbf{K}^{-1}(\boldsymbol{b}^1 - \mathbf{G}_1\boldsymbol{\mu})\\ \boldsymbol{u}^2 &= \mathbf{K}^{-1}(\boldsymbol{b}^2 - \mathbf{G}_2\boldsymbol{\mu})\\ \boldsymbol{u}^3 &= \mathbf{K}^{-1}(\boldsymbol{b}^3 - \mathbf{G}_3\boldsymbol{\mu})\end{aligned}$$

and define the Schur Complement

$$\begin{aligned}-(\mathbf{D}_1^T\mathbf{K}^{-1}\mathbf{D}_1 + \mathbf{D}_2^T\mathbf{K}^{-1}\mathbf{D}_2 + \mathbf{D}_3^T\mathbf{K}^{-1}\mathbf{D}_3)\boldsymbol{\mu} =& \boldsymbol{b}_{BC} - \mathbf{D}_1^T\mathbf{K}^{-1}\boldsymbol{b}_1 + \mathbf{D}_2^T\mathbf{K}^{-1}\boldsymbol{b}_2 + \mathbf{D}_3^T\mathbf{K}^{-1}\boldsymbol{b}_3\\ =& \boldsymbol{b}_{BC}\\ \mathbf{S} =& \mathbf{D}_1^T\mathbf{K}^{-1}\mathbf{D}_1 + \mathbf{D}_2^T\mathbf{K}^{-1}\mathbf{D}_2 + \mathbf{D}_3^T\mathbf{K}^{-1}\mathbf{D}_3\end{aligned}$$

To start the iterative process we initialize a few variables

$$\begin{aligned}\dot{\boldsymbol{\mu}} &= 0\\ \mathbf{K}\dot{\boldsymbol{u}}^1 &= \boldsymbol{b}^1 - \mathbf{G}_1\dot{\boldsymbol{\mu}}\\ \mathbf{K}\dot{\boldsymbol{u}}^2 &= \boldsymbol{b}^2 - \mathbf{G}_2\dot{\boldsymbol{\mu}}\\ \mathbf{K}\dot{\boldsymbol{u}}^3 &= \boldsymbol{b}^3 - \mathbf{G}_3\dot{\boldsymbol{\mu}}.\end{aligned}$$

Then we solve for initial values for $\dot{\boldsymbol{u}}^1$, $\dot{\boldsymbol{u}}^2$, and $\dot{\boldsymbol{u}}^3$.

To meet the LBB stability condition, either P2-P1 elements or a stabilization matrix $\mathbf{C}$ can be used.

4.2.3 Projection of Data onto Modes

Once all the modes have been calculated, they are combined to form a new, reconstructed velocity field. This reconstructed velocity field, $\mathbf{U}_r$, is equal to the sum of the modes, each multiplied by a constant:

$$\mathbf{U}_r = \sum_{i=1}^{N_I} \alpha_i^I \boldsymbol{u}_i^I + \sum_{i=1}^{N_b} \alpha_i^b \boldsymbol{u}_i^b = \sum_{i=1}^{N} \alpha_i \boldsymbol{u}_i \tag{4.14}$$

where $\mathbf{u}_i^I$ are interior modes, $\mathbf{u}_i^b$ are boundary modes, N_I is the number of interior modes available, N_b is the number of boundary modes available, and $N = N_I + N_b$.

There are multiple methods that can be used to determine the coefficients, α. The most straightforward way is to minimize the difference between the measured velocity field and the reconstructed velocity field using least squares. More advanced ways can incorporate more information, such as how the velocity field changes in time. However, in this chapter we will only consider the least squares problem:

$$\begin{aligned}\min_{\alpha} \|\mathbf{U}_{true} - \mathbf{U}_r\|_2^2 &= \min_{\alpha} \|\mathbf{U}_{true} - (\sum_{i=1}^{N_I} \alpha_i^I \boldsymbol{u}_i^I + \sum_{i=1}^{N_b} \alpha_i^b \boldsymbol{u}_i^b)\|_2^2\\ &= \min_{\boldsymbol{\alpha}} \|\mathbf{U}_{true} - \mathbf{A}\boldsymbol{\alpha}\|_2^2\end{aligned}$$

where each column of $\mathbf{A}$ contains information for one mode.

Since the reconstructed field is developed with a finite element formulation, the result is a continuous velocity field. Another way to calculate the coefficients is to project the available data onto a finite element function space and minimize the difference between the measured and reconstructed velocity fields on this continuous space.

$$\begin{aligned}
\min_{\boldsymbol{\alpha}} \int_\Omega \left(\mathbf{U}_{true} - \mathbf{U}_r \right)^2 dV & \\
= \min_{\boldsymbol{\alpha}} \int_\Omega \left(\sum_{i=1}^{n} \bar{u}_i \varphi_i - \sum_{j=1}^{N} \alpha_j \sum_{k=1}^{n} \hat{u}_k \varphi_k \right)^2 dV & \\
= \min_{\boldsymbol{\alpha}} \int_\Omega \Bigg(\sum_{i=1}^{n} \bar{u}_i \varphi_i \sum_{j=1}^{n} \bar{u}_j \varphi_j - 2 \sum_{i=1}^{n} \bar{u}_i \varphi_i \sum_{j=1}^{N} \alpha_j \sum_{k=1}^{n} \hat{u}_k \varphi_k & \\
+ \sum_{j=1}^{N} \alpha_j \sum_{k=1}^{n} \hat{u}_k \varphi_k \sum_{m=1}^{N} \alpha_m \sum_{n=1}^{n} \hat{u}_n \varphi_n \Bigg) dV & \\
= \min_{\boldsymbol{\alpha}} F(\boldsymbol{\alpha}, \hat{u}, \bar{u}) & \\
0 = \frac{\partial F}{\partial \alpha_i} & \\
= \int_\Omega -2 \sum_{i=1}^{n} \bar{u}_i \varphi_i \sum_{k=1}^{n} \hat{u}_k \varphi_k + 2 \sum_{j=1}^{n} \alpha_j \sum_{k=1}^{n} \hat{u}_k \varphi_k \sum_{n=1}^{n} \hat{u}_n \varphi_n dV & \\
0 = - \mathbf{A}^T \mathbf{M} \mathbf{U}_{true} + \mathbf{A}^T \mathbf{M} \mathbf{A} \boldsymbol{\alpha} & \\
\mathbf{A}^T \mathbf{M} \mathbf{A} \boldsymbol{\alpha} = \mathbf{A}^T \mathbf{M} \mathbf{U}_{true} & \\
\boldsymbol{\alpha} = (\mathbf{A}^T \mathbf{M} \mathbf{A})^{-1} \mathbf{A}^T \mathbf{M} \mathbf{U}_{true} &
\end{aligned}$$

4.2.4 Error Calculation

To evaluate the quality of the reconstruction, the reconstructed velocity field was compared to the true velocity field. The normalized root mean square error was determined:

$$Error = \frac{\sqrt{\frac{1}{n} \sum_{j=1}^{n} \sum_{i=1}^{3} (v_{i,true}^j - v_{i,reconstructed}^j)^2}}{\frac{1}{n} \sum_{j=1}^{n} \left(\sqrt{\sum_{i=1}^{3} (v_{i,true}^j)^2} \right)} \tag{4.15}$$

where v_i^j is the i^{th} component of velocity at the j^{th} point, and n is the number of points in the velocity field.

4.3 Application to Test Problems

Three different test cases were used to evaluate the quality of reconstructed flow fields using this method. The first case is synthetic flow inside a cube with sinusoidal body forces. The cube has no flow through any of the boundaries, so only interior modes are used to reconstruct the velocity field. The second case is flow around a cylinder in a rectangular channel with a Reynolds number of about 300. The diameter of the cylinder is c, and the dimensions of the channel are $5c$ by $5c$ by $25c$, with the cylinder located in the center of the channel and a distance of $7.5c$ from the inlet. The third test case is flow through an idealized stenosis.

4.3.1 Modes

First, modes were calculated for each type of geometry. Figure 4.1 and Figure 4.2 show streamlines of the first few modes in the cube and stenosis geometry respectively.

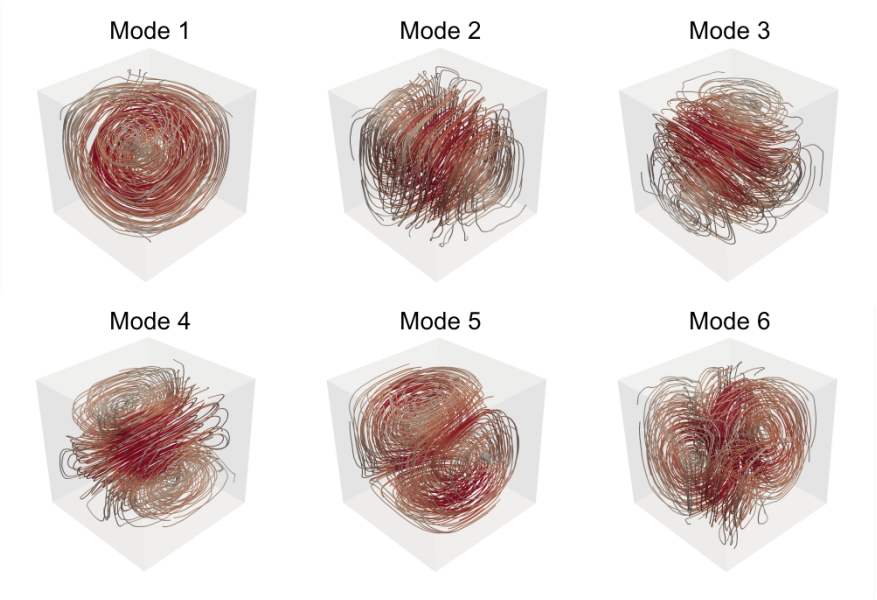

Figure 4.1: Streamlines for interior modes inside a cube.

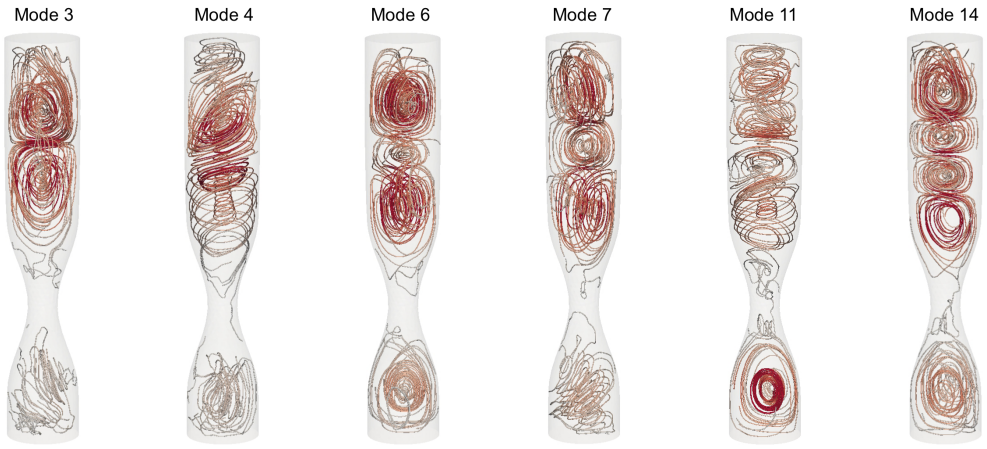

Figure 4.2: Streamlines for interior modes inside a stenosis.

4.3.2 Reconstruction

To test the ability of the method to accurately capture flow structures in a given velocity field, the reconstruction algorithm was first tested on known flow fields without noise. Below, we will show that across all test cases, large flow structures were captured in the reconstructions and increasing the number of modes used in the reconstruction decreased the error.

To test the potential performance of the reconstruction algorithm with experimental data, artificial noise was added to the example flow fields to better represent what image data would look like. Two types of noise were considered to represent different types of imaging data. In the first type, random noise was added directly to the velocity field. Gaussian noise with a zero average and standard deviation of 5%, 10%, 25% and 50% of the maximum velocity component was added to each component of the velocity. In the second, 'MRI type', noise, a signal was calculated using the five-point balanced flow-encoding method described by Johnson and Markl, noise was added to the signal with varying magnitudes, and then the velocity fields were re-calculated from the signal [73, 69]. Both types of noise were tested for all test cases. We will show that geometric modal analysis successfully reduced the error in the velocity field for both types of noise.

In addition, the results were compared to two other methods - the Finite Difference Method (FDM) described by Song et al. [65] and the Radial Basis Function Method (RBF) described by Busch et al. [66]. The reconstructions using FDM and RBF were implemented using MATLAB code made available by Frank Ong [69]. The original data for the stenosis is provided on an unstructured grid and the reconstruction method described in the paper was performed on this unstructured grid. However, the comparison methods are implemented on data that is interpolated onto a structured grid with a comparable mesh size for the FDM and RBF reconstructions.

Cube

First, the interior modes were tested on a synthetic flow field inside a cube. There is no flow on or through the boundary, so only interior modes are used in the reconstruction. The streamlines of the reconstructed velocity fields appear to match closely with the true velocity field for a wide range of number of modes used to reconstruct the velocity field (Figure 4.3A-C). It can be seen that increasing the number of interior modes decreased the mean and median of the error (Figure 4.4).

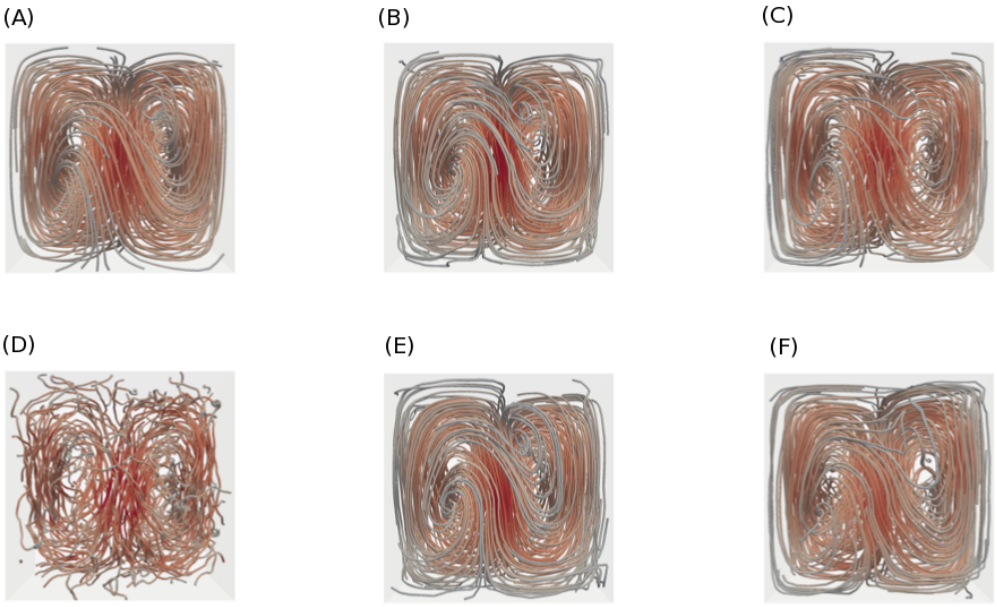

Figure 4.3: Streamlines for synthetic flow inside a cube. (A) is the true velocity field. (B) is the reconstruction from the true velocity field using 44 interior modes. (C) is the reconstruction from the true velocity field using 500 interior modes. (D) is a noisy velocity field. (E) is the reconstruction from the noisy velocity field in D using 44 interior modes. (F) is the reconstruction from the noisy velocity field in D using 500 interior modes.

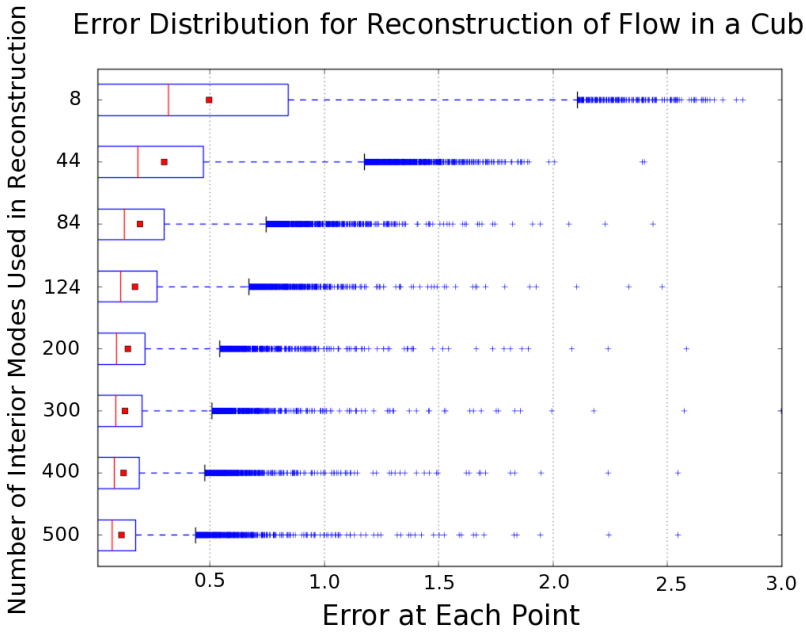

Figure 4.4: Point-by-point error distribution for velocity field reconstructed directly from the results of the simulation for synthetic flow in a cube. Each box represents a different reconstruction using a different number of modes.

When noise was added to the original velocity field, increasing the number of interior modes used in the reconstruction decreased the normalized root mean square error for almost all levels of noise tested for Gaussian and MRI-type error (Figures 4.3 and 4.5). As the error in the noisy field increased, the difference in the performance of the reconstruction between the fewest number of modes and the most number of modes decreased. For very high levels of noise, using the maximum number of modes available ceased to produce the lowest error. For all levels of noise, the velocity field produced by the modal projection method described here had lower root mean square error than the velocity fields produced by FDM and RBF for high numbers of modes used to reconstruct the velocity field.

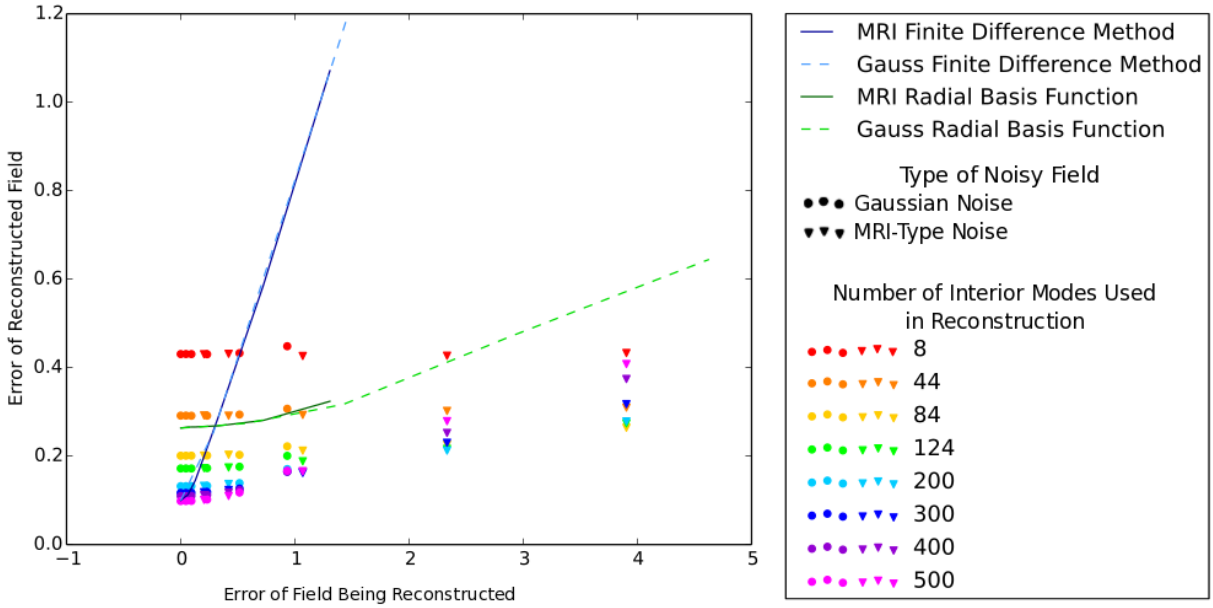

Figure 4.5: Normalized root mean square errors in reconstructed velocity fields for the flow inside a cube when Gaussian noise was added (circles and dashed) and when MRI-type noise was added (triangles and solid). The results are compared to results from two other types of reconstructions.

Flow around a cylinder

For the flow through a channel around a cylinder, increasing the number of interior modes decreased the error. This can be seen in Figure 4.6 where the x-value is 0, meaning that there is no noise added to the velocity field that is input into the reconstruction algorithm. The streamlines for the true field and two different reconstructions appear in Figure 4.7, where we can see that increasing the number of modes helps straighten out the flow downstream from the cylinder and better captures the recirculation region directly downstream from the cylinder.

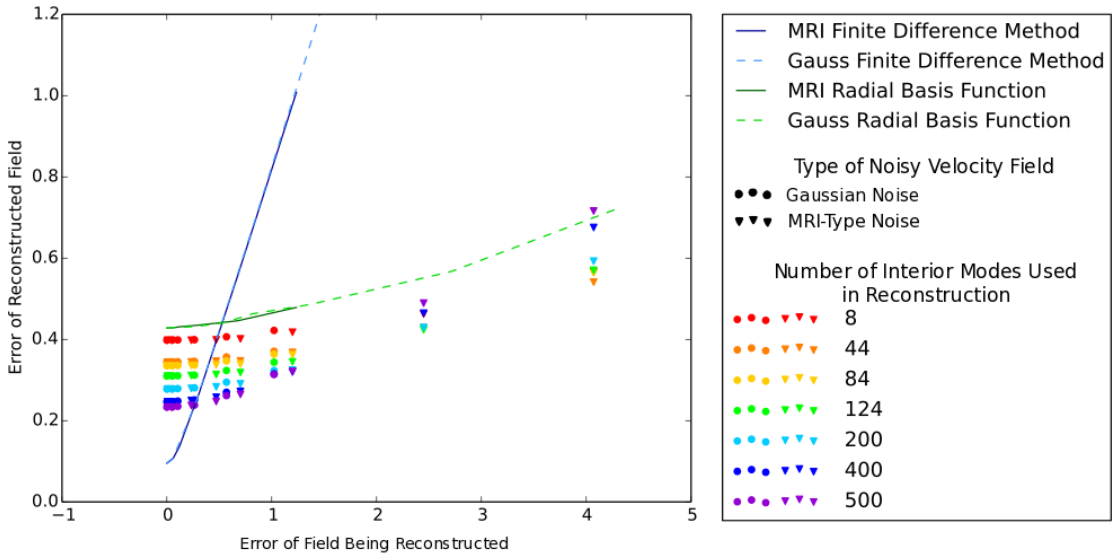

Figure 4.6: Root mean square error for reconstructions of velocity fields with varying degrees of noise in flow around a cylinder. Each point represents the root mean square error over an entire velocity field. The x-axis is the root mean square error of the velocity field that is input to the algorithm, and the y-axis is the root mean square error of the reconstructed velocity field output from the algorithm. Multiple different numbers of modes are used to reconstruct the flow field, which is indicated by color, and the results are compared to two other types of reconstructions.

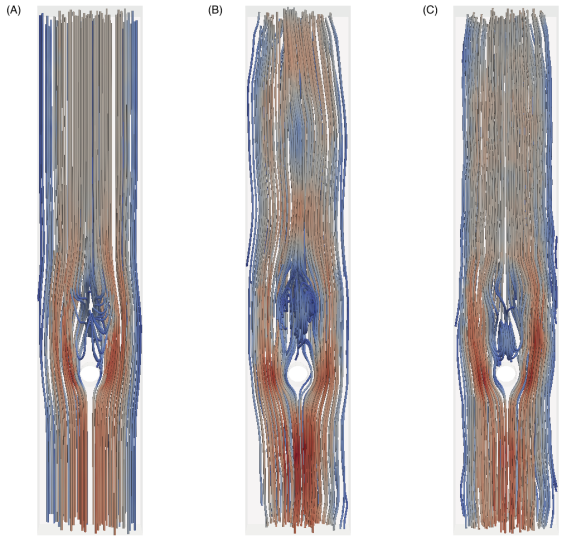

Figure 4.7: Streamlines of flow through a channel around a cylinder. (A) True flow through a channel around a cylinder. (B) Flow through a channel reconstructed from true with 44 interior modes and 48 boundary modes. (C) Flow through a channel reconstructed from true with 400 interior modes and 48 boundary modes.

When noise was added to the original flow field, the reconstruction significantly reduced the noise in the velocity fields and captured the main flow structures (Figure 4.8). The number of modes that produced the best reconstruction depended on the amount of noise added to the flow field (Figure 4.6). For reconstruction of velocity fields with a noise standard deviation of 25% of the maximum velocity magnitude, for the different numbers of modes tested, the lowest errors were achieved with around 200 interior modes and 48 boundary modes. For reconstruction of velocity fields with a noise standard deviation of 25% of the maximum velocity magnitude, improved reconstructions were achieved when fewer modes were available. This is due to the fact that the flow structures are relatively simple and when more modes are available, the reconstruction begins to capture the noise rather than filtering it out.

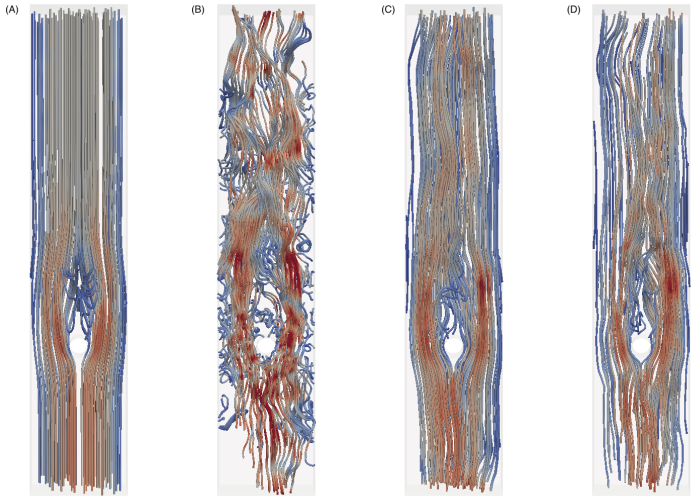

Figure 4.8: Streamlines of flow through a channel around a cylinder. (A) True flow through a channel. (B) Flow through a channel with artificial noise added with a maximum magnitude of 25% of the maximum velocity magnitude. (C) Noisy flow through a channel reconstructed with 84 interior modes and 48 boundary modes. (D) Noisy flow through a channel reconstructed with 400 interior modes and 48 boundary modes.

Stenosis

For the stenosis, increasing the number of interior modes decreased the mean of the error (Figure 4.9). The overall trend of the results was very similar to those seen for the flow around a cylinder. Streamlines for the original and two reconstructions are shown in Figure 4.10A-C.

For the reconstruction of noisy flow in an idealized stenosis, similar trends for noisy reconstructions were observed (Figure 4.9). Streamlines for velocity fields reconstructed

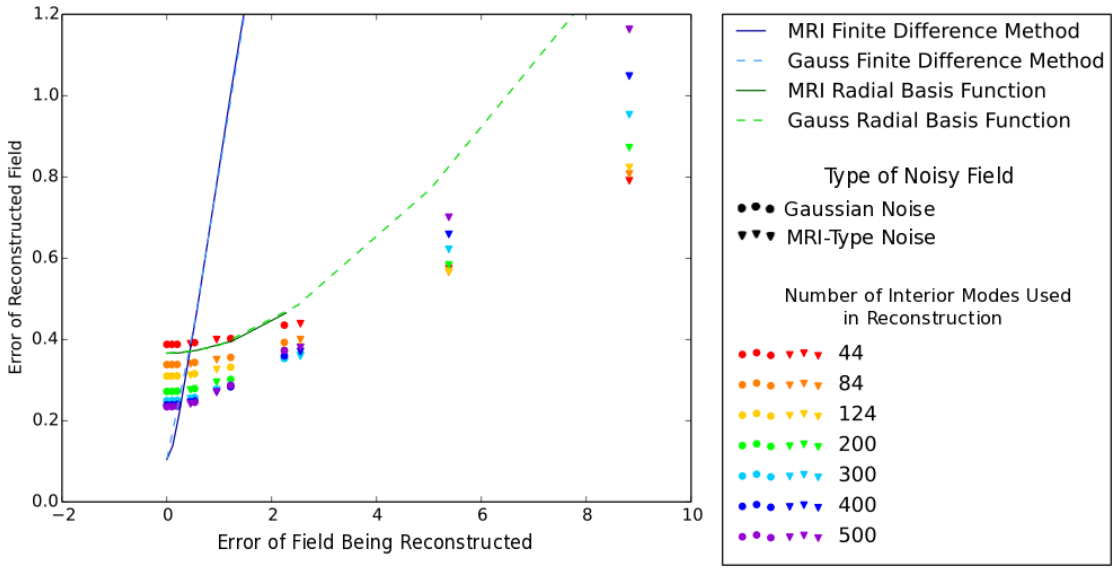

Figure 4.9: Root mean square errors in reconstructed velocity fields for the flow through a stenosis when Gaussian noise was added (A) and when MRI-type noise was added (B). The results are compared to results from two other types of reconstructions.

from a noisy velocity field are shown in Figure 4.10D-F. When noise with a noise standard deviation of 25% of the maximum velocity magnitude was added to the stenosis velocity field, the number of modes did not change the error of the reconstructed velocity field. For MRI-type noise with a standard deviation of 25% of the maximum velocity magnitude, increasing the number of modes decreased the error (Figure 4.9).

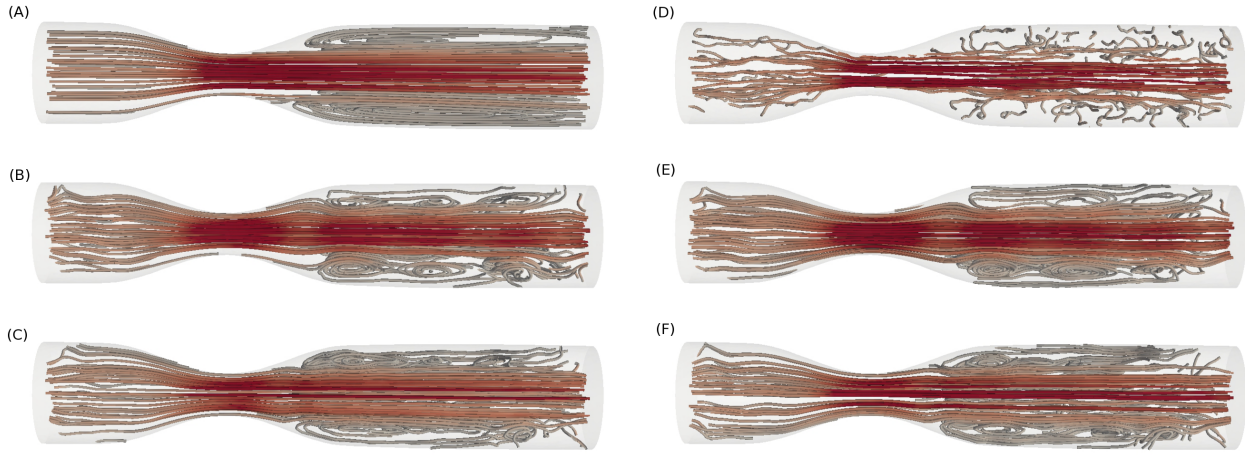

Figure 4.10: Streamlines of the velocity field in an idealized stenosis. Colors represent velocity magnitude. Flow is from bottom to top. (A) The true velocity field from the result of a simulation. (B) Velocity field reconstructed from true with 84 interior modes and 64 boundary modes. (C) Velocity field reconstructed from true with 300 interior modes and 64 boundary modes. (D) Noisy field generated using MRI type noise. (E) Velocity field reconstructed from the noisy field with 84 interior modes and 64 boundary modes. (F) Velocity field reconstructed from the noisy field with 300 interior modes and 64 boundary modes.

Overall, we saw expected trends in the modal analysis projection onto the results of a simulation when no noise was added to the velocity field, with errors of the reconstructed fields decreasing with increasing numbers of modes. The median errors were below 10% for the cylinder and the stenosis, and mean errors were below 20% for the cylinder and 30% for the stenosis. One limitation to the test problems shown here is that the grids were very coarse. We expect that with finer grids, the errors of the reconstructed velocity fields would continue to decrease. However, the coarseness of the grids is more representative of what is seen experimentally.

When looking at the distribution of error for different levels of noise added to the velocity field, a few clear trends appear that are consistent between all types of flows seen here. For very large levels of noise added, there is a clear reduction in error in the reconstructed field, regardless of the number of modes used to reconstruct the flow field. For very small errors, the error is small enough to start with that the error of the reconstructed flow field is larger than the error of the original flow field. For other, intermediate levels of error, the noise is significantly reduced in the reconstruction, and increasing the number of modes used in the reconstructions decreases the errors present in the reconstructed flow field.

4.3.3 Fitting to Sparse Data

The least squares projection of data onto modes was performed using only a subset of the available true data to test the performance of the method on sparse data. To do this, only every n^{th} data point was made available to the reconstruction algorithm, where n was varied. For the cube and the stenosis, n was set equal to 2, 3, 5, and 8. The sparse reconstruction was tested on the original data, as well as the noisy data.

In the cube, when every 2^{nd} and 3^{rd} point was used (Figures 4.11a and 4.11b), the results were very similar to when every point was used for all levels of noise tested (Figure 4.5). However, when the amount of data available was reduced further, higher errors in the reconstructions were seen (Figures 4.11c and 4.11d). For fewer numbers of modes used in the reconstructions, the error did not increase significantly, but for larger numbers of modes used in the reconstructions, the increase in error was more noticeable. In particular, when every 2^{nd} and 3^{rd} point was available, increasing the numbers of modes decreased the error, but for every 5^{th} and 8^{th} point, the error initially increased with increasing modes until 124 modes, and then the error began to increase with increasing number of modes. For the most part, these patterns held when noise was added to the original velocity field, although the overall error was higher. Another interesting result was that the errors were higher in the cube reconstruction when every 5^{th} point was used than when every 8^{th} point was used. This is likely because the mesh on the cube is a structured grid with a multiple of 5 nodes in each direction, so when every 5^{th} point is used, the available data lines up in a few parallel planes, whereas when every 8^{th} point is used the points are distributed more evenly across the whole cube.

The results for sparse reconstructions were very similar for the stenosis compared to the cube. For the stenosis, for the lower levels of error in the initial velocity field, when the reconstructions were completed using every 2^{nd} and 3^{rd} point, the error is not too much larger than when reconstructed using every point (Figures 4.12a and 4.12b compared to Figure 4.9). However, the error is higher in the reconstruction when the original field has higher levels of noise in it. In addition, at these higher levels, increasing the number of modes used in the reconstruction doesn't always decrease the error. When the flow is reconstructed using every 5^{th} point, the error of the reconstructed field about doubles, and again for high levels of initial noise, increasing the number of modes does not necessarily decrease error. When the flow is reconstructed using every 8^{th} point, the error in the reconstructed field is much higher and the error does not decrease with increasing modes even for low levels of initial error. Overall, for moderate levels of sparsity, the method was able to perform reconstructions with relatively low levels of error, but at higher levels of sparsity, the reconstruction method does not perform very well.

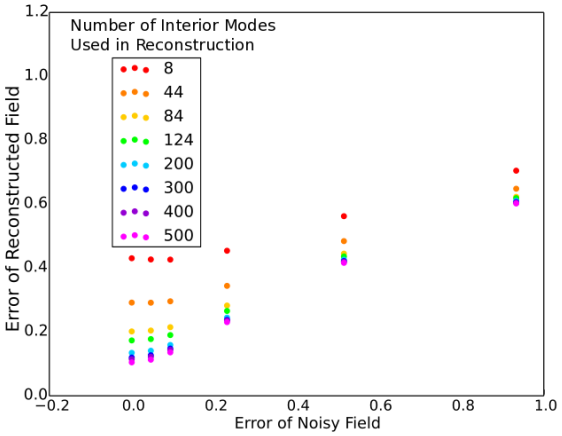

(a) Normalized root mean square error for velocity field reconstructed from every 2^{nd} point for flow inside a cube.

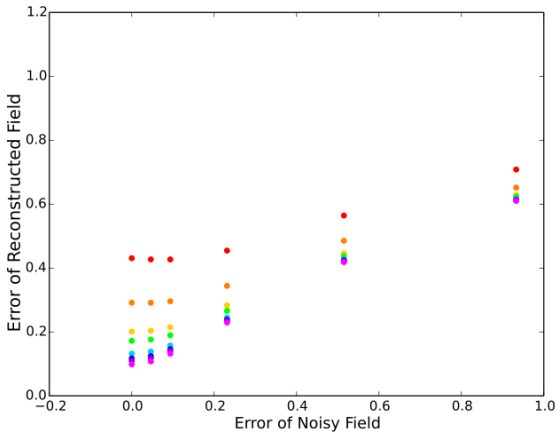

(b) Normalized root mean square error for velocity field reconstructed from every 3^{rd} point for flow inside a cube.

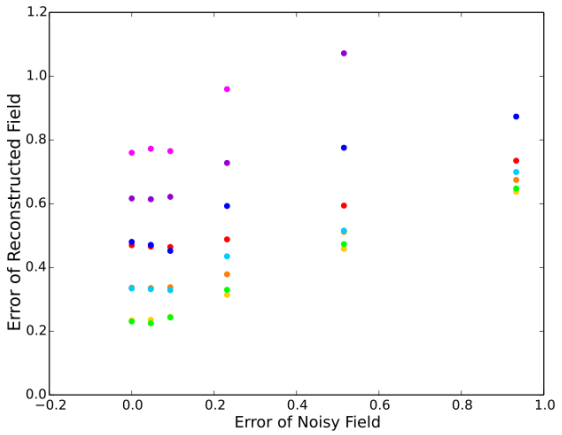

(c) Normalized root mean square error for velocity field reconstructed from every 5^{th} point for flow inside a cube.

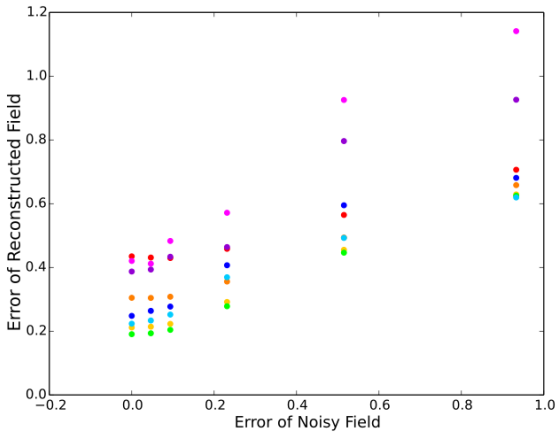

(d) Normalized root mean square error for velocity field reconstructed from every 8^{th} point for flow inside a cube.

Figure 4.11: Normalized root mean square error in reconstructed velocity fields for flow in a cube when reconstructed with only a subset of the data.

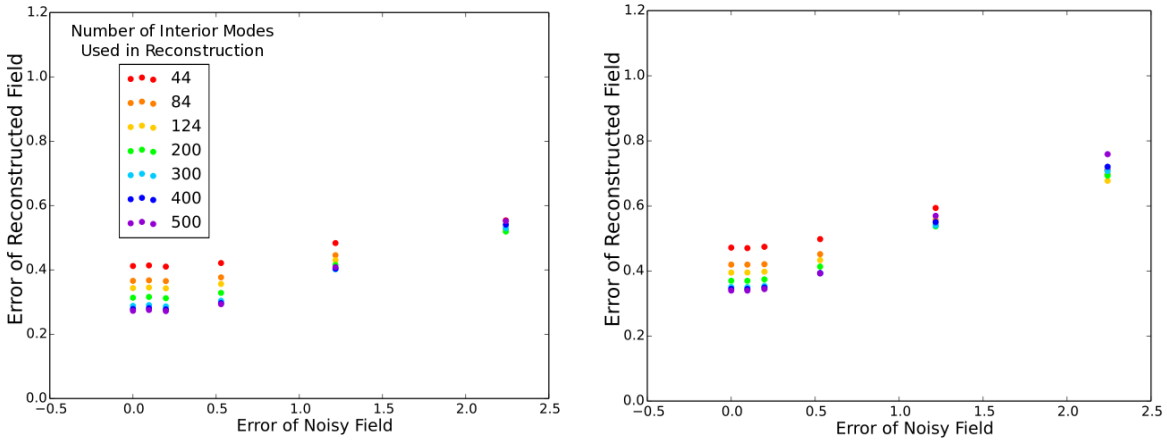

(a) Normalized root mean square error for velocity field reconstructed from every 2^{nd} point for flow through a stenosis.

(b) Normalized root mean square error for velocity field reconstructed from every 3^{rd} point for flow through a stenosis.

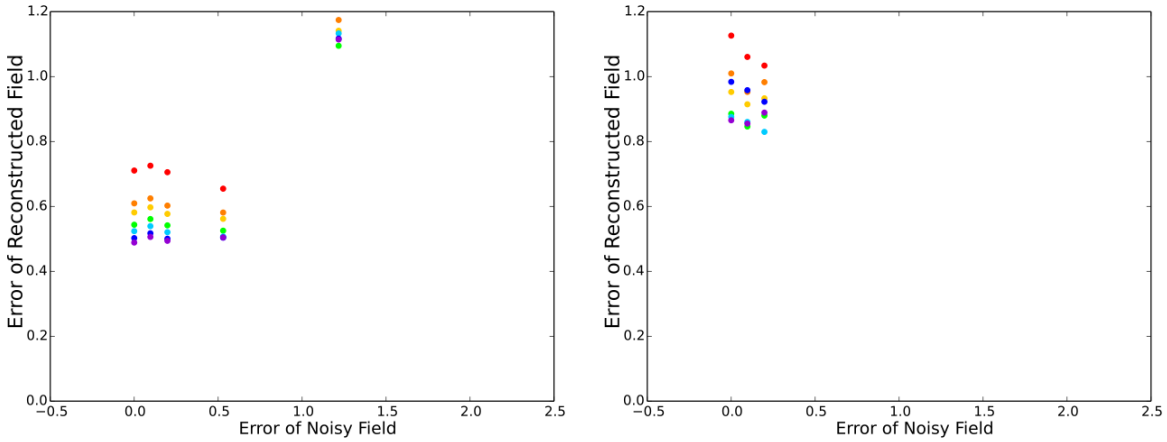

(c) Normalized root mean square error for velocity field reconstructed from every 5^{th} point for flow through a stenosis.

(d) Normalized root mean square error for velocity field reconstructed from every 8^{th} point for flow through a stenosis.

Figure 4.12: Normalized root mean square error in reconstructed velocity fields for flow in an idealized stenosis when reconstructed with only a subset of the data. Each reconstruction uses 64 boundary modes, and a varying number of interior modes, indicated by color.

4.3.4 Fitting to One and Two Components of Velocity

Next, the reconstruction for the cube and flow through a stenosis was performed with only one or two components of velocity available. For the cube, when only one component of velocity was available, the reconstructions were very poor. However, when two components were available, the results were comparable to when three components were available (Figure 4.14). These results follow naturally from the fact that we are reconstructing a divergence-free flow. In a divergence-free flow field, if two components of velocity and boundary conditions are known, the third component of velocity can be calculated.

For the stenosis it is important to note that the majority of the flow is in the y-direction, through the stenosis. Fitting to only one component of velocity did not produce anything meaningful, although when only the y component of velocity was used the errors were significantly lower than using only the x or z component. When two components of velocity were used, if one of these components was the y component then we saw expected patterns with the reconstructions. However, when only the x and z components were used the errors were very large.

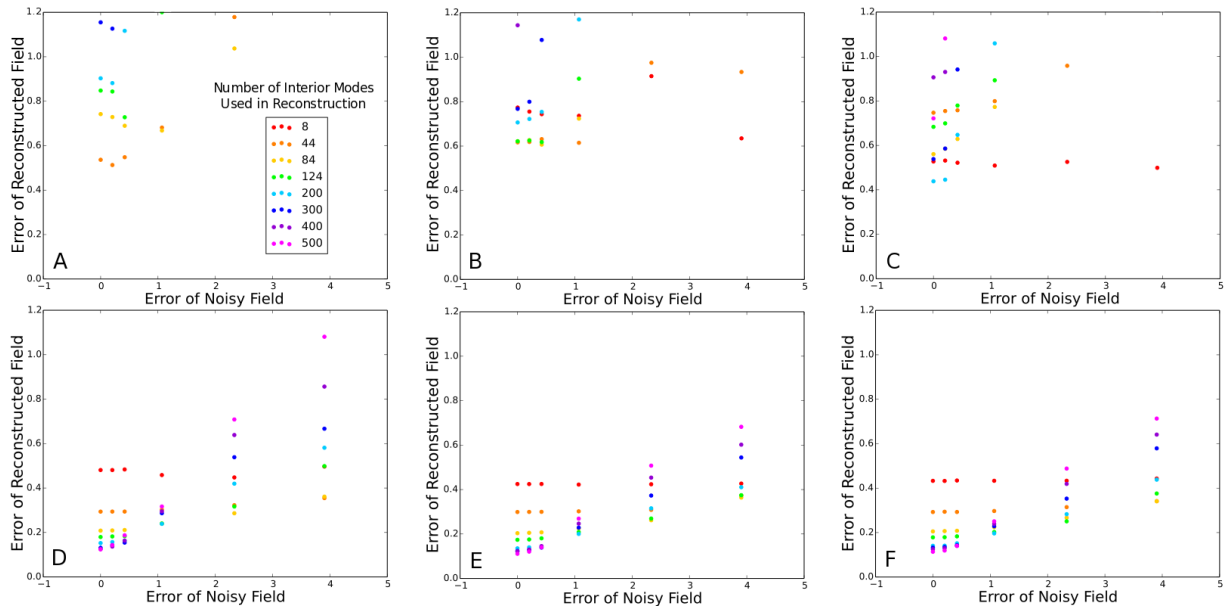

Figure 4.13: Normalized root mean square errors for velocity fields reconstructed from limited information for the cube - i.e. only one or two components of velocity. (A) shows reconstructed from the x component of velocity, (B) shows the y component, (C) shows the z component, (D) shows reconstructed from the x and y components, (E) shows x and z components, and (F) shows y and z components.

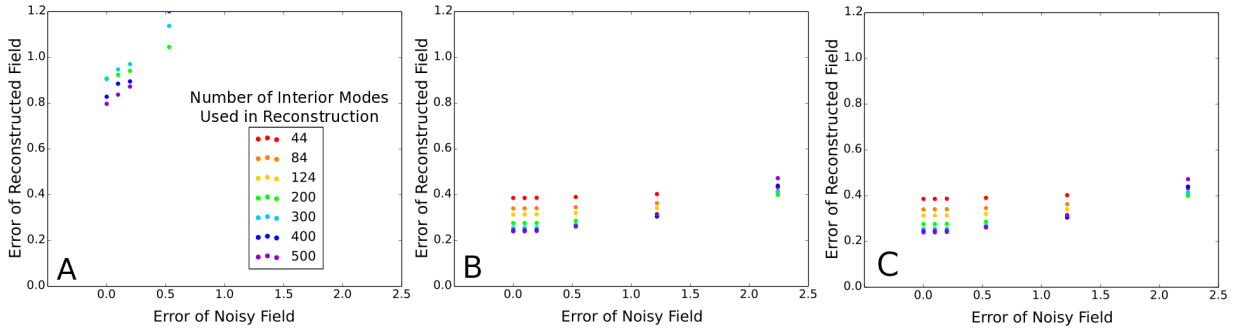

Figure 4.14: Normalized root mean square errors for velocity fields reconstructed from limited information for a stenosis - i.e. only one or two components of velocity. (A) shows reconstructed from the x component of velocity, (B) shows reconstructed from the x and y components, (C) shows y and z components.

4.4 Discussion

A method to reconstruct noisy and sparse velocity fields from measurements was developed and tested on coarsely-meshed test-problems. Overall, expected trends of decreasing error for increasing modes at lower levels of noise, with the pattern reversing for very high levels of noise, were seen, which is a promising initial result. The number of modes used to get the best reconstruction of a flow field is dependent on the magnitude of the noise present in the data and the complexity of the flow. Therefore, this reconstruction technique will need to be tailored for each application that it is used for. In the future, we expect the method to be even more successful and useful for 'geometry-driven-flows,' such as flow inside the heart.

An important consideration when developing de-noising and reconstruction methods is the ability to test the quality of the method. In the examples presented in this chapter, results from computational fluid dynamics simulations were used, where a true velocity field is available. This method will ultimately be used on velocity fields where the truth is not known, making it impossible to test the 'success' of the method. It is therefore important to be confident in the method's ability to de-noise and reconstruct velocity fields before applying it to data where the truth is unknown. There are still improvements that can be made to the method and with each adjustment, the results should be evaluated using velocity fields where the 'truth' is available, before moving to more realistic applications.

In order to achieve better results, one possible adjustment is to incorporate other information during the projection. For example, many of the flows we are interested in are changing in time. An extra term can be introduced in the least squares problem that penalizes changes in the contributions of each mode between time steps. This method has the potential to be helpful when the change in time between images is small, meaning that the flows at the two time steps are related to each other but the noise is not.

This method also has the potential to be used in cases where only one or two components of velocity are available. Color-Doppler ultrasound is one such application, where only a

single component of velocity, parallel to the ultrasound beam, is available. Traditional color-Doppler ultrasound is only available on a single plane, but recent advancements have led to the availability of multi-plane ultrasound where a single component of velocity, parallel to the ultrasound beam, is available in multiple parallel planes, creating a three-dimensional domain. The geometry of the heart can also be measured using multi-plane ultrasound, making this method well-suited for this application.

Ideally, this method could be tailored to each application so that the optimal number and types of modes are available to easily and accurately reconstruct a velocity field from sparse and noisy data. For future work, one may consider investigating different types of problems individually to determine the necessary types and numbers of modes required to reconstruct the velocity fields for a given application with a typical level of noise. In Chapter 5, we apply this method to blood flow in the left ventricle.

Chapter 5

Geometric Modal Analysis: Left Ventricle Examples

5.1 Introduction

In this chapter, we assess the ability of the modal projection method described in Chapter 4 to filter and reconstruct velocity fields in the left ventricle in multiple patient-specific geometries. This method is applied as a post-processing step to flow fields representative of data collected from 4D-flow Magnetic Resonance Imaging (MRI) and color-Doppler ultrasound.

While disease states have been linked to flow structures inside the left ventricle [12, 13, 14, 20, 22, 74, 75, 76], the use of quantitative measures of blood flow in the clinic are limited by blood flow imaging technology. To measure blood flow in the clinic, the most common tools are color-Doppler ultrasound and 4D-flow MRI. In general, in the clinic, color-Doppler ultrasound provides a single component of velocity parallel to the ultrasound beam on a 2D plane, although recent developments in research have expanded it to multiple components in multiple planes [77, 78]. 4D-flow MRI can be used to measure and evaluate a full 3D blood flow field in a 3D domain, but 4D-flow MRI data is noisy, and it does not satisfy physical constraints, such as the divergence-free condition, complicating further analysis of the flow field [2]. Both types of measured flow fields are noisy and have low spatial and temporal resolution, and would benefit from improved filtering and reconstruction methods.

In order to improve the quality of the data collected from 4D-flow MRI, many techniques have been developed to address different sources of error and make 4D-flow MRI easier to use in the data acquisition stages. One of the main roadblocks to 4D-flow MRI being widely used in the clinic is long acquisition times, which are typically on the order of 5 to 25 minutes [2]. In order to address this, many methods have been developed to decrease acquisition time, even though this sometimes comes at the cost of the quality of flow data [79, 80, 81, 82]. Other techniques have been developed that focus on tuning acquisition parameters to improve the quality of the acquired data [54, 55, 73].

Other methods incorporate improvements in the post-processing stages by using information about physiological conditions of flow to filter 4D-flow MRI data. In particular,

the concept that blood is incompressible is enforced by introducing a divergence-free condition to the measured flow field. Song et al. use a projection operation into the space of divergence-free vector fields to reduce noise [65]. Busch et al. combine normalized convolution and divergence-free radial basis functions to de-noise 4D-flow MRI data [66]. Santelli et al. combined divergence-free wavelets and the finite difference method to iteratively reconstruct the flow field by regularizing phase and magnitude in alternating iterations [67]. Schiavazzi et al. use a divergence-free linear filter to de-noise three-dimensional velocity fields [63]. These methods all enforce a divergence-free condition, but in another approach, Ong et al. enforces a 'soft' divergence-free condition using wavelet transforms to account for inaccurate boundary conditions [69]. Ong et al. argue that due to the resolution of the data, introducing a strict divergence-free condition results in unwanted boundary affects near the edges if the segmentation of the domain is imperfect. Tafti et al. [83] and Bostan et al. [84] use variational reconstruction algorithms that minimize a cost function that includes the difference between the reconstructed and measured flow field and other measures that take into account physical properties of flow. All of these methods have been shown to reduce noise in different cases and they have also been evaluated by other groups. Sereno et al. [85] recommend the methods by Song [65] and Ong [69] due to their quick computation times. Loecher et al. [86] also recommends Song's algorithm [65] over Busch's algorithm [66] when added to PC-VIPR 4D-flow data.

As evidenced by the range of these methods, the incompressibility of blood flow is an important characteristic, but there are other aspects of blood flow that are also important to capture in the post-processing stages. For example, accurate boundary conditions are very important for further analysis of flow fields. In particle-tracking analyses, errors at the wall will cause particles to flow through the wall, and clinically valuable measures such as wall shear stress require physiological boundary conditions. Due to the importance of further analysis of the flow fields for gathering diagnostic information, our method was designed to enforce a strict divergence-free condition, in addition to satisfying specified boundary conditions.

In this chapter, we use the open-boundary modal analysis method described in Chapter 4 to de-noise velocity fields in the left ventricle such that the resulting field is divergence-free and satisfies appropriate boundary conditions. This method calculates a set of modes, based on the geometry of the domain and specified boundary conditions, and then projects the data onto these modes to produce a new velocity field. The modes are calculated by solving for velocity fields that minimize velocity gradient, and there are two types of modes: interior and boundary. Here, the boundary modes are modified for the specific left ventricle application. Velocity gradient is related to viscous dissipation, so the method seeks velocity fields that minimize energy losses through viscous dissipation. In the heart, the natural vortex formation has been hypothesized to minimize kinetic energy dissipation [12, 40], and healthy patients have been shown to have lower energy losses in the heart, measured as a sum of velocity gradients, compared to diseased patients [14, 49].

In order to test the method using a dataset where the 'ground truth' is available, data from computational fluid dynamics simulations were used. Noise was added to these data

sets to represent imaging data. Reconstructions were performed on the original CFD data and the noisy versions of the data. In addition, the reconstruction was tested on very sparse versions of the data sets and data sets where only one or two components of velocity were available.

5.2 Methods

A velocity field is reconstructed by projecting the measured velocity data onto a limited number of velocity modes, where the modes are based on the instantaneous geometry of the domain. The method is described in detail in Chapter 4. In this chapter, the boundary modes are modified for the left ventricle application. This is described in section 5.2.1. Multiple different data sets from multiple patients are tested, with varying amounts of noise and sparsity. These are described in section 5.2.3. Figure 5.1 shows an overview of the velocity field reconstruction process.

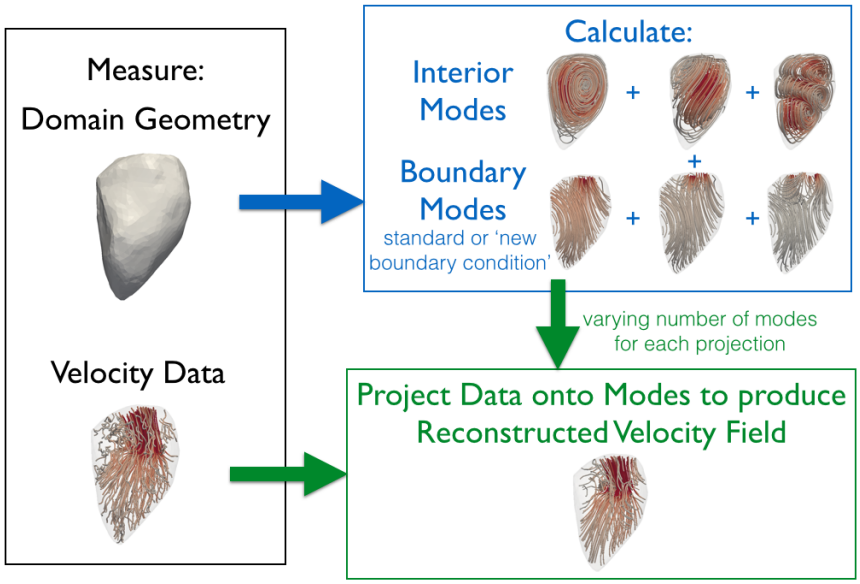

Figure 5.1: Overview of the modal analysis reconstruction process, from measuring the data to producing the new, reconstructed velocity field.

Examples of interior modes and boundary modes for one of the left ventricule geometries used in this Chapter are shown in Figures 5.2 and 5.3 respectively.

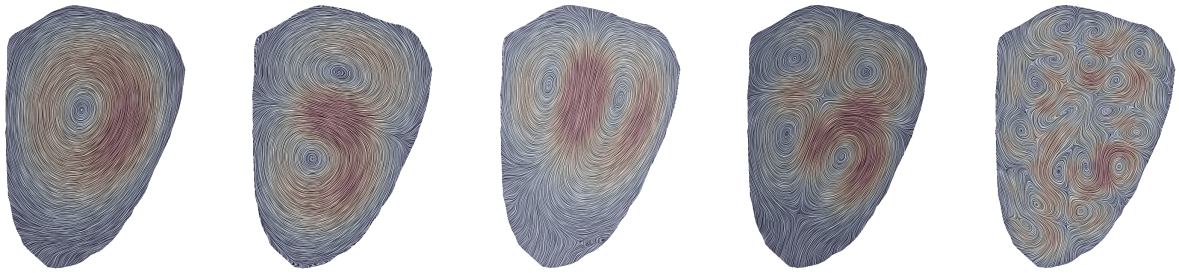

Figure 5.2: Examples of five different interior modes for LV2 at the 13^{th} time step, during diastole. The color indicates velocity magnitude with red high and blue low. The lines are a line integral convolution of the velocity field, where the lines are indicative of flow direction.

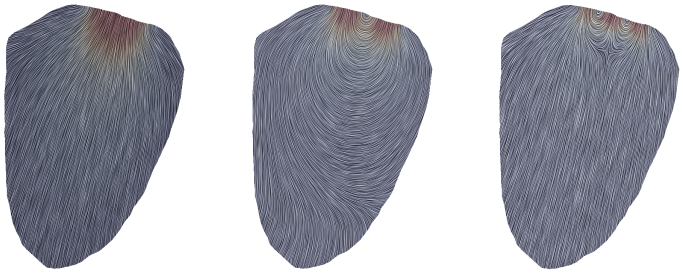

Figure 5.3: Examples of three different boundary modes for LV2 at the 13^{th} time step, during diastole. The color indicates velocity magnitude and the lines are a line integral convolution of the velocity field, where the lines are indicative of flow direction. The mitral valve, which is at the top right in these snapshots, is open. The velocity changes over the mitral valve between the modes, whereas the velocity patterns on the rest of the walls stay the same between modes, although the magnitude may vary.

5.2.1 Boundary Modes for the Left Ventricle

The boundary modes are the modes that allow flow through the boundary. There are two main types of boundaries, one where the velocity is known exactly, known as a 'closed boundary', and another where the velocity data in those areas is noisy or unknown, known as an 'open boundary'. It is possible to have more than one of each type of boundary.

Each boundary mode is associated with a single boundary condition. Multiple boundary modes come from multiple boundary conditions. If the velocity field on the boundary is known exactly, (i.e. is entirely a 'closed boundary'), then only a single boundary mode is needed. This boundary mode will have a boundary condition equal to the known velocity information. For velocity data in the left ventricle, the flow on the boundary is noisy, and therefore a set of boundary modes is needed in order to eliminate the noise.

Additionally, the boundary modes can be modified to include different types of boundary conditions on different parts of the boundary. This can be used to leverage information about the physics of the flow on and near the boundaries. Therefore, we tested two types of boundary conditions to better understand the extent to which this information would

be valuable in the reconstruction. The first type uses information about wall movement to inform the boundary conditions, and the second type uses blood velocity data at the wall to inform the boundary conditions.

Boundary Modes - Incorporating Wall Motion The first type of boundary mode uses information about movement of the wall to determine velocity boundary conditions at the walls. This is based on the assumption that because there is no flow through the walls and there is a no-slip condition on the walls, that the velocity of the blood at the walls will be proportional to the velocity of the wall. To implement this, the domain is split into two parts. The first part contains the walls and the closed valve, where the boundary condition is set based on the motion at the wall. All of the modes will have the same boundary condition on this part of the boundary. The second part contains the valve that is open during that part of the cycle. The set of modes comes from a set of boundary conditions on this part of the boundary.

In order to determine the velocity of the walls, the change in location of the walls between time steps is measured. Tracking this change in location is itself its own research problem [87]. If the motion of the wall was available, we used this information. When this information was unavailable, we used the method described by Myronenko and Song with code they have made openly available [88] to determine the wall motion.

For the second part of the boundary, with the (single) open valve, the flow through the valve is assumed to be perpendicular to the surface. A set of scalar modes, described below in 'Solving Scalar Modes on a Surface', is calculated on the valve. For each scalar mode, at each point on the surface, the velocity is set to be normal to the surface with the magnitude of the scalar mode at that point.

For each mode, there is a unique boundary condition on the valve, and a single boundary condition on the rest of the surface. In order to ensure conservation of mass, the magnitude of the flow through the valve is adjusted to be equal and opposite the flow through the rest of the surface. Each of these combined boundary conditions results in a single boundary mode.

Boundary Modes - Incorporating Wall Velocity Data The second type of boundary mode is based on the velocity data at the wall, in order to address the fact that our ability to calculate wall motion is not perfect. Again, the boundary is split into two different parts, the open valve and the rest of the wall. The boundary condition on the valve is calculated the same was as it is in the previous type of boundary mode, but the conditions on the rest of the walls are treated differently. Instead of the boundary conditions based on wall motion, this time the velocity data at the wall is used.

However, the data at the wall is noisy, so it is not used as-is. Instead, a type of modal analysis is used to smooth the velocity data at the wall. First, a set of scalar modes on the wall are calculated, in the same way as for the valve, as described below in 'Solving Scalar Modes on a Surface'. Then, each component of velocity on the wall (v_x, v_y, and v_z)

is projected onto the set of modes, resulting in a single, de-noised, velocity field at the wall. To ensure conservation of mass, for each scalar mode in the valve, the magnitude of the flow through the valve is set to balance the flow through the walls.

Solving Scalar Modes on a Surface For 'open boundary' conditions, where the velocity information is not known exactly, a series of scalar modes is developed for the boundary conditions. This method is similar to the interior modes solved inside the domain, but instead we are interested in a surface, and we are solving for a scalar field, not a velocity field. The i^{th} scalar mode, g_i, is the result of the Laplace eigenvalue problem, where g_i is set to 0 on the edge of the surface ($\delta\Omega$) and g_i is a scalar field on the given surface:

$$\begin{aligned} \Delta g_i &= -\lambda_i^g g_i \\ g_i &= 0 \text{ on } \delta\Omega. \end{aligned} \tag{5.1}$$

5.2.2 Projection of Data onto Modes

In almost all cases, the projection of the data onto the modes is performed by a least squares optimization to minimize the difference between the data and the new reconstructed velocity field, as described in Section 4.2.3. The least squares algorithm determines the coefficients, α, for each mode that describe the contribution of that mode to the new, reconstructed velocity field. The form for the reconstructed velocity field, U_r, is the same as before:

$$\mathbf{U}_r = \sum_{i=1}^{N_I} \alpha_i^I \boldsymbol{u}_i^I + \sum_{i=1}^{N_b} \alpha_i^b \boldsymbol{u}_i^b = \sum_{i=1}^{N} \alpha_i \boldsymbol{u}_i \tag{5.2}$$

where $\mathbf{u}_i^I$ are interior modes, $\mathbf{u}_i^b$ are boundary modes, N_I is the number of interior modes available, N_b is the number of boundary modes available, and $N = N_I + N_b$.

In the case where the reconstruction was performed from only a single component of velocity, an additional constraint was included where the least squares algorithm was modified to include ridge regression. In the ridge regression formulation, the coefficients, α, are determined by solving this modified least squares problem:

$$\begin{aligned} \min_{\alpha} \|\mathbf{U}_{true} - \mathbf{U}_r\|_2^2 &= \min_{\alpha} \|\mathbf{U}_{true} - (\sum_{i=1}^{N_I} \alpha_i^I \boldsymbol{u}_i^I + \sum_{i=1}^{N_b} \alpha_i^b \boldsymbol{u}_i^b)\|_2^2 + \gamma \| \sum_{i=1}^{N_I} \alpha_i^I \|_2^2 \\ &= \min_{\boldsymbol{\alpha}} \|\mathbf{U}_{true} - \mathbf{A}\boldsymbol{\alpha}\|_2^2 + \gamma \|\boldsymbol{\alpha}_i\|_2^2 \end{aligned}$$

where each column of $\mathbf{A}$ contains information for one mode, $\boldsymbol{\alpha}_i$ is a vector containing the interior mode coefficients, and γ is an experimentally determined parameter, and in this case was set equal to 10^6.

Table 5.1 describes the parameters available for modification in the reconstruction algorithm.

Parameter	Forms	(Details)/[Levels of Parameter]
Interior Modes		[Any number of modes can be used, up to the number calculated.]
Boundary Modes	Original	(based on wall movement)/[Any number of modes can be used, up to the number calculated.]
	New	(based on flow data)/[Any number of modes can be used, up to the number calculated.]
Type of Projection		[Least Squares, Ridge Regression]

Table 5.1: Summary of parameters that can be adjusted by the user in the reconstruction. In the clinic, these parameters will be adjustable by the user.

5.2.3 Application to Data

The reconstruction was performed on multiple data sets, using a variety of noise levels and different levels of sparsity of the data.

CFD Data from Linköping University

Results from computational fluid dynamics (CFD) simulations performed at Linköping University were used to test the method. CFD provides all three components of velocity in a three-dimensional domain. Unlike image data, the results of a simulation satisfy the divergence-free condition and also have a much higher resolution than images. The simulations are a result of a fluid dynamics simulation where the geometry of the heart was collected from Computed Tomography (CT) images at Linköping University. The simulations were performed by Jonas Lantz and Tino Ebbers. Three different data sets were used, where each is a left ventricle from a different patient, and are referred to as LV1, LV2, and LV3. A snapshot of LV1 can be seen in Figure 5.4. For this project, the results of the simulation were down-sampled to represent a 4D-flow MRI acquisition, and then different levels of noise were added to the data.

Noisy Data

Two types of noise were considered to represent different types of imaging data. In the first type, random noise was added directly to the velocity field. Gaussian noise with a zero average and standard deviation of 0.1%, 1%, 10%, 20% and 50% of the maximum velocity component was added to each component of the velocity, resulting in five different velocity fields that could be input to the algorithm for each data set. In the second, 'MRI type', noise, a signal was calculated using the five-point balanced flow-encoding method described by Johnson and Markl, noise was added to the signal with varying magnitudes, and then the velocity fields were re-calculated from the signal [69, 73].

Sparse and Incomplete Data

The ability to reconstruct from sparse and incomplete data sets has applications in multiple types of medical imaging. Here, we perform the velocity reconstruction using data from a reduced number of points in the domain, and also using only one or two components of velocity. In all types of reconstructions, the modes are calculated on the original meshes that contain the entire domain. The projection of the data onto the modes is modified to only include the limited velocity information. For the sparse data sets, or the reduced number of data points, a specified percentage of the data points are excluded from the projection. For limited components of velocity, all data points are available but only the specified components of velocity are used in the projection.

The different possible inputs to the method are described in Table 5.2 and example input velocity fields are shown in Figure 5.4.

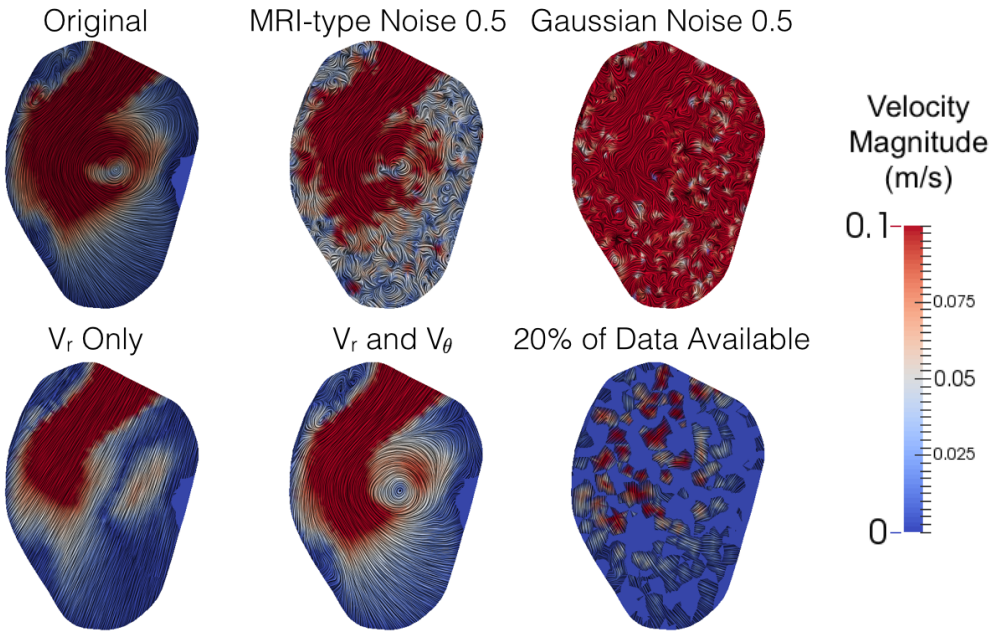

Figure 5.4: Screenshots of examples of velocity fields that are inputs to the reconstruction algorithm. Each screenshot is a slice of the left ventricle during filling. The color represents the velocity magnitudes and the lines are a line integral convolution of the velocity field.

5.2.4 Reconstruction Summary

In order to test the abilities of the modal reconstruction algorithm, a variety of different types of velocity fields are reconstructed using varying numbers of modes, as described above. The general process, from measuring the data to a new, reconstructed velocity field is shown in Figure 5.1. This process is executed for all data sets at each time point. There are

Parameter	Forms	(Details)/[Levels of Parameter]
Noise Type and Level	None	
	Gaussian	[0.01, 0.1, 0.2, 0.5]
	MRI-type	[0.01, 0.1, 0.2, 0.5]
Sparsity		[All data available, 50% available, 20% available]
Incomplete		[All 3 components of velocity available, 2 components available, 1 component available]

Table 5.2: Summary of parameters describing the input data for the reconstruction. In the clinic, these would not be adjustable. They are adjusted here to test the efficacy of the method and explore different possibilities in the clinic.

multiple parameters used in the reconstruction that can be modified by the user to achieve a better velocity field, including the number of modes used in the reconstruction and the type of projection. These parameters are described in Table 5.1. A variety of different parameter levels are explored here. For all test cases for a specific time point and geometry, the interior modes are the same. For all cases except the 'new boundary condition', the boundary conditions are as described in Section 5.2.1. For the 'new boundary condition', the boundary modes are modified as described in Section 5.2.1. However, the number of modes made available for the reconstruction was varied for each reconstruction to explore how the number of modes affects the reconstruction.

To test the robustness of the method, a variety of different types of velocity data are used as inputs into the method. They are outlined in Table 5.2. These alternative versions of the fields replace the 'velocity data' (Figure 5.1) but the modes are unaffected. The reconstructed field will be dictated by this input velocity field. The original velocity data with no noise is used to test the ability of the method to capture a typical velocity field in the heart.

5.2.5 Error Calculation

To evaluate the quality of each reconstruction, the reconstructed velocity field was compared to the true velocity field. The error of a velocity field at a specific time point was calculated

$$E_{l2} = \frac{\sqrt{\sum_{i=1}^{3}\sum_{j=1}^{n}\left(v_{i,true}^{j} - v_{i,reconstructed}^{j}\right)^2}}{\sqrt{\sum_{i=1}^{3}\sum_{j=1}^{n}(v_{i,true}^{j})^2}} \tag{5.3}$$

where v_i^j is i^{th} component of velocity at the j^{th} point, and n is the number of points in the domain.

The error was calculated for both the new reconstructed velocity field, and the velocity field that is being reconstructed (i.e. the 'noisy' velocity fields). The 'true' velocity field has an error of 0, and all other velocity fields ('noisy' and reconstructed) have a positive error. In the following section, the error of the reconstructed velocity field is compared to the error of the velocity field it was reconstructed from.

5.3 Results

For each data set, multiple reconstructions were performed. First, noise was added to the original data, and then multiple different types of reconstructions were performed, each with a varying number of modes used. Between 50 and 300 interior modes were used, and between 10 and 42 boundary modes were used. If it is not specified, the maximum number of boundary modes (42) were used in the reconstruction.

5.3.1 Application to Noisy Data

Overall, the observed trends aligned with what was seen in Chapter 4. In general, increasing the numbers of modes used for the reconstruction decreased the error of the reconstructed velocity field (Figure 5.5). This is expected because higher modes have more complex flow structures, so increasing the number of modes used in the reconstruction increases the complexity of flow features that can be captured. However, when the error of the 'noisy' field (without reconstruction) was high initially, adding more modes did not necessarily decrease the error of the reconstructed field. In these cases, the higher modes capture the noise rather than eliminating noise. Although increasing the numbers of modes did not always decrease error in these cases, all reconstructions with all numbers of modes had much lower error than the original noisy velocity field. For low noise levels (including the 'Original' velocity field with no noise added), the reconstructions had higher errors than the original field. This is expected because there were not enough modes available in the reconstruction to perfectly capture all the flow features. As the number of modes used for these reconstructions increased, the error accordingly decreased. Overall, the error of the reconstructed field was very consistent, regardless of the noise added to the velocity field. Figure 5.5 shows the error of the reconstructed velocity fields plotted against the error of the fields being reconstructed for two time points for LV2. The patterns discussed can be seen for these two time points and were consistent across all of the datasets for all time points.

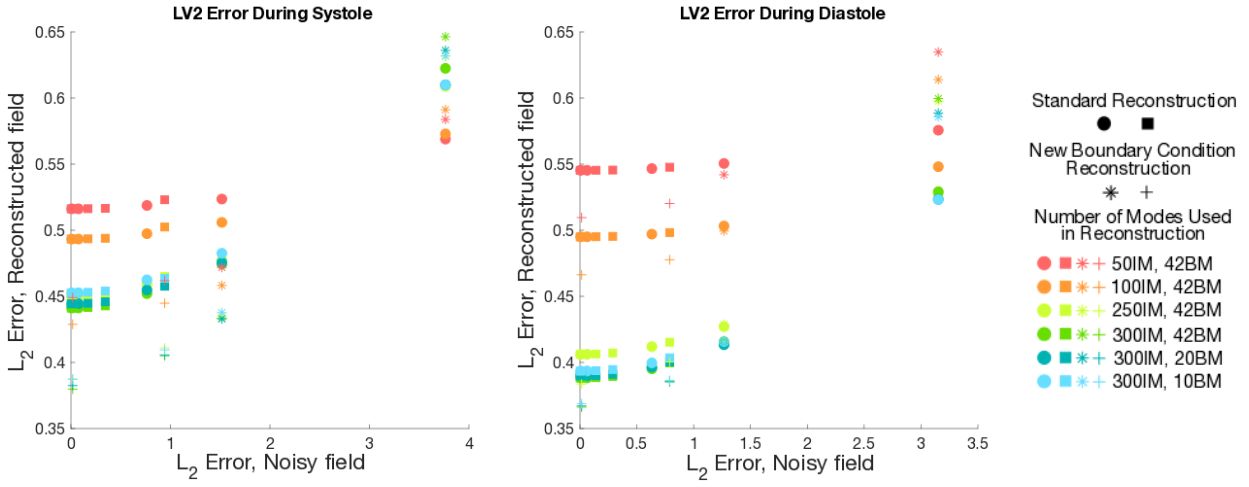

Figure 5.5: Error of reconstructed field for LV2 at different time points. The x-axis is the error of the velocity field that is being reconstructed, and the y-axis is the error of the reconstructed velocity field. For example, '0' on the x-axis corresponds to the 'Original' velocity field, and other points further to the right indicate velocity fields with noise added. The solid dots show the standard reconstruction type and the the stars show the reconstruction with the new boundary condition. The different colors represent different numbers of interior modes (IM) and boundary modes (BM) used in the reconstruction.

For the CFD data, the influence of the interior modes was observed to be much larger than that of the boundary modes. This is evident because changing the number of interior modes had a larger effect on the error for almost all cases (Figure 5.5). The biggest exception was during systole for LV1. Upon further examination, it could be seen that the flow structures inside the ventricle during systole were very small compared to the flow exiting through the aortic valve. In the other example ventricles, LV2 and LV3, there appear to be non-negligible flow structures during systole, meaning that the interior modes are more important than in LV1 during systole.

In addition, the second type of boundary mode, which uses the measured velocity at the wall to determine boundary conditions, decreased the errors in the reconstructions compared to the original boundary mode, which uses wall movement information to determine boundary conditions (Figures 5.5 and 5.6). However, the amount that the second type of boundary mode improved the error varied with the different time points and different cases. These discrepancies are likely caused by the fact that the algorithm to track wall changes in time performed better at some time points than others. Flow fields at a few representative time points are shown in Figures 5.8 and 5.9.

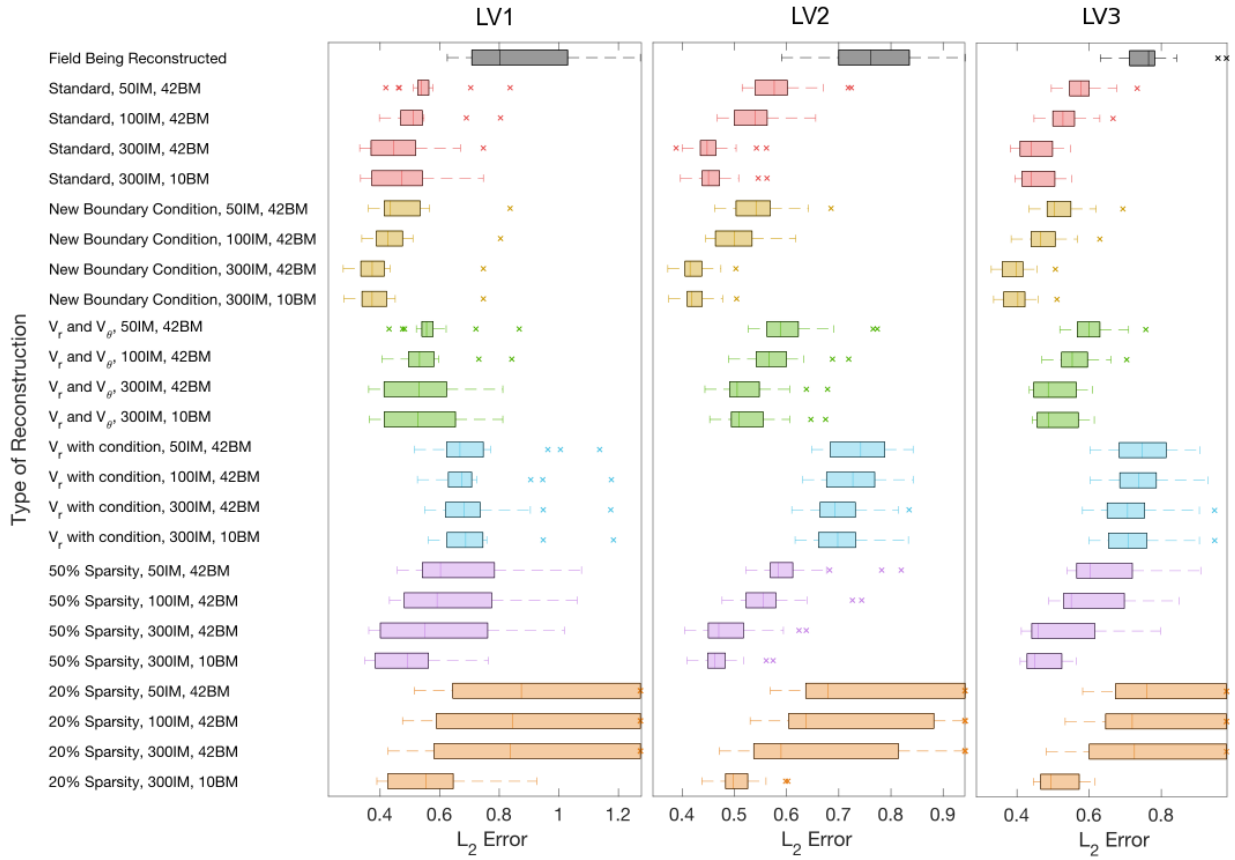

Figure 5.6: Error of reconstructed fields at multiple time points for the different types of reconstructions (colors) with varying number of modes used for the reconstruction when reconstructed from a noisy velocity field with MRI-type noise.

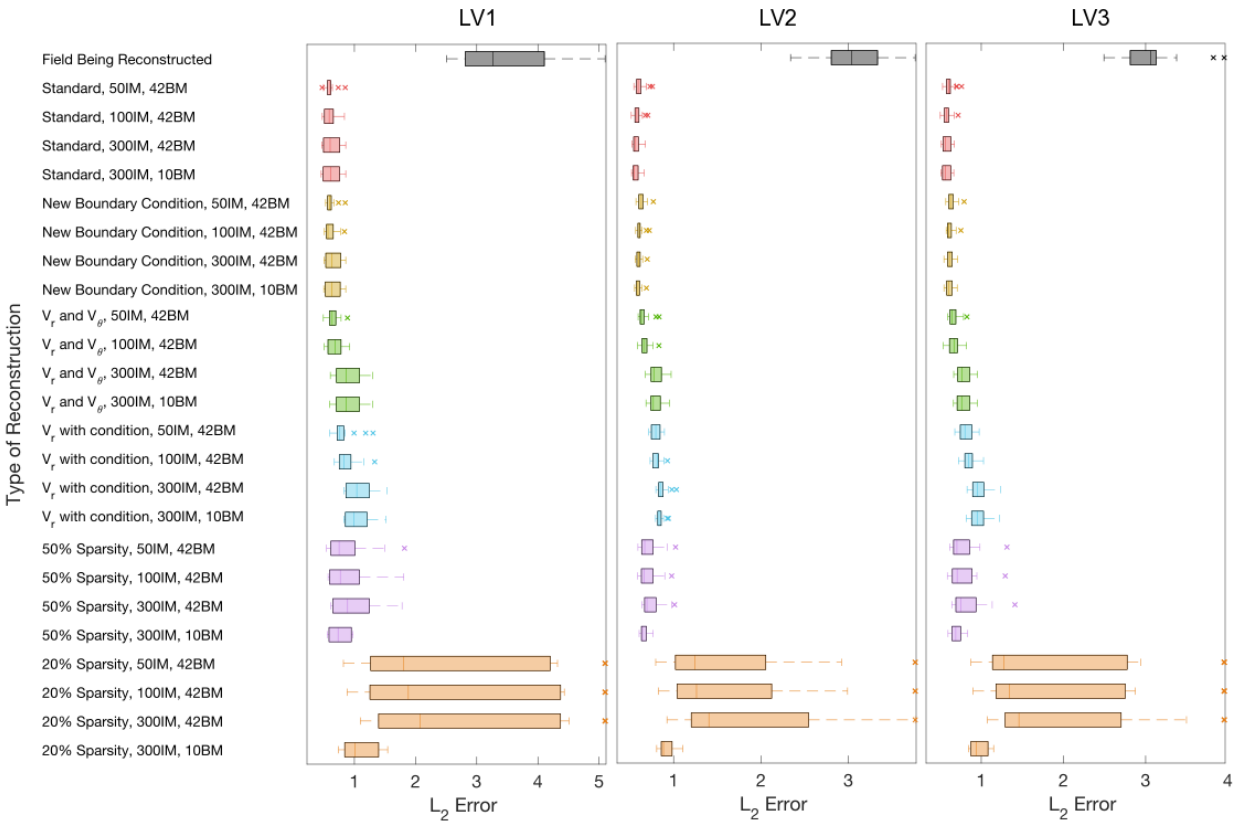

Figure 5.7: Error of reconstructed fields at multiple time points for the different types of reconstructions (colors) with varying number of modes used for the reconstruction when reconstructed from a noisy velocity field with regular noise.

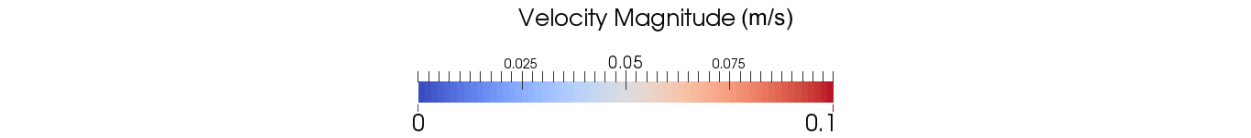

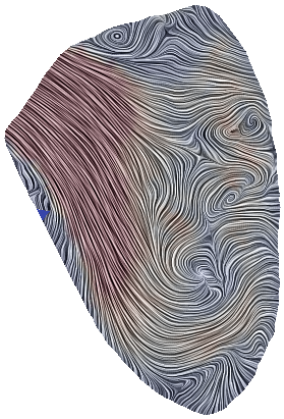

(a) True flow field.

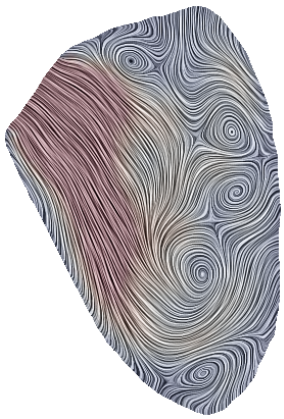

(b) Flow field reconstructed from the true flow field with 300 interior modes and 42 boundary modes.

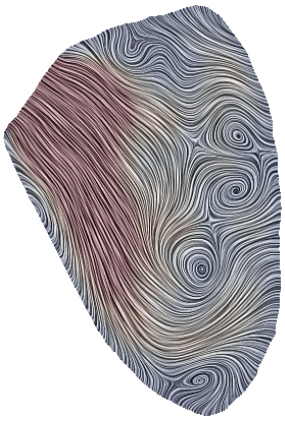

(c) Flow field reconstructed from the true flow field with 300 interior modes and 42 of the new type of boundary modes.

(d) Flow field reconstructed using only two components of velocity from the true flow field with 300 interior modes and 42 boundary modes.

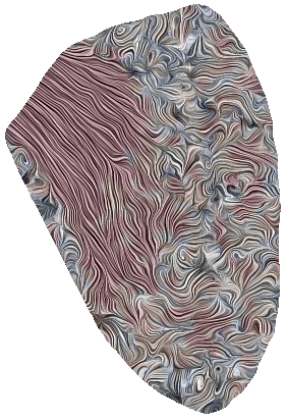

(e) Flow field with MRI-type artificial noise added.

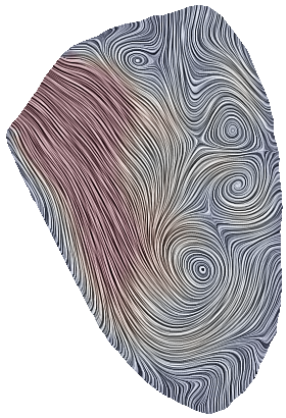

(f) Flow field reconstructed from the noisy flow field with 300 interior modes and 42 boundary modes.

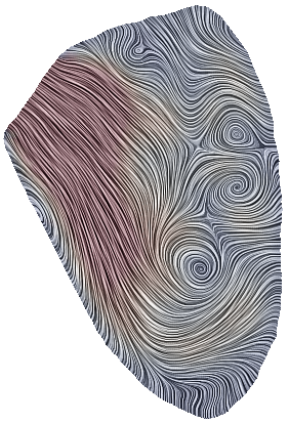

(g) Flow field reconstructed from the noisy flow field with 300 interior modes and 42 of the new type of boundary modes.

(h) Flow field reconstructed using only two components of velocity from the noisy flow field with 300 interior modes and 42 boundary modes.

Figure 5.8: Snapshots of original and reconstructed flow fields of LV2 during systole. The color indicates velocity magnitude and the lines are a line integral convolution of the velocity field, where the lines are indicative of flow direction.

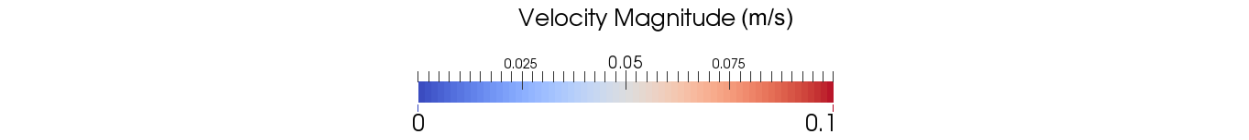

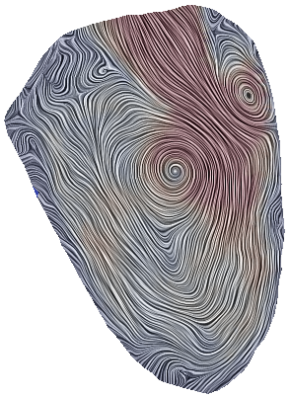

(a) True flow field.

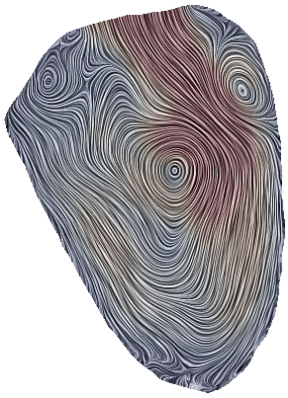

(b) Flow field reconstructed from the true flow field with 300 interior modes and 42 boundary modes.

(c) Flow field reconstructed from the true flow field with 300 interior modes and 42 of the new type of boundary modes.

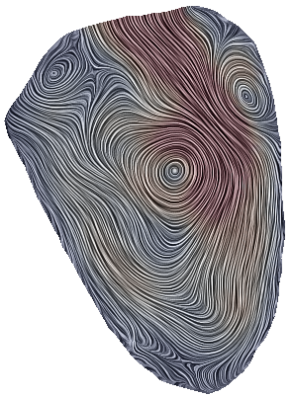

(d) Flow field reconstructed using only two components of velocity from the true flow field with 300 interior modes and 42 boundary modes.

(e) Flow field with MRI-type artificial noise added.

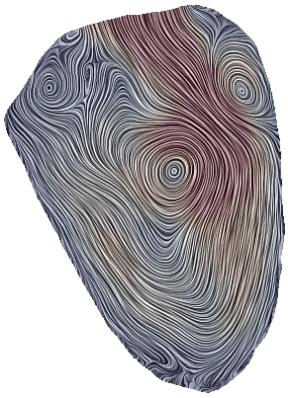

(f) Flow field reconstructed from the noisy flow field with 300 interior modes and 42 boundary modes.

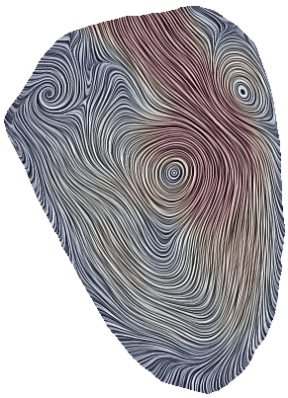

(g) Flow field reconstructed from the noisy flow field with 300 interior modes and 42 of the new type of boundary modes.

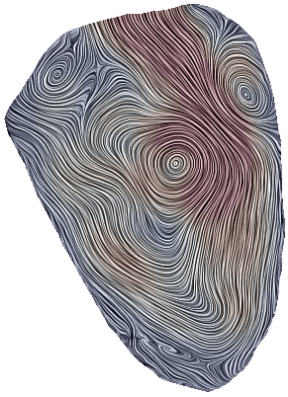

(h) LV2: Snapshot of flow field in LV2 at t/T = 14/20 reconstructed using only two components of velocity from the noisy flow field with 300 interior modes and 42 boundary modes.

Figure 5.9: Snapshots of flow fields in original and reconstructed flow fields of LV2 during diastole. The color indicates velocity magnitude and the lines are a line integral convolution of the velocity field, where the lines are indicative of flow direction.

5.3.2 Application to Data - Sparse and Incomplete Data

Sparse and incomplete results were only evaluated for the original type of boundary modes. The sparse results refer to reconstructions where only 50 or 20% of the data was available to the reconstruction algorithm. The incomplete results refer to reconstructions where only one or two components of velocity are available.

As expected, making less data available to the reconstruction algorithm increased the errors in the results of the reconstructions. However, the error of the reconstructions with only half the data were similar to the reconstructions with the full data. Once the data was reduced to 20%, the errors increased more significantly (the purple and orange bars in Figures 5.6-5.7). In addition, the errors for the reconstructions with sparse data were higher during systole than diastole. During systole, the majority of the flow is flow exiting the ventricle, whereas during diastole, there are more complex vortices forming inside the ventricle. Because the algorithm emphasizes internal flow structures, as the amount of data available is reduced, the algorithm has trouble capturing the more direct flow seen in systole.

For all cases, reconstructions using only a single, radial, component of velocity had very poor reconstructions with errors that were orders of magnitude larger than when reconstructed with all three components of velocity. The magnitude of the reconstructed velocity field in these cases was orders of magnitude larger than the true velocity field. To address this, we modified the projection of the data onto the modes by introducing a ridge regression to penalize the L_2 norm of the coefficients of the modes, which is equivalent to penalizing large magnitudes of the reconstructed velocity field. The modified projection, denoted as 'V_r with condition', significantly reduced the error in the reconstructed velocity fields from only a single, radial component of velocity (the blue bars in Figures 5.6-5.7). These errors were still higher than reconstruction with all three components of velocity, but were now on the same order of magnitude.

Reconstructions performed from only two available components of velocity, the radial and azimuthal components, performed comparatively well to the original reconstruction method (the green bars in Figures 5.6-5.7). For example, the errors for a reconstruction from two components of velocity with 200 modes was frequently lower than the errors for a reconstruction from all three components of velocity with 100 modes. This is expected behavior because for a divergence-free flow field, if two components of velocity are known, the third component of velocity could be calculated from the divergence-free condition.

5.4 Discussion

The geometric modal analysis method was effective at reducing the noise in flow fields in the left ventricle, and followed similar patterns to those seen in other example velocity fields in Chapter 4. When the velocity field had high levels of noise, geometric modal analysis was able to significantly decrease the noise in the velocity field. By taking advantage of the knowledge of the geometry of the left ventricle, this method is very robust to noise and would likely

be effective for other noisy internal flow fields. For velocity fields that had no noise or low levels of noise initially, the reconstructed velocity field had higher errors than the field being reconstructed when compared to the true velocity field. In these cases with low levels of noise initially, the reconstruction was not able to capture all of the flow features because a limited number of modes are available. The noise levels are low to begin with, so with flow features missing, the error in the reconstructed velocity field is larger than that of the field being reconstructed. If more modes were available, then we expect that the reconstruction would improve. However, the number of modes available is currently limited by the computational complexity of the problem. Moving forward, we are studying more efficient ways to solve for modes that would enable us to use more modes in our reconstruction and decrease the error, especially when we start with low amounts of error in the velocity field.

In addition, other expected trends and those seen in Chapter 4 were observed in the reconstructions. For the lower levels of initial noise, increasing the number of modes in the reconstruction decreased the error because the higher modes were able to capture the flow structures that the lower modes could not capture. At higher levels of initial noise, increasing the number of modes in the reconstruction increased the error because the higher modes began to capture the noise in the data. For MRI and ultrasound data, estimates of the amount of noise in the data are available, and the number of modes used in the reconstruction could be adjusted based on those noise levels.

In addition to being robust to high noise levels, we saw that geometric modal analysis also performed well with incomplete information. When only half of the data points were made available to the algorithm, the reconstructions were still able to reduce the overall error. In addition, when only two components of velocity were made available, the method was able to give a good reconstruction. This makes sense in a 3D, divergence-free flow field because in an error-free field, if two components of velocity are known, then the divergence-free condition can be used to calculate the third component of velocity. This is promising for some forms of color-Doppler ultrasound data where two components of velocity are available. When only a single component of velocity is available, which is the case for the majority of color-Doppler ultrasound, the original form of the method has trouble reconstructing the velocity field. However, when the least squares projection algorithm is modified to penalize the L_2 norm of the coefficients, a much better result is achieved. While still not as good as when all components of velocity are known or when only 50% of the data but all three components are available, this result is still promising for the analysis of flow from color-Doppler ultrasound data in the clinic.

We saw that there is room for improvement in the quality of reconstructed velocity fields in modifications of the boundary conditions and boundary modes. Changing the way the boundary modes were calculated did much more to decrease the error in the reconstructed velocity fields than increasing the number of boundary modes did, which could happen for a few reasons. One reason is that the new boundary modes are derived from the available flow at the boundary, and our measure of error is calculated with the ground truth being the known velocity at the boundary. In comparison, the original boundary modes are calculated by measuring the change in the wall position. We would expect the method that uses

velocity data at the wall to have lower errors because we are using simulation data, so even with noise added, the velocity data at the boundary is likely to be a better representation of the actual velocity at the wall than the wall motion that is calculated from an algorithm. When applying the method to measured data, this comes down to a discussion of which type of data is more trustworthy, the flow data or the wall boundary and motion. With our data, the wall data is more trustworthy because we are considering the velocity field from the simulation to be the 'true' data. With actual data the answer is not as clear and depends on the specific scenario and data measurement techniques used.

For future work, one may consider a few adjustments to the method. Two potential areas of improvement, as discussed above, are altering the boundary conditions and the projection of the data onto the modes. We saw that with only one component of velocity, introducing ridge regression to the projection of the data onto the modes provided significant improvement in the reconstruction. It is expected that other modifications to the projection method may provide similar improvements. For example, between two time steps, the geometry and many of the flow structures are similar, but the noise is not. Because the geometry is similar, it is expected that the modes will be very similar between two time points as well. It is possible to penalize changes in contributions of modes between adjacent time points to improve the reconstruction algorithm.

Another important component of this work is evaluating the success of this method based on diagnostic measures rather than on error in the velocity field. Ultimately, if diagnostic information can be gathered from the resulting reconstructed velocity fields even if the reconstruction does not perfectly match the true data, then that is more important in the clinic than a true reconstruction of the velocity field. In future work, one could focus on examining the flow in ways that inform about the health of the patient. This could be done by evaluating the reconstructed field based on its ability to capture structures and the quality of the flow field using Lagrangian Coherent Structures or by using bulk flow measurements such as kinetic energy and viscous dissipation rates. Because this method was successful in reducing the noise in noisy velocity fields in the left ventricle, it is expected that the method should also be successful in identifying diagnostic information in velocity fields in the left ventricle.

In Chapter 4 we saw that the geometric modal analysis method was a promising tool for reducing noise in internal flows, and in this chapter we saw that the geometric modal analysis method is a promising tool for reducing noise in velocity fields in the left ventricle. Although there is room for improvement in multiple aspects of the method, we saw that the method was robust to noise and provided accurate reconstructions for sparse datasets. Future work can continue to explore this method as a tool for de-noising and reconstructing velocity fields in the left ventricle in healthy and diseased states.

Chapter 6

Concluding Remarks

6.1 Summary

This dissertation sought to develop computational tools that will improve our ability to understand blood flow in the left ventricle and how it relates to disease progression. To this end we developed and studied reduced dimensional estimates of kinetic energy and viscous dissipation rate in the left ventricle that can be measured using color-Doppler ultrasound data and we introduced and evaluated a modal analysis technique to de-noise and reconstruct 3D flow fields.

In Chapter 1 we reviewed background and motivation for reconstruction and analysis of 3D flow fields in the left ventricle. In Chapter 2 we introduced and evaluated two methods to reconstruct the second, in-plane component of velocity for color-Doppler ultrasound that do not rely on the divergence-free assumption. Although this assumption has been shown to be over-simplified [30], methods that use this assumption are still being used to evaluate blood flow quality [20, 28]. The alternative methods without the divergence-free assumption investigated here did not offer an improvement over methods that used the divergence-free assumption. When evaluated based on accuracy of the reconstructed component of velocity, all types of the reconstructions were not much better than assuming the second component of velocity was zero everywhere. However, the accuracy of the second component of velocity is not what is most important. What is important is if the velocity field can tell us diagnostic information. Methods that use the divergence-free assumption have been used to show differences in blood flow patterns in healthy and diseased patients and therefore the methods continue to be used to research flow in the left ventricle.

The results of Chapter 2 motivated two different directions of research. The first was to investigate if diagnostic tools could be calculated from only a single component of velocity from color-Doppler ultrasound data, thereby avoiding having to make assumptions in order to calculate the second component of velocity. This line of thought was pursued in Chapter 3. The second direction was to develop a reconstruction method for a 3D domain rather than a single plane because ultrasound is now able to measure data in a 3D domain. This method was introduced in Chapter 4 and can be used as a de-noising or reconstruction method.

The method was applied to synthetic color-Doppler ultrasound and MRI data from the left ventricle in Chapter 5.

In Chapter 3, reduced dimensional estimates of kinetic energy and viscous dissipation rate were introduced as potential diagnostic tools, measurable from color-Doppler ultrasound data without having to reconstruct a second component of velocity. Using results of computational fluid dynamics simulations of the left ventricle in three different patients, virtual measurements were taken and 1D and 2D estimates were compared to 3D measurements across the entire ventricle. Overall, the 1D estimates were correlated with the 3D measurements. In many cases, the correlations of the 1D estimates were lower than when both components of velocity were available for a 2D estimate, but higher than when a second component of velocity was calculated from the first component for the 2D estimate. This implies that in the clinic, 1D estimates of kinetic energy and viscous dissipation rate could be valuable tools. When examined at lower resolution and with noise added to the velocity field, reduced dimensional estimates of kinetic energy were much more robust than viscous dissipation rate. In addition, reduced dimensional estimates of kinetic energy were actually more strongly correlated than reduced dimensional estimates of viscous dissipation rate with the measured 3D viscous dissipation rate. This finding indicates that while imaging in the clinic is still noisy and has low resolution, using estimates of kinetic energy rather than viscous dissipation rate could give a better prediction of true viscous dissipation rate. Only simulation data was used in this dissertation, so it is worth further investigation into these reduced dimensional estimates using color-Doppler ultrasound data from patient populations.

Chapter 4 was a transition back to reconstruction and de-noising methods, but this time in 3D. An open-boundary modal analysis method was developed for 3D velocity fields. In Chapter 4 this method is described in detail and tested on three example problems. The test problems were the results of simulations so that the reconstructions could be compared to a known velocity field. In open-boundary modal analysis, the modes are calculated directly from the geometry, without any influence from the flow data. The flow data is introduced by projecting the data onto the modes to get a new, reconstructed velocity field. Due to how the method is implemented, it can be applied to a noisy but fully 3D velocity field, such as those from MRI data, or to a sparse velocity field either missing data at certain points or missing some components of velocity, such as those from color-Doppler ultrasound data. The method was shown to be very robust to noise, and to perform well on some sparse data sets, depending on how much and what type of information was available.

In Chapter 5 we applied the open-boundary modal analysis introduced in Chapter 4 to velocity fields from left ventricles. The data used were results of computational fluid dynamics simulations so that the reconstructions could be evaluated against a true, known velocity field. Similar results were seen for the left ventricle as with the example problems, where the method was shown to be very robust to noise and for reconstructions to be dependent on the number of modes used in the reconstruction and the velocity field available. When only one component of velocity was available, similar to color-Doppler ultrasound data, extra penalty terms were required to give adequate results. It is worth continuing to examine extra conditions that could be applied to improve results for color-Doppler ultrasound data.

Recent developments in color-Doppler ultrasound data have made a second component of velocity available [77, 78], and when we started with only two components of velocity, the method was able to give a good reconstruction, which is a promising result. While many methods have been introduced to de-noise 3D velocity fields, this method provides advantages because it results in a divergence-free flow field, satisfies necessary boundary conditions, and can be applied to multiple types of data.

6.2 Future Directions

As this research continues to progress, it is important to remember that the ultimate goal of this work is to improve diagnosis and treatment of heart disease by improving blood flow imaging in the left ventricle. There are many possible directions for continuation of these projects, but ease of implementation and understanding of results are very important factors that help determine if a tool will be successful in the clinic.

For color-Doppler ultrasound based measurements, 1D estimates of diagnostic tools should be pursued, especially in comparison to 2D estimates that are calculated using the divergence-free assumption. Here, we examined reduced dimensional estimates of kinetic energy and viscous dissipation rate, but there are other potential diagnostic measures that could be investigated as well. For example, even with kinetic energy, different studies have examined different versions of kinetic energy, by indexing to stroke volume [37] or ventricular volume [38]. In addition, estimates of vortex location and strength based solely on radial velocity magnitude and gradient of radial velocity could also be developed.

As image processing tools are advancing, the imaging tools themselves are also advancing. Although not yet used in the clinic, developments in color-Doppler ultrasound have enabled 2D measurements, avoiding the need for 2D reconstructions [77, 78]. When these 2D measurement techniques become widely available, the usage of reduced dimensional diagnostic tools would need to be modified for this type of data. As both tools and processing methods continue to progress, it is important to evaluate which tools and methods are accurate, provide useful diagnostic information, and are easily adaptable in the clinic.

Open boundary modal analysis is also a potentially valuable clinical tool that can continue to be developed. Currently, one of the limiting aspects of the method is the number of modes that can be calculated due to the computational complexity of the problem. In the future, testing different solver methods and preconditioners or even modifying the formulation of the problem could lead to a more efficient calculation of the modes, speeding up the process and making the method more clinically viable. Also of importance is a deeper investigation into the optimal number of modes for different problems. Here, we saw that the optimal number of modes depended on the flow field, the amount of data available, and the level of noise of the velocity field. In addition, fitting only a single component of velocity by introducing extra constraints would be a valuable path to pursue because of its potential use with color-Doppler ultrasound data. In this work, fitting only a single component of velocity using traditional least squares led to poor, unusable results. However, introducing a penalty term

on the magnitude of the coefficients of the modes reduced the error significantly, resulting in reconstructed velocity fields that captured many of the flow patterns that were present in the true velocity field. Continued research into methods to further and better constrain the reconstructed velocity field when only a single component of velocity is available could make this method viable for multi-plane color-Doppler ultrasound data, which is currently becoming more widely available in the clinic.

For all parts of the research in this dissertation, an important next step is evaluating the different methods with respect to clinical outcomes. For the most part, the methods were evaluated compared to a 'true' value or velocity field. In the end, we are interested in how these methods can be used to evaluate disease, so it is important to study how the estimates of kinetic energy and viscous dissipation rate and how the reconstructions of the velocity field perform when healthy cases are compared to diseased cases.

It is also important to note that there are a few qualifications for a tool to be adopted into the clinic. It is not necessarily the most complex engineering tool used to solve the most complex problem that qualifies a tool for the clinic. Instead, the tool must be easy to use and easy to understand. For example, Bermejo et al. noted that spectral Doppler-based techniques used to quantify the degree of valvular stenosis were quickly adopted in the clinic due to the fact that they could take measurements non-invasively even though the technique required highly oversimplified fluid dynamics approximations [20].

Regardless of how this field advances, it is important to always consider the balance between complexity and accuracy. Ideally, we would like to have the most accurate results with the highest resolution. However, these tend to come at a high cost. If a simple measurement can tell us diagnostic information, then that is the most valuable information. In summary, while there is much work to be done, this thesis demonstrated we can develop tools to help understand flow that can ultimately be used to improve our understanding of disease and disease progression, leading to improved clinical outcomes.

Appendix A

Minimization of Velocity Gradient

Minimizing the velocity gradient is equivalent to minimizing multiple other quantities.

A.1 Comparison to viscous dissipation

Viscous dissipation is defined:

$$\phi_v = \sum_i \sum_j \frac{2\mu}{\rho} \left[\left(\frac{1}{2} \left(\frac{\partial v_i}{\partial x_j} + \frac{\partial v_j}{\partial x_i} \right) \right)^2 - \frac{1}{3} \left(\frac{\partial v_i}{\partial x_i} \right)^2 \right] \tag{A.1}$$

For incompressible flow, $\frac{\partial v_i}{\partial x_i} = 0$. As a result, we can reduce viscous dissipation to

$$\begin{aligned} \phi_v =& \sum_i \sum_j \frac{\mu}{2\rho} \left[\left(\frac{\partial v_i}{\partial x_j} + \frac{\partial v_j}{\partial x_i} \right)^2 \right] \\ =& \frac{\mu}{\rho} \|\nabla v\|_F^2 + \sum_i \sum_j \frac{\mu}{\rho} \left[\frac{\partial v_i}{\partial x_j} \frac{\partial v_j}{\partial x_i} \right] \end{aligned}$$

We are concerned with the difference between minimizing viscous dissipation and minimizing the velocity gradient, therefore, we are concerned about the function:

$$I = \sum_i \sum_j \frac{\partial v_i}{\partial x_j} \frac{\partial v_j}{\partial x_i} \tag{A.2}$$

To get the minimum, we will take the first variation and set it equal to 0. Here, we will show the result of taking the first variation with respect to u_1, but we will get the same results when we take the first variation with respect to u_2 and u_3. The variation in the u_1 direction is v_1, and is equivalent to our test function in our finite element formulation.

$$
\begin{aligned}
\delta I_{u_1} =& \frac{d}{d\omega}\left[I(u_1+\omega v_1, u_2, u_3)\right]_{\omega=0} \\
=& \frac{d}{d\omega}\left[\frac{\partial u_1+\omega v_1}{\partial x_1}\frac{\partial u_1+\omega v_1}{\partial x_1}+\frac{\partial u_2}{\partial x_2}\frac{\partial u_2}{\partial x_2}+\frac{\partial u_3}{\partial x_3}\frac{\partial u_3}{\partial x_3}\right. \\
& \left. +2\frac{\partial u_1+\omega v_1}{\partial x_2}\frac{\partial u_2}{\partial x_1}+2\frac{\partial u_2}{\partial x_3}\frac{\partial u_3}{\partial x_2}+2\frac{\partial u_3}{\partial x_1}\frac{\partial u_1+\omega v_1}{\partial x_3}\right]_{\omega=0} \\
=& \frac{d}{d\omega}\left[\frac{\partial u_1}{\partial x_1}\frac{\partial u_1}{\partial x_1}+2\omega\frac{\partial u_1}{\partial x_1}\frac{\partial v_1}{\partial x_1}+\omega^2\frac{\partial v_1}{\partial x_1}\frac{\partial v_1}{\partial x_1}+2\frac{\partial u_1}{\partial x_2}\frac{\partial u_2}{\partial x_1}\right. \\
& \left. +2\omega\frac{\partial v_1}{\partial x_2}\frac{\partial u_2}{\partial x_1}+2\frac{\partial u_3}{\partial x_1}\frac{\partial u_1}{\partial x_3}+2\omega\frac{\partial u_3}{\partial x_1}\frac{\partial v_1}{\partial x_3}\right]_{\omega=0} \\
=& \frac{d}{d\omega}\left[2\omega\frac{\partial u_1}{\partial x_1}\frac{\partial v_1}{\partial x_1}+\omega^2\frac{\partial v_1}{\partial x_1}\frac{\partial v_1}{\partial x_1}+2\omega\frac{\partial v_1}{\partial x_2}\frac{\partial u_2}{\partial x_1}+2\omega\frac{\partial u_3}{\partial x_1}\frac{\partial v_1}{\partial x_3}\right]_{\omega=0} \\
=& \left[2\frac{\partial u_1}{\partial x_1}\frac{\partial v_1}{\partial x_1}+2\omega\frac{\partial v_1}{\partial x_1}\frac{\partial v_1}{\partial x_1}+2\frac{\partial v_1}{\partial x_2}\frac{\partial u_2}{\partial x_1}+2\frac{\partial u_3}{\partial x_1}\frac{\partial v_1}{\partial x_3}\right]_{\omega=0} \\
=& 2\left[\frac{\partial u_1}{\partial x_1}\frac{\partial v_1}{\partial x_1}+\frac{\partial v_1}{\partial x_2}\frac{\partial u_2}{\partial x_1}+\frac{\partial u_3}{\partial x_1}\frac{\partial v_1}{\partial x_3}\right] \\
=& 2\left[\frac{\partial}{\partial x_1}\left(\frac{\partial u_1}{\partial x_1}v_1\right)-\frac{\partial^2 u_1}{\partial x_1^2}v_1+\frac{\partial}{\partial x_2}\left(\frac{\partial u_2}{\partial x_1}v_1\right)-\frac{\partial^2 u_2}{\partial x_1\partial x_2}v_1\right. \\
& \left. +\frac{\partial}{\partial x_3}\left(\frac{\partial u_3}{\partial x_1}v_1\right)-\frac{\partial^2 u_3}{\partial x_1\partial x_3}v_1+\right] \\
=& 2\left[\nabla\cdot\left(v_1\left(\frac{\partial u_1}{\partial x_1}\mathbf{e}_1+\frac{\partial u_2}{\partial x_1}\mathbf{e}_2+\frac{\partial u_3}{\partial x_1}\mathbf{e}_3\right)\right)-v_1\frac{\partial}{\partial x_1}\left(\frac{\partial u_1}{\partial x_1}+\frac{\partial u_2}{\partial x_2}+\frac{\partial u_3}{\partial x_3}\right)\right] \\
=& 2\nabla\cdot\left(v_1\left(\frac{\partial u_1}{\partial x_1}\mathbf{e}_1+\frac{\partial u_2}{\partial x_1}\mathbf{e}_2+\frac{\partial u_3}{\partial x_1}\mathbf{e}_3\right)\right)
\end{aligned}
$$

In our finite element problem, we will take the integral of δI_{u_1} over a volume, so we can use the divergence theorem to convert it to a surface integral. The surface integral is equal to 0, since our test function v_1 is equal to 0 on the boundary, as shown below:

$$
\begin{aligned}
\int_v \delta I_{u_1} dv &= \int_v 2\nabla\cdot\left(v_1\left(\frac{\partial u_1}{\partial x_1}\mathbf{e}_1+\frac{\partial u_2}{\partial x_1}\mathbf{e}_2+\frac{\partial u_3}{\partial x_1}\mathbf{e}_3\right)\right)dv \\
&= \int_A 2v_1\left(\frac{\partial u_1}{\partial x_1}\mathbf{e}_1+\frac{\partial u_2}{\partial x_1}\mathbf{e}_2+\frac{\partial u_3}{\partial x_1}\mathbf{e}_3\right)\cdot\mathbf{n}da \\
&= 0
\end{aligned}
$$

We will achieve the same result when we take the first variation with respect to u_1 and u_2.

Therefore, minimizing viscous dissipation is the same as minimizing the velocity gradient.

A.2 Comparison to enstrophy

Enstrophy is defined:

$$\varepsilon = |\omega|^2 = |\nabla \times \mathbf{u}|^2$$

We can rewrite this

$$\begin{aligned}
|\nabla \times \mathbf{u}|^2 =& \| \left(\frac{\partial u_2}{\partial x_3} - \frac{\partial u_3}{\partial x_2} \right) \mathbf{e}_1 + \left(\frac{\partial u_3}{\partial x_1} - \frac{\partial u_1}{\partial x_3} \right) \mathbf{e}_2 + \left(\frac{\partial u_1}{\partial x_2} - \frac{\partial u_2}{\partial x_1} \right) \mathbf{e}_3 \|_2^2 \\
=& \left(\frac{\partial u_2}{\partial x_3} - \frac{\partial u_3}{\partial x_2} \right)^2 + \left(\frac{\partial u_3}{\partial x_1} - \frac{\partial u_1}{\partial x_3} \right)^2 + \left(\frac{\partial u_1}{\partial x_2} - \frac{\partial u_2}{\partial x_1} \right)^2 \\
=& \sum_i \sum_j \left(\frac{\partial u_i}{\partial x_j} \right)^2 - \sum_i \left(\frac{\partial u_i}{\partial x_i} \right)^2 - \sum_i \sum_j \left(\frac{\partial u_i}{\partial x_j} \frac{\partial u_j}{\partial x_i} \right) + \sum_i \left(\frac{\partial u_i}{\partial x_i} \right)^2 \\
=& \sum_i \sum_j \left(\frac{\partial u_i}{\partial x_j} \right)^2 - \sum_i \sum_j \left(\frac{\partial u_i}{\partial x_j} \frac{\partial u_j}{\partial x_i} \right) \\
=& \|\nabla u\|_F^2 - \sum_i \sum_j \left(\frac{\partial u_i}{\partial x_j} \frac{\partial u_j}{\partial x_i} \right)
\end{aligned}$$

We are concerned with the difference between minimizing enstrophy and minimizing the velocity gradient. The difference is

$$I_2 = -\sum_i \sum_j \left(\frac{\partial u_i}{\partial x_j} \frac{\partial u_j}{\partial x_i} \right)$$

This is the negative of the difference between velocity gradient and viscous dissipation. In the previous subsection we showed that when we take the minimum, the term $-I_2$ does not contribute. We will get the same result for positive I_2.

Appendix B

Calculation of Kinetic Energy and Viscous Dissipation Rate in Synthetic Vortex Flows

The following section displays the steps for calculating kinetic energy and viscous dissipation rate in vortex flow fields with analytical solutions.

B.1 Rigid-body Vortices

In a rigid-body vortex, angular rotational velocity, Ω, is uniform. The center of the vortex is located at $x_c\mathbf{e_x} + y_c\mathbf{e_y} + z_c\mathbf{e_z} = r_c\mathbf{e_r} + \theta_c\mathbf{e}_\theta + z_c\mathbf{e_z}$. The velocity field is

$$
\begin{aligned}
\mathbf{u} =& -\Omega(y - y_c)\mathbf{e_x} + \Omega(x - x_c)\mathbf{e_y} \\
=& -\Omega(r\sin\theta - r_c\sin\theta_c)(\mathbf{e_r}\cos\theta - \mathbf{e}_\theta\sin\theta) + \Omega(r\cos\theta - r_c\cos\theta_c)(\mathbf{e_r}\sin\theta + \mathbf{e}_\theta\cos\theta) \\
=& \Omega(-r\sin\theta\cos\theta + r_c\sin\theta_c\cos\theta + r\cos\theta\sin\theta - r_c\cos\theta_c\sin\theta)\mathbf{e_r} \\
&+ \Omega(r\sin\theta\sin\theta - r_c\sin\theta_c\sin\theta + r\cos\theta\cos\theta - r_c\cos\theta_c\cos\theta)\mathbf{e}_\theta \\
=& \Omega r_c(\sin\theta_c\cos\theta - \cos\theta_c\sin\theta)\mathbf{e_r} + \Omega(r - r_c(\sin\theta_c\sin\theta + \cos\theta_c\cos\theta))\mathbf{e}_\theta
\end{aligned}
$$

B.1.1 Kinetic Energy

Kinetic energy can be evaluated analytically. In $2D$ we get:

$$\begin{aligned}
KE_{2D} =& \frac{1}{2}\Omega^2\big((\sin\theta_c\cos\theta - \cos\theta_c\sin\theta)^2 + (r - r_c(\sin\theta_c\sin\theta + \cos\theta_c\cos\theta))^2\big) \\
=& \frac{1}{2}\Omega^2\big(\sin^2\theta_c\cos^2\theta - 2\sin\theta_c\cos\theta\cos\theta_c\sin\theta + \cos^2\theta_c\sin^2\theta \\
& + r^2 - 2rr_c(\sin\theta_c\sin\theta + \cos\theta_c\cos\theta) - r_c^2(\sin\theta_c\sin\theta + \cos\theta_c\cos\theta)^2\big) \\
=& \frac{1}{2}\Omega^2\big((1 - r_c^2)(\sin^2\theta_c\cos^2\theta - 2\sin\theta_c\cos\theta\cos\theta_c\sin\theta + \cos^2\theta_c\sin^2\theta) \\
& + r^2 - 2rr_c(\sin\theta_c\sin\theta + \cos\theta_c\cos\theta)\big)
\end{aligned}$$

In $1D$ we get

$$\begin{aligned}
KE_{1D} =& \frac{1}{2}\Omega^2(\sin\theta_c\cos\theta - \cos\theta_c\sin\theta)^2 \\
=& \frac{1}{2}\Omega^2(\sin^2\theta_c\cos^2\theta - 2\sin\theta_c\cos\theta\cos\theta_c\sin\theta + \cos^2\theta_c\sin^2\theta)
\end{aligned}$$

B.1.2 Viscous Dissipation Rate

The viscous dissipation rate can be evaluated analytically. In $2D$ we get:

$$\phi_{2D} = 0$$

However in $1D$, the viscous dissipation rate estimate yields a nonzero value:

$$\begin{aligned}
\phi_{1D} =& \frac{\mu}{\rho}\left(2\left(\frac{1}{r}\Omega r_c(\sin\theta_c\cos\theta - \cos\theta_c\sin\theta)\right)^2 + \left(\frac{\Omega r_c}{r}(-\sin\theta_c\sin\theta - \cos\theta_c\cos\theta)\right)^2\right) \\
=& \frac{\mu}{\rho}\left(\frac{\Omega r_c}{r}\right)^2\left(2(\sin\theta_c\cos\theta - \cos\theta_c\sin\theta)^2 + (\sin\theta_c\sin\theta\cos\theta_c\cos\theta)^2\right) \\
=& \frac{\mu}{\rho}\left(\frac{\Omega r_c}{r}\right)^2\Big(2\sin^2\theta_c\cos^2\theta - 4\sin\theta_c\cos\theta_c\sin\theta\cos\theta + 2\cos^2\theta_c\sin^2\theta \\
& + \sin^2\theta_c\sin^2\theta + 2\sin\theta_c\sin\theta\cos\theta_c\cos\theta + \cos^2\theta_c\cos^2\theta\Big) \\
=& \frac{\mu}{\rho}\left(\frac{\Omega r_c}{r}\right)^2\Big(2\sin^2\theta_c\cos^2\theta - 2\sin\theta_c\cos\theta_c\sin\theta\cos\theta + 2\cos^2\theta_c\sin^2\theta \\
& + \sin^2\theta_c\sin^2\theta + \cos^2\theta_c\cos^2\theta\Big) \\
=& \frac{\mu}{\rho}\left(\frac{\Omega r_c}{r}\right)^2\Big(1 + \sin^2\theta_c\cos^2\theta + \cos^2\theta_c\sin^2\theta\Big)
\end{aligned}$$

B.2 Irrotational Vortices

In an irrotational vortex, the velocity is inversely proportional to the center of the vortex:

$$\begin{aligned}
\mathbf{u} =& -\alpha(y-y_c)((x-x_c)^2+(y-y_c)^2)^{-1}\mathbf{e_x} + \alpha(x-x_c)((x-x_c)^2+(y-y_c)^2)^{-1}\mathbf{e_y} \\
=& \frac{-\alpha(r\sin\theta - r_c\sin\theta_c)}{(r\cos\theta - r_c\cos\theta_c)^2+(r\sin\theta-r_c\sin\theta_c)^2}(\mathbf{e_r}\cos\theta - \mathbf{e}_\theta\sin\theta) \\
&+ \frac{\alpha(r\cos\theta - r_c\cos\theta_c)}{(r\cos\theta - r_c\cos\theta_c)^2+(r\sin\theta-r_c\sin\theta_c)^2}(\mathbf{e_r}\sin\theta + \mathbf{e}_\theta\cos\theta) \\
=& \frac{\alpha}{(r^2+r_c^2-2rr_c(\sin\theta\sin\theta_c+\cos\theta\cos\theta_c))}\Big((r\sin\theta\cos\theta(-1+1) + r_c(\sin\theta_c\cos\theta - \\
& \cos\theta_c\sin\theta))\mathbf{e_r} + (r\sin^2\theta - r_c\sin\theta_c\sin\theta + r\cos^2\theta - r_c\cos\theta_c\cos\theta)\mathbf{e}_\theta\Big) \\
=& \frac{\alpha}{(r^2+r_c^2-2rr_c\cos(\theta_c-\theta))}\Big(r_c(\sin\theta_c\cos\theta - \cos\theta_c\sin\theta)\mathbf{e_r} \\
& + (r - r_c(\sin\theta_c\sin\theta+\cos\theta_c\cos\theta))\mathbf{e}_\theta\Big) \\
=& \frac{\alpha}{(r^2+r_c^2-2rr_c\cos(\theta_c-\theta))}\Big(r_c\sin(\theta_c-\theta)\mathbf{e_r} + (r - r_c\cos(\theta_c-\theta))\mathbf{e}_\theta\Big)
\end{aligned}$$

B.2.1 Kinetic Energy

Kinetic energy can be evaluated analytically. In $2D$ we get:

$$\begin{aligned}
KE_{2D} =& \frac{1}{2}\frac{\alpha^2}{(r^2+r_c^2-2rr_c\cos(\theta_c-\theta))^2}\Big(r_c^2\sin^2(\theta_c-\theta) + r^2 - 2rr_c\cos(\theta_c-\theta) \\
& + r_c^2\cos^2(\theta_c-\theta)\Big) \\
=& \frac{\alpha^2}{2}\frac{r_c^2+r^2-2rr_c\cos(\theta_c-\theta)}{(r^2+r_c^2-2rr_c\cos(\theta_c-\theta))^2} \\
=& \frac{1}{2}\frac{\alpha^2}{(r^2+r_c^2-2rr_c\cos(\theta_c-\theta))}
\end{aligned}$$

In $1D$,

$$KE_{1D} = \frac{\alpha^2}{2}\frac{r_c^2\sin^2(\theta_c-\theta)}{(r^2+r_c^2-2rr_c\cos(\theta_c-\theta))^2}$$

B.2.2 Viscous Dissipation Rate

The viscous dissipation rate can be evaluated analytically. In $2D$ we get:

$$\begin{aligned}
\phi_{2D} =& 4\left(\frac{\partial u_x}{\partial x}\right)^2 + 4\left(\frac{\partial u_y}{\partial u}\right)^2 + 2\left(\frac{\partial u_y}{\partial x} + \frac{\partial u_x}{\partial y}\right)^2 \\
=& 4\left(\frac{2\alpha(y-y_c)(x-x_c)}{((x-x_c)^2+(y-y_c)^2)^2}\right)^2 + 4\left(\frac{-2\alpha(y-y_c)(x-x_c)}{((x-x_c)^2+(y-y_c)^2)^2}\right)^2 \\
&+ 2\left(\frac{-\alpha}{(x-x_c)^2+(y-y_c)^2} + \frac{2\alpha(y-y_c)^2}{((x-x_c)^2+(y-y_c)^2)^2}\right. \\
&\left.+ \frac{\alpha}{(x-x_c)^2+(y-y_c)^2} - \frac{2\alpha(x-x_c)^2}{((x-x_c)^2+(y-y_c)^2)^2}\right)^2 \\
=& 8\left(\frac{4\alpha^2(y-y_c)^2(x-x_c)^2}{((x-x_c)^2+(y-y_c)^2)^4}\right) \\
&+ 2\left(\frac{2\alpha(y-y_c)^2}{((x-x_c)^2+(y-y_c)^2)^2} - \frac{2\alpha(x-x_c)^2}{((x-x_c)^2+(y-y_c)^2)^2}\right)^2 \\
=& \frac{32\alpha^2(y-y_c)^2(x-x_c)^2}{((x-x_c)^2+(y-y_c)^2)^4} + 8\alpha^2\left(\frac{(y-y_c)^2-(x-x_c)^2}{((x-x_c)^2+(y-y_c)^2)^2}\right)^2 \\
=& 8\alpha^2\frac{4(y-y_c)^2(x-x_c)^2+(y-y_c)^4-2(y-y_c)^2(x-x_c)^2+(x-x_c)^4}{((x-x_c)^2+(y-y_c)^2)^4} \\
=& 8\alpha^2\frac{(y-y_c)^4+2(y-y_c)^2(x-x_c)^2+(x-x_c)^4}{((x-x_c)^2+(y-y_c)^2)^4} \\
=& 8\alpha^2\frac{((y-y_c)^2+(x-x_c)^2)^2}{((x-x_c)^2+(y-y_c)^2)^4} \\
=& \frac{8\alpha^2}{((x-x_c)^2+(y-y_c)^2)^2} \\
=& \frac{8\alpha^2}{((r\cos\theta - r_c\cos\theta_c)^2+(r\sin\theta - r_c\sin\theta_c)^2)^2} \\
=& \frac{8\alpha^2}{(r^2+r_c^2-2rr_c\cos(\theta_c-\theta))^2}
\end{aligned}$$

But in $1D$:

$$\begin{aligned}
\phi_{1D} =& \frac{16r^2\sin^2(\theta_c-\theta)(r-r_c\cos(\theta_c-\theta))^2}{(r^2+r_c^2-2rr_c\cos(\theta_c-\theta))^4} \\
&+ \frac{4\left(-r^2+2rr_c\cos(\theta_c-\theta)-r_c^2\cos^2(\theta_c-\theta)+r_c^2\sin^2(\theta_c-\theta)\right)^2}{(r^2+r_c^2-2rr_c\cos(\theta_c-\theta))^4}
\end{aligned}$$

B.3 Lamb-Oseen Vortex

The Lamb-Oseen vortex is an exact solution of the 2D Navier-Stokes equation.

When the center is at $r = 0$,

$$\begin{aligned} v_r =& 0 \\ v_\theta =& \frac{\gamma}{2\pi r}\left(1 - \exp\left(-\frac{r^2}{c^2(t)}\right)\right) \end{aligned}$$

where

$$\begin{aligned} \gamma =& \text{ circulation contained in the vortex} \\ \nu =& \text{ viscosity} \\ c(t) =& \sqrt{4\nu t + c^2(0)} \end{aligned}$$

In cartesian coordinates, we have

$$\begin{aligned} v_x =& -\frac{\gamma}{2\pi r}\left(1 - \exp\left(-\frac{r^2}{c^2(t)}\right)\right)\sin(\arctan(y/x)) \\ v_y =& \frac{\gamma}{2\pi r}\left(1 - \exp\left(-\frac{r^2}{c^2(t)}\right)\right)\cos(\arctan(y/x)) \\ v_x =& -\frac{\gamma}{2\pi r}\left(1 - \exp\left(-\frac{r^2}{c^2(t)}\right)\right)(y/r) \\ v_y =& \frac{\gamma}{2\pi r}\left(1 - \exp\left(-\frac{r^2}{c^2(t)}\right)\right)(x/r) \\ v_x =& -\frac{\gamma}{2\pi(x^2+y^2)}\left(1 - \exp\left(-\frac{(x^2+y^2)}{c^2(t)}\right)\right)y \\ v_y =& \frac{\gamma}{2\pi(x^2+y^2)}\left(1 - \exp\left(-\frac{(x^2+y^2)}{c^2(t)}\right)\right)x \end{aligned}$$

When the center is at $r = r_c$, $\theta = \theta_c$,

$$
\begin{aligned}
v_x =& -\frac{\gamma}{2\pi((x-x_c)^2+(y-y_c)^2)}\left(1-\exp\left(-\frac{((x-x_c)^2+(y-y_c)^2)}{c^2(t)}\right)\right)(y-y_c)\\
v_y =& \frac{\gamma}{2\pi((x-x_c)^2+(y-y_c)^2)}\left(1-\exp\left(-\frac{(((x-x_c)^2+(y-y_c)^2)}{c^2(t)}\right)\right)(x-x_c)\\
v_x =& -\frac{\gamma\left(1-\exp\left(-\frac{r^2+r_c^2-2rr_c(\sin\theta\sin\theta_c+\cos\theta\cos\theta_c)}{c^2(t)}\right)\right)}{2\pi(r^2+r_c^2-2rr_c(\sin\theta\sin\theta_c+\cos\theta\cos\theta_c))}(r\sin\theta-r_c\sin\theta_c)\\
v_y =& \frac{\gamma\left(1-\exp\left(-\frac{r^2+r_c^2-2rr_c(\sin\theta\sin\theta_c+\cos\theta\cos\theta_c)}{c^2(t)}\right)\right)}{2\pi(r^2+r_c^2-2rr_c(\sin\theta\sin\theta_c+\cos\theta\cos\theta_c))}(r\cos\theta-r_c\cos\theta_c)
\end{aligned}
$$

In polar coordinates, we have

$$
\begin{aligned}
v_r =& \frac{\gamma\left(1-\exp\left(-\frac{r^2+r_c^2-2rr_c(\sin\theta\sin\theta_c+\cos\theta\cos\theta_c)}{c^2(t)}\right)\right)}{2\pi(r^2+r_c^2-2rr_c(\sin\theta\sin\theta_c+\cos\theta\cos\theta_c))}\Big(-(r\sin\theta-r_c\sin\theta_c)\cos\theta\\
&+(r\cos\theta-r_c\cos\theta_c)\sin\theta\Big)\\
v_\theta =& \frac{\gamma\left(1-\exp\left(-\frac{r^2+r_c^2-2rr_c(\sin\theta\sin\theta_c+\cos\theta\cos\theta_c)}{c^2(t)}\right)\right)}{2\pi(r^2+r_c^2-2rr_c(\sin\theta\sin\theta_c+\cos\theta\cos\theta_c))}\Big((r\sin\theta-r_c\sin\theta_c)\sin\theta\\
&+(r\cos\theta-r_c\cos\theta_c)\cos\theta\Big)\\
v_r =& \frac{\gamma\left(1-\exp\left(-\frac{r^2+r_c^2-2rr_c(\sin\theta\sin\theta_c+\cos\theta\cos\theta_c)}{c^2(t)}\right)\right)}{2\pi(r^2+r_c^2-2rr_c(\sin\theta\sin\theta_c+\cos\theta\cos\theta_c))}\Big(r_c(\sin\theta_c\cos\theta-\cos\theta_c\sin\theta)\Big)\\
v_\theta =& \frac{\gamma\left(1-\exp\left(-\frac{r^2+r_c^2-2rr_c(\sin\theta\sin\theta_c+\cos\theta\cos\theta_c)}{c^2(t)}\right)\right)}{2\pi(r^2+r_c^2-2rr_c(\sin\theta\sin\theta_c+\cos\theta\cos\theta_c))}\Big(r-r_c(\sin\theta_c\sin\theta+\cos\theta_c\cos\theta)\Big)\\
v_r =& \frac{\gamma r_c\sin(\theta_c-\theta)}{2\pi(r^2+r_c^2-2rr_c\cos(\theta_c-\theta))}\left(1-\exp\left(-\frac{r^2+r_c^2-2rr_c\cos(\theta_c-\theta)}{c^2(t)}\right)\right)\\
v_\theta =& \frac{\gamma(r-r_c\cos(\theta_c-\theta))}{2\pi(r^2+r_c^2-2rr_c\cos(\theta_c-\theta))}\left(1-\exp\left(-\frac{r^2+r_c^2-2rr_c\cos(\theta_c-\theta)}{c^2(t)}\right)\right)
\end{aligned}
$$

B.3.1 Kinetic Energy

In $2D$, kinetic energy is equal to

$$\begin{aligned} KE_{2D} =& \frac{1}{2}\frac{\gamma^2\big(r_c^2\sin^2(\theta_c-\theta)+r^2-2rr_c\cos(\theta_c-\theta)+r_c^2\cos^2(\theta_c-\theta)\big)}{4\pi^2(r^2+r_c^2-2rr_c\cos(\theta_c-\theta))^2}\Bigg(1 \\ & -\exp\left(-\frac{r^2+r_c^2-2rr_c\cos(\theta_c-\theta)}{c^2(t)}\right)\Bigg)^2 \\ =& \frac{1}{2}\frac{\gamma^2\big(r_c^2+r^2-2rr_c\cos(\theta_c-\theta)\big)}{4\pi^2(r^2+r_c^2-2rr_c\cos(\theta_c-\theta))^2}\left(1-\exp\left(-\frac{r^2+r_c^2-2rr_c\cos(\theta_c-\theta)}{c^2(t)}\right)\right)^2. \end{aligned}$$

In $1D$,

$$KE_{1D} = \frac{\gamma^2\big(r_c^2\sin^2(\theta_c-\theta)\big)}{8\pi^2(r^2+r_c^2-2rr_c\cos(\theta_c-\theta))^2}\left(1-\exp\left(-\frac{r^2+r_c^2-2rr_c\cos(\theta_c-\theta)}{c^2(t)}\right)\right)^2.$$

B.3.2 Viscous Dissipation Rate

The viscous dissipation rate can also be evaluated analytically, but that is not explored herein.

B.4 Hill's Spherical Vortex

In 3D, the velocity field within a Hill's Spherical Vortex centered at $(0,0,0)$ with radius c is:

$$\begin{aligned} v_r =& \frac{3U}{2c^2}rz \\ v_\theta =& 0 \\ v_z =& \frac{3U}{2c^2}(c^2-2r^2-z^2) \end{aligned}$$

which in cartesian coordinates is

$$\begin{aligned} v_x =& \frac{x}{\sqrt{x^2+y^2}}\frac{3U}{2c^2}\sqrt{x^2+y^2}z = \frac{3U}{2c^2}xz \\ v_y =& \frac{y}{\sqrt{x^2+y^2}}\frac{3U}{2c^2}\sqrt{x^2+y^2}z = \frac{3U}{2c^2}yz \\ v_z =& \frac{3U}{2c^2}(c^2-2(x^2+y^2)-z^2) \end{aligned}$$

The velocity field outside of the vortex centered at $(0,0,0)$ with radius c is:

$$\begin{aligned} v_r =& \frac{3c^3U}{2}\frac{rz}{(r^2+z^2)^{5/2}} \\ v_\theta =& 0 \\ v_z =& -U - \frac{c^3U}{2}\frac{(r^2-2z^2)}{(r^2+z^2)^{5/2}} \end{aligned}$$

which in cartesian coordinates is

$$\begin{aligned} v_x =& \frac{x}{\sqrt{x^2+y^2}}\frac{3c^3U}{2}\frac{\sqrt{x^2+y^2}z}{(x^2+y^2+z^2)^{5/2}} = \frac{3c^3U}{2}\frac{xz}{(x^2+y^2+z^2)^{5/2}} \\ v_y =& \frac{y}{\sqrt{x^2+y^2}}\frac{3c^3U}{2}\frac{\sqrt{x^2+y^2}z}{(x^2+y^2+z^2)^{5/2}} = \frac{3c^3U}{2}\frac{yz}{(x^2+y^2+z^2)^{5/2}} \\ v_z =& -U - \frac{c^3U}{2}\frac{(x^2+y^2-2z^2)}{(x^2+y^2+z^2)^{5/2}} \end{aligned}$$

For the purposes of a 2D examination of a vortex, we will look at the vortex in the $x-z$ plane, where $y=0$. Therefore, v_y goes to 0 and we care about v_x and v_z. In addition, we consider a vortex centered at $(x_c, 0, z_c)$.

Inside the vortex, we get

$$\begin{aligned} v_x =& \frac{3U}{2c^2}(x-x_c)(z-z_c) \\ v_y =& 0 \\ v_z =& \frac{3U}{2c^2}(c^2 - 2(x-x_c)^2 - (z-z_c)^2). \end{aligned}$$

Outside of the vortex, the velocity is

$$\begin{aligned} v_x =& \frac{3c^3U}{2}\frac{(x-x_c)(z-z_c)}{((x-x_c)^2+(z-z_c)^2)^{5/2}} \\ v_y =& 0 \\ v_z =& -U - \frac{c^3U}{2}\frac{((x-x_c)^2-2(z-z_c)^2)}{((x-x_c)^2+(z-z_c)^2)^{5/2}}. \end{aligned}$$

Now, we consider the results in a special version of radial coordinates, where y is taken to be the azimuthal direction and the r-θ plane corresponds to the x-z plane. In these radial coordinates the conversion of coordinates looks like:

$$\begin{aligned} \mathbf{e}_r =& \mathbf{e}_z\cos\theta + \mathbf{e}_x\sin\theta & \mathbf{e}_\theta =& -\mathbf{e}_z\sin\theta + \mathbf{e}_x\cos\theta \\ \mathbf{e}_z =& \mathbf{e}_r\cos\theta - \mathbf{e}_\theta\sin\theta & \mathbf{e}_x =& \mathbf{e}_r\sin\theta + \mathbf{e}_\theta\cos\theta \end{aligned}$$

Inside the vortex the velocity field looks like:

$$
\begin{aligned}
v_r =& v_x \sin\theta + v_z \cos\theta \\
=& \frac{3U}{2c^2}(x - x_c)(z - z_c)\sin\theta + \frac{3U}{2c^2}(c^2 - 2(x - x_c)^2 - (z - z_c)^2)\cos\theta \\
=& \frac{3U}{2c^2}(r\sin\theta - r_c\sin\theta_c)(r\cos\theta - r_c\cos\theta_c)\sin\theta \\
&+ \frac{3U}{2c^2}(c^2 - 2(r\sin\theta - r_c\sin\theta_c)^2 - (r\cos\theta - r_c\cos\theta_c)^2)\cos\theta \\
v_\theta =& v_x \cos\theta - v_z \sin\theta \\
=& \frac{3U}{2c^2}(x - x_c)(z - z_c)\cos\theta - \frac{3U}{2c^2}(c^2 - 2(x - x_c)^2 - (z - z_c)^2)\sin\theta \\
=& \frac{3U}{2c^2}(r\sin\theta - r_c\sin\theta_c)(r\cos\theta - r_c\cos\theta_c)\cos\theta \\
&- \frac{3U}{2c^2}(c^2 - 2(r\sin\theta - r_c\sin\theta_c)^2 - (r\cos\theta - r_c\cos\theta_c)^2)\sin\theta.
\end{aligned}
$$

Outside of the vortex the velocity field looks like:

$$
\begin{aligned}
v_r =& v_x \sin\theta + v_z \cos\theta \\
=& \frac{3c^3U}{2} \frac{(x-x_c)(z-z_c)}{((x-x_c)^2+(z-z_c)^2)^{5/2}} \sin\theta - \big(U + \frac{c^3U}{2} \frac{((x-x_c)^2-2(z-z_c)^2)}{((x-x_c)^2+(z-z_c)^2)^{5/2}}\big) \cos\theta \\
=& -U\cos\theta + \left(\frac{c^3U}{2((x-x_c)^2+(z-z_c)^2)^{5/2}}\right)\Big(3(x-x_c)(z-z_c)\sin\theta \\
& - ((x-x_c)^2-2(z-z_c)^2)\cos\theta\Big) \\
=& -U\cos\theta \\
& + \left(\frac{c^3U}{2((r\sin\theta - r_c\sin\theta_c)^2+(r\cos\theta - r_c\cos\theta_c)^2)^{5/2}}\right)\Big(3(r\sin\theta - r_c\sin\theta_c)(r\cos\theta \\
& - r_c\cos\theta_c)\sin\theta - ((r\sin\theta - r_c\sin\theta_c)^2 - 2(r\cos\theta - r_c\cos\theta_c)^2)\cos\theta\Big) \\
v_\theta =& v_x\cos\theta - v_z\sin\theta \\
=& \frac{3c^3U}{2} \frac{(x-x_c)(z-z_c)}{((x-x_c)^2+(z-z_c)^2)^{5/2}} \cos\theta + \big(U + \frac{c^3U}{2} \frac{((x-x_c)^2-2(z-z_c)^2)}{((x-x_c)^2+(z-z_c)^2)^{5/2}}\big) \sin\theta \\
=& U\sin\theta + \left(\frac{c^3U}{2((x-x_c)^2+(z-z_c)^2)^{5/2}}\right)\Big(3(x-x_c)(z-z_c)\cos\theta + ((x-x_c)^2 \\
& - 2(z-z_c)^2)\sin\theta\Big) \\
=& U\sin\theta \\
& + \left(\frac{c^3U}{2((r\sin\theta - r_c\sin\theta_c)^2+(r\cos\theta - r_c\cos\theta_c)^2)^{5/2}}\right)\Big(3(r\sin\theta - r_c\sin\theta_c)(r\cos\theta \\
& - r_c\cos\theta_c)\cos\theta + ((r\sin\theta - r_c\sin\theta_c)^2 - 2(r\cos\theta - r_c\cos\theta_c)^2)\sin\theta\Big).
\end{aligned}
$$

The kinetic energy and viscous dissipation rate can also be evaluated analytically, but they are not explored in this paper.

Bibliography

[1] Pierce, E., 2005. Heart labelled large.

[2] Dyverfeldt, P., Bissell, M., Barker, A. J., Bolger, A. F., Carlhäll, C.-j., Ebbers, T., Francios, C. J., Frydrychowicz, A., Geiger, J., Giese, D., Hope, M. D., Kilner, P. J., Kozerke, S., Myerson, S., Neubauer, S., Wieben, O., and Markl, M., 2015. "4D flow cardiovascular magnetic resonance consensus statement". *Journal of Cardiovascular Magnetic Resonance*, pp. 1–19.

[3] Heart disease fact sheet. Centers for Disease Control and Prevention.

[4] Mendis, S., Armstrong, T., Bettcher, D., Branca, F., Lauer, J., Mace, C., Poznyak, V., Riley, L., De Costa E Silva, V., and Stevens, G., 2014. "Global status report on noncommunicable diseases 2014". *World Health Organization*, p. 176.

[5] Kochanek, K. D., Xu, J., Murphy, S. L., Minino, A. M., and Kung, H.-C., 2016. "National Vital Statistics Reports: Deaths : Final Data for 2013". *National Center for Health Statistics,* **64**(2), pp. 1–119.

[6] Paulus, W. J., and van Ballegoij, J. J., 2010. "Treatment of Heart Failure With Normal Ejection Fraction". *Journal of the American College of Cardiology,* **55**(6), pp. 26–34.

[7] Goliasch, G., Goscinska-Bis, K., Caracciolo, G., Nakabo, A., Smolka, G., Pedrizzetti, G., Narula, J., and Sengupta, P. P., 2013. "CRT improves LV filling dynamics: Insights from echocardiographic particle imaging velocimetry". *JACC: Cardiovascular Imaging,* **6**(6), pp. 704–713.

[8] What is heart failure? American Heart Association.

[9] Silent ischemia and ischemic heart disease. American Heart Association.

[10] Nichols, W., O'Rourke, M., and Vlachopoulos, C., 2011. *McDonald's Blood Flow in Arteries: Theoretical, Experimental and Clinical Principles*, 6 ed. Hodder Arnold.

[11] Bermejo, J., Martínez-Legazpi, P., and Del Álamo, J. C., 2015. "The Clinical Assessment of Intraventricular Flows". *Annual Review of Fluid Mechanics,* **47**(1), pp. 315–342.

[12] Gharib, M., Rambod, E., Kheradvar, A., Sahn, D. J., and Dabiri, J. O., 2006. "Optimal vortex formation as an index of cardiac health.". *Proceedings of the National Academy of Sciences of the United States of America,* **103**(16), pp. 6305–6308.

[13] Faludi, R., Szulik, M., D'hooge, J., Herijgers, P., Rademakers, F., Pedrizzetti, G., and Voigt, J.-U., 2010. "Left ventricular flow patterns in healthy subjects and patients with prosthetic mitral valves: An in vivo study using echocardiographic particle image

velocimetry". *The Journal of Thoracic and Cardiovascular Surgery,* **139**(6), pp. 1501–1510.

[14] Elbaz, M. S., van der Geest, R. J., Calkoen, E. E., de Roos, A., Lelieveldt, B. P., a.W. Roest, A., and Westenberg, J. J., 2017. "Assessment of viscous energy loss and the association with three-dimensional vortex ring formation in left ventricular inflow: In vivo evaluation using four-dimensional flow MRI". *Magnetic Resonance in Medicine,* **00**, pp. n/a–n/a.

[15] Bolger, A. F., Heiberg, E., Karlsson, M., Wigström, L., Engvall, J., Sigfridsson, A., Ebbers, T., Kvitting, J.-P. E., Carlhäll, C. J., and Wranne, B., 2007. "Transit of blood flow through the human left ventricle mapped by cardiovascular magnetic resonance". *Journal of Cardiovascular Magnetic Resonance,* **9**(5), pp. 741–747. PMID: 17891610.

[16] Taylor, 2004. "Experimental and Computational Methods in Cardiovascular Fluid Mechanics". *Annual Review of Fluid Mechanics,* **36**(1), p. 197.

[17] Stankovic, Z., Allen, B. D., Garcia, J., Jarvis, K. B., and Markl, M., 2014. "4D flow imaging with MRI.". *Cardiovascular diagnosis and therapy,* **4**(2), pp. 173–92.

[18] Seraphim, A., Paschou, S. A., and Grapsa, J., 2016. "Pocket-Sized Echocardiography Devices : One Stop Shop Service ?". *Journal of Cardiovascular Ultrasound*, pp. 1–6.

[19] Evans, D. H., Jensen, J. A., and Nielsen, M. B., 2011. "Ultrasonic colour Doppler imaging.". *Interface Focus,* **1**(May), pp. 490–502.

[20] Bermejo, J., Benito, Y., Alhama, M., Yotti, R., Martinez-Legazpi, P., del Villar, C. P., Perez-David, E., Gonzalez-Mansilla, A., Santa-Marta, C., Barrio, A., Fernandez-Aviles, F., and del Alamo, J. C., 2014. "Intraventricular vortex properties in nonischemic dilated cardiomyopathy". *AJP: Heart and Circulatory Physiology,* **306**(5), pp. H718–H729.

[21] Rajiah, P., Tandon, A., Greil, G. F., and Abbara, S., 2017. "Update on the Role of Cardiac Magnetic Resonance Imaging in Congenital Heart Disease". *Current Treatment Options in Cardiovascular Medicine,* **19**(1), p. 2.

[22] Hope, M. D., Sedlic, T., and Dyverfeldt, P., 2013. "Cardiothoracic magnetic resonance flow imaging". *Journal of Thoracic Imaging,* **28**(4), pp. 217–230.

[23] Frank, S., 2016. "Color Doppler Ultrasound Velocity Field Reconstruction: Accounting for Through-Plane Divergence". Master's thesis, University of California, Berkeley, Spring.

[24] Garcia, D., del Alamo, J. C., Tanné., D., Yotti, R., Cortina, C., Bertrand, E., Antoranz, J. C., Pérez-David, E., Rieu, R., Fernández-Avilés, F., and Bermejo, J., 2010. "Two-dimensional intraventricular flow mapping by digital processing conventional color-

doppler echocardiography images". *IEEE Transactions on Medical Imaging,* **29**(10), pp. 1701–1713.

[25] Uejima, T., Koike, A., Sawada, H., Aizawa, T., Ohtsuki, S., Tanaka, M., Furukawa, T., and Fraser, A. G., 2010. "A New Echocardiographic Method for Identifying Vortex Flow in the Left Ventricle: Numerical Validation". *Ultrasound in Medicine & Biology,* **36**(5), pp. 772–788.

[26] Ohtsuki, S., and Tanaka, M., 2006. "The flow velocity distribution from the doppler information on a plane in three-Dimensional flow". *Journal of Visualization,* **9**(1), pp. 69–82.

[27] Hendabadi, S., Bermejo, J., Benito, Y., Yotti, R., Fernandez-Aviles, F., Del Alamo, J. C., and Shadden, S. C., 2013. "Topology of blood transport in the human left ventricle by novel processing of doppler echocardiography". *Annals of Biomedical Engineering,* **41**(12), pp. 2603–2616.

[28] Rossini, L., Martinez-Legazpi, P., Benito, Y., Pérez del Villar, C., Gonzalez-Mansilla, A., Barrio, A., Borja, M.-G., Yotti, R., Kahn, A. M., Shadden, S. C., Fernández-Avilés, F., Bermejo, J., and Del Álamo, J. C., 2016. "Clinical assessment of intraventricular blood transport in patients undergoing cardiac resynchronization therapy". *Meccanica*.

[29] Wolf, J., 2015. "Validation and Improvements to Ultrasound-Based Flow Diagnostics for the Human Left Ventricle". Master's thesis, University of California, Berkeley.

[30] Jang, J., Ahn, C. Y., Jeon, K., Heo, J., Lee, D., Joo, C., Choi, J.-i., and Seo, J. K., 2015. "A Reconstruction Method of Blood Flow Velocity in Left Ventricle Using Color Flow Ultrasound". *Computational and Mathematical Methods in Medicine,* **2015**.

[31] Hoffman, J., Jansson, J., Vilela de Abreu, R., Degirmenci, N. C., Jansson, N., Muller, K., Nazarov, M., and Spuller, J. H., 2012. "Unicorn : Parallel adaptive finite element simulation of turbulent flow and fluid-structure interaction for deforming domains and complex geometry". *Computers&fluids*.

[32] Lekien, F., Coulliette, C., Bank, R., and Marsden, J., 2004. "Open-boundary modal analysis: Interpolation, extrapolation, and filtering". *Journal of Geophysical Research,* **109**.

[33] Jeong, D., Anagnostopoulos, P. V., Roldan-Alzate, A., Srinivasan, S., Schiebler, M. L., Wieben, O., and François, C. J., 2015. "Ventricular kinetic energy may provide a novel noninvasive way to assess ventricular performance in patients with repaired tetralogy of Fallot". *Journal of Thoracic and Cardiovascular Surgery,* **149**(5), pp. 1339–1347.

[34] Garg, P., Crandon, S., Swoboda, P. P., Fent, G. J., Foley, J. R., Chew, P. G., Brown, L. A., Vijayan, S., Hassell, M. E., Nijveldt, R., Bissell, M., Elbaz, M. S., Al-Mohammad, A., Westenberg, J. J., Greenwood, J. P., Van Der Geest, R. J., Plein, S., and Dall'Armellina, E., 2018. "Left ventricular blood flow kinetic energy after myocardial infarction - Insights from 4D flow cardiovascular magnetic resonance". *Journal of Cardiovascular Magnetic Resonance,* **20**(61).

[35] Garg, P., van der Geest, R. J., Swoboda, P. P., Crandon, S., Fent, G. J., Foley, J. R. J., Dobson, L. E., Al Musa, T., Onciul, S., Vijayan, S., Chew, P. G., Brown, L. A. E., Bissell, M., Hassell, M. E. C. J., Nijveldt, R., Elbaz, M. S. M., Westenberg, J. J. M., Dall'Armellina, E., Greenwood, J. P., and Plein, S., 2018. "Left ventricular thrombus formation in myocardial infarction is associated with altered left ventricular blood flow energetics". *European Heart Journal - Cardiovascular Imaging,* **20**(1), pp. 108–117.

[36] Kanski, M., Arvidsson, P. M., Töger, J., Borgquist, R., Heiberg, E., Carlsson, M., and Arheden, H., 2015. "Left ventricular fluid kinetic energy time curves in heart failure from cardiovascular magnetic resonance 4D flow data". *Journal of Cardiovascular Magnetic Resonance,* **17**(111).

[37] Sjöberg, P., Heiberg, E., Wingren, P., Ramgren Johansson, J., Malm, T., Arheden, H., Liuba, P., and Carlsson, M., 2017. "Decreased Diastolic Ventricular Kinetic Energy in Young Patients with Fontan Circulation Demonstrated by Four-Dimensional Cardiac Magnetic Resonance Imaging". *Pediatric Cardiology,* **38**(4), pp. 669–680.

[38] Wong, J., Chabiniok, R., DeVecchi, A., Dedieu, N., Sammut, E., Schaeffter, T., and Razavi, R., 2016. "Age-related changes in intraventricular kinetic energy: a physiological or pathological adaptation?". *American Journal of Physiology - Heart and Circulatory Physiology,* **310**(6), pp. H747–H755.

[39] Kim, I.-C., Hong, G.-R., Pedrizzetti, G., Shim, C. Y., Kang, S.-M., and Chung, N., 2018. "Usefulness of Left Ventricular Vortex Flow Analysis for Predicting Clinical Outcomes in Patients with Chronic Heart Failure: A Quantitative Vorticity Imaging Study Using Contrast Echocardiography". *Ultrasound in Medicine and Biology,* **44**(9), pp. 1951–1959.

[40] Pedrizzetti, G., and Domenichini, F., 2005. "Nature optimizes the swirling flow in the human left ventricle". *Physical Review Letters,* **95**(10), pp. 1–4.

[41] Di Labbio, G., and Kadem, L., 2018. "Jet collisions and vortex reversal in the human left ventricle". *Journal of Biomechanics*, pp. 1–6.

[42] Kamphuis, V. P., Elbaz, M. S. M., van den Boogaard, P. J., Kroft, L. J. M., van der Geest, R. J., de Roos, A., Helbing, W. A., Blom, N. A., Westenberg, J. J. M., and Roest, A. A. W., 2018. "Disproportionate intraventricular viscous energy loss in fontan

patients: analysis by 4d flow mri". *European Heart Journal - Cardiovascular Imaging*, p. jey096.

[43] Kamphuis, V. P., Westenberg, J. J. M., van der Palen, R. L. F., van den Boogaard, P. J., van der Geest, R. J., de Roos, A., Blom, N. A., Roest, A. A. W., and Elbaz, M. S. M., 2018. "Scan–rescan reproducibility of diastolic left ventricular kinetic energy, viscous energy loss and vorticity assessment using 4D flow MRI: analysis in healthy subjects". *The International Journal of Cardiovascular Imaging,* **34**(6), pp. 905–920.

[44] Cibis, M., Jarvis, K., Markl, M., Rose, M., Rigsby, C., Barker, A. J., and Wentzel, J. J., 2015. "The effect of resolution on viscous dissipation measured with 4D flow MRI in patients with Fontan circulation: Evaluation using computational fluid dynamics". *Journal of Biomechanics,* **48**(12), pp. 2984–2989.

[45] Itatani, K., Okada, T., Uejima, T., Tanaka, T., Ono, M., Miyaji, K., and Takenaka, K., 2013. "Intraventricular flow velocity vector visualization based on the continuity equation and measurements of vorticity and wall shear stress". *Japanese Journal of Applied Physics,* **52**(7S), p. 07HF16.

[46] Hayashi, T., Itatani, K., Inuzuka, R., Shimizu, N., Shindo, T., Hirata, Y., and Miyaji, K., 2015. "Dissipative energy loss within the left ventricle detected by vector flow mapping in children: Normal values and effects of age and heart rate". *Journal of Cardiology,* **66**(5), pp. 403–410.

[47] Akiyama, K., Maeda, S., Matsuyama, T., Kainuma, A., Ishii, M., Naito, Y., Kinoshita, M., Hamaoka, S., Kato, H., Nakajima, Y., Nakamura, N., Itatani, K., and Sawa, T., 2017. "Vector flow mapping analysis of left ventricular energetic performance in healthy adult volunteers". *BMC Cardiovascular Disorders,* **17**(1), pp. 1–10.

[48] Yoshida, S., Miyagawa, S., Fukushima, S., Yoshikawa, Y., Hata, H., Saito, S., Yoshioka, D., Kainuma, S., Domae, K., Matsuura, R., Nakatani, S., Toda, K., and Sawa, Y., 2018. "Cardiac Function and Type of Mitral Valve Surgery Affect Postoperative Blood Flow Pattern in the Left Ventricle". *Circulation Journal,* **83**(1), pp. 130–138.

[49] Li, C.-m., Bai, W.-j., Liu, Y.-t., Tang, H., and Rao, L., 2017. "Dissipative energy loss within the left ventricle detected by vector flow mapping in diabetic patients with controlled and uncontrolled blood glucose levels". *The International Journal of Cardiovascular Imaging,* **33**(8), pp. 1151–1158.

[50] Stugaard, M., Koriyama, H., Katsuki, K., Masuda, K., Asanuma, T., Takeda, Y., Sakata, Y., Itatani, K., and Nakatani, S., 2015. "Energy loss in the left ventricle obtained by vector flow mapping as a new quantitative measure of severity of aortic regurgitation: a combined experimental and clinical study". *European Heart Journal - Cardiovascular Imaging,* **16**(7), pp. 723–730.

[51] Batchelor, G., 2000. *An Introduction to Fluid Dynamics*. Cambridge University Press, doi:10.1017/CBO9780511800955.

[52] Markl, M., Chan, F. P., Alley, M. T., Wedding, K. L., Draney, M. T., Elkins, C. J., Parker, D. W., Wicker, R., Taylor, C. A., Herfkens, R. J., and Pelc, N. J., 2003. "Time-resolved three-dimensional phase-contrast MRI". *Journal of Magnetic Resonance Imaging,* **17**(4), pp. 499–506.

[53] Köhler, B., Born, S., van Pelt, R. F. P., Hennemuth, A., Preim, U., and Preim, B., 2016. "A Survey of Cardiac 4D PC-MRI Data Processing". *Computer Graphics Forum,* **00**(0), pp. 1–30.

[54] Callaghan, F. M., and Grieve, S. M., 2016. "Spatial Resolution and Velocity Field Improvement of 4D-Flow MRI". *Magnetic Resonance in Medicine,* **00**.

[55] Dyverfeldt, P., and Ebbers, T., 2017. "Comparison of respiratory motion suppression techniques for 4D flow MRI". *Magnetic Resonance in Medicine,* **00**(October 2016), pp. 1–6.

[56] Elsinga, G. E., Scarano, F., Wieneke, B., and Van Oudheusden, B. W., 2006. "Tomographic particle image velocimetry". *Experiments in Fluids,* **41**(6), pp. 933–947.

[57] Atkinson, C., and Soria, J., 2009. "An efficient simultaneous reconstruction technique for tomographic particle image velocimetry". *Experiments in Fluids,* **47**, pp. 553–568.

[58] Novara, M., Batenburg, K. J., and Scarano, F., 2010. "Motion tracking-enhanced MART for tomographic PIV". *Measurement Science and Technology,* **21**.

[59] Discetti, S., Natale, A., and Astarita, T., 2013. "Spatial filtering improved tomographic PIV". *Experiments in Fluids,* **54**(4).

[60] Garcia, D., 2009. "Robust smoothing of gridded data in one and higher dimensions with missing values". *Computational Statistics and Data Analysis,* **54**(4), pp. 1167–1178.

[61] Thielicke, W., and Stamhuis, E. J., 2014. "PIVlab – Towards User-friendly, Affordable and Accurate Digital Particle Image Velocimetry in MATLAB". *Journal of Open Research Software,* **2**.

[62] Kähler, C. J., Astarita, T., Vlachos, P. P., Sakakibara, J., Hain, R., Discetti, S., La Foy, R., and Cierpka, C., 2016. "Main results of the 4th International PIV Challenge". *Experiments in Fluids,* **57**(97).

[63] Schiavazzi, D., Coletti, F., Iaccarino, G., and Eaton, J. K., 2014. "A matching pursuit approach to solenoidal filtering of three-dimensional velocity measurements". *Journal of Computational Physics,* **263**, pp. 206–221.

[64] De Silva, C. M., Philip, J., and Marusic, I., 2013. "Minimization of divergence error in volumetric velocity measurements and implications for turbulence statistics". *Experiments in Fluids,* **54**.

[65] Song, S. M., Napel, S., Glover, G. H., and Pelc, N. J., 1993. "Noise reduction in three-dimensional phase-contrast MR velocity measurements.". *Journal of magnetic resonance imaging : JMRI,* **3**(4), pp. 587–96.

[66] Busch, J., Giese, D., Wissmann, L., and Kozerke, S., 2013. "Reconstruction of divergence-free velocity fields from cine 3D phase-contrast flow measurements". *Magnetic Resonance in Medicine,* **69**(1), pp. 200–210.

[67] Santelli, C., Loecher, M., Busch, J., Wieben, O., Schaeffter, T., and Kozerke, S., 2015. "Accelerating 4D flow MRI by exploiting vector field divergence regularization". *Magnetic Resonance in Medicine,* **00**.

[68] Falahatpisheh, A., Pedrizzetti, G., and Kheradvar, A., 2014. "Three-dimensional reconstruction of cardiac flows based on multi-planar velocity fields". *Experiments in Fluids,* **55**(11).

[69] Ong, F., Uecker, M., Tariq, U., Hsiao, A., Alley, M. T., Vasanawala, S. S., and Lustig, M., 2015. "Robust 4D flow denoising using divergence-free wavelet transform". *Magnetic Resonance in Medicine,* **73**(2), pp. 828–842.

[70] Assi, K. C., Gay, E., Chnafa, C., Mendez, S., Nicoud, F., Abascal, J. F. P. J., Lantelme, P., and Garcia, D., 2017. "Intraventricular vector flow mapping - a Doppler-based regularized problem with automatic model selection". *Physics in Medicine & Biology,* **62**, pp. 7131–7147.

[71] Taira, K., Brunton, S. L., Dawson, S. T. M., Rowley, C. W., Colonius, T., Mckeon, B. J., and Schmidt, O. T., 2017. "Modal Analysis of Fluid Flows: An Overview". *ArXiv e-prints*.

[72] Chu, P. C., Ivanov, L. M., Korzhova, T. P., Margolina, T. M., and Melnichenko, O. V., 2003. "Analysis of sparse and noisy ocean current data using flow decomposition. Part I: Theory". *Journal of Atmospheric and Oceanic Technology,* **20**(Inoue 1986), pp. 478–491.

[73] Johnson, K. M., and Markl, M., 2010. "Improved SNR in phase contrast velocimetry with five-point balanced flow encoding". *Magnetic Resonance in Medicine,* **63**(2), pp. 349–355.

[74] Abe, H., Caracciolo, G., Kheradvar, A., Pedrizzetti, G., Khandheria, B. K., Narula, J., and Sengupta, P. P., 2013. "Contrast echocardiography for assessing left ventricular vortex strength in heart failure: A prospective cohort study". *European Heart Journal Cardiovascular Imaging,* **14**(11), pp. 1049–1060.

[75] Eriksson, J., Bolger, A. F., Ebbers, T., and Carlhäll, C.-J., 2016. "Assessment of left ventricular hemodynamic forces in healthy subjects and patients with dilated cardiomyopathy using 4D flow MRI". *Physiological Reports,* **4**(3), pp. 1–12.

[76] Badas, M. G., Domenichini, F., and Querzoli, G., 2016. "Quantification of the blood mixing in the left ventricle using Finite Time Lyapunov Exponents". *Meccanica*.

[77] Jensen, J. A., Gran, F., Udensen, J., Nielsen, M. B., and Nielsen, K. R., 2006. "Vector blood velocity estimation in medical ultrasound". *5th International Symposium on Ultrasonic Doppler Methods for Fluid Mechanics and Fluid Engineering*.

[78] Holbek, S., Christiansen, T. L., Stuart, M. B., Beers, C., Thomsen, E. V., and Jensen, J. A., 2016. "3-D Vector Flow Estimation With Row-Column-Addressed Arrays". *IEEE Transactions on Ultrasonics, Ferroelectrics, and Frequency Control,* **63**(11), pp. 1799–1814.

[79] Gu, T., Korosec, F. R., Block, W. F., Fain, S. B., Turk, Q., Lum, D., Zhou, Y., Grist, T., Haughton, V., and Mistretta, C. A., 2005. "PC VIPR: A High-Speed 3D Phase-Contrast Method for Flow Quantification and High- Resolution Angiography". *American Journal of Neuroradiology,* **26**(4), pp. 743–749.

[80] Wang, D., Shao, J., Ennis, D. B., and Hu, P., 2016. "Phase-contrast MRI with hybrid one and two-sided flow-encoding and velocity spectrum separation". *Magnetic Resonance in Medicine,* **00**.

[81] Bollache, E., Barker, A. J., Dolan, R. S., Carr, J. C., van Ooij, P., Ahmadian, R., Powell, A., Collins, J. D., Geiger, J., and Markl, M., 2017. "k-t accelerated aortic 4D flow MRI in under two minutes: Feasibility and impact of resolution, k-space sampling patterns, and respiratory navigator gating on hemodynamic measurements". *Magnetic Resonance in Medicine,* **00**.

[82] Bastkowski, R., Weiss, K., Maintz, D., and Giese, D., 2018. "Self-gated golden-angle spiral 4D flow MRI". *Magnetic Resonance in Medicine,* **80**(3), pp. 904–913.

[83] Tafti, P. D., Delgado-Gonzalo, R., Stalder, A. F., and Unser, M., 2011. "Variational enhancement and denoising of flow field images". In 2011 IEEE International Symposium on Biomedical Imaging: From Nano to Macro, pp. 1061–1064.

[84] Bostan, E., Lefkimmiatis, S., Vardoulis, O., Stergiopulos, N., and Unser, M., 2015. "Improved variational denoising of flow fields with application to phase-contrast MRI data". *IEEE Signal Processing Letters,* **22**(6), pp. 762–766.

[85] Sereno, M. F., Köhler, B., and Preim, B., 2018. "Comparison of divergence-free filters for cardiac 4D PC-MRI data". *Bildverarbeitung für die Medizin*(211279), pp. 139–144.

[86] Loecher, M., Kecskemeti, S., Turski, P., and Wieben, O., 2012. "Comparison of divergence-free algorithms for 3D MRI with three-directional velocity encoding". *Journal of Cardiovascular Magnetic Resonance,* **14(Suppl 1**(W64).

[87] Oliveira, F. P., and Tavares, J. M. R., 2014. "Medical image registration: A review". *Computer Methods in Biomechanics and Biomedical Engineering,* **17**(2), pp. 73–93.

[88] Myronenko, A., and Song, X. B., 2010. "Point Set Registration: Coherent Point Drift". {*IEEE*} *Transactions on Pattern Analysis and Machine Intelligence,* **32**(12), pp. 2262–2275.